

ISSN : 2372-0484

AIMS MEDICAL SCIENCE

VOLUME NO. 10
ISSUE NO. 1
JANUARY - APRIL 2023

AIMS Medical Science

Aim & Scopes

AIMS Medical Science is an international Open Access journal devoted to publishing peer-reviewed, high quality, original papers in the field of medical science. We publish the following article types: original research articles, reviews, case report, editorials, letters, and conference reports.

AIMS Medical Science welcomes, but not limited to, the papers from the following topics:

- Basic medicine
- Clinical medicine
- Genetics
- Surgery
- Cancer
- Neurology
- Serology
- Radiology
- Pathology

Editor-in-Chief**Kelly Pagidas**

Texas Christian University, Professor and Chair of Medical Education, Fort Worth, Texas, USA

Managing Editor**Shengjiao Pang**

AIMS Press, Anli Road, Chaoyang District, Beijing 100101, China

Geriatrics Section**Casey Peiris (Assistant Section Editor)**

Department of Rehabilitation, Nutrition and Sport, La Trobe University, Melbourne, Victoria, Australia

Susanne FinneganWarwick Clinical Trials Unit, The University of
Warwick, UK**Carol Dillon**National Scientific and Technical Research Council
(CONICET-CEMIC); CEMIC University Hospital;
Universidad de Palermo; Instituto Universitario
CEMIC, Buenos Aires, Argentina.**Pediatrics Section****Piero Pavone**

Pediatric Clinic AOU Policlinico-Vittorio Emanuele University of Catania, Via S. Sofia 78, 95123, Catania, Italy.

Endocrinology Section**Panayota Mitrou (Section Editor-in-Chief)**

Senior Researcher. Hellenic National Diabetes Center, Attikon University Hospital, Athens, Greece.

Ali Tiss

Dasman Diabetes Institute, Kuwait

Alessandro P. DelitalaDepartment of Internal Medicine, Azienda-
Ospedaliero-University of Sassari, Sassari, Italy.**Hubert E. Blum**University Hospital Freiburg, Clinic of Internal
Medicine II, Hugstetterstrasse 55, D-79106 Freiburg,
Germany**Sujith Rajan**NYU Langone Long Island School of Medicine,
United States**Nursing and Health Section****Belgüzar Kara (Section Editor-in-Chief)**

Department of Internal Medicine Nursing, Faculty of Health Sciences, Yuksek Ihtisas University, Turkey.

Eleanor HolroydSchool of Clinical Sciences, Auckland University of
Technology, Auckland 1142, New Zealand**Kaumudi Jinraj Joshipura**Department of Epidemiology, Center for Clinical
Research and Health Promotion, University of Puerto
Rico, Medical Sciences Campus, USA**Gwendolyn P. Quinn**Department of Oncologic Sciences, The University of South Florida, Morsani College of Medicine, Tampa, Florida,
USA**Medical Imaging Section****Yi-Jang Lee (Section Editor-in-Chief)**

Biomedical Imaging and Radiological Sciences, National Yang-Ming University, Taipei, Taiwan

<p>Herbert F. Jelinek Charles Sturt University, School of Community Health, Albury, NSW 2640, Australia</p>	<p>Elizabeth A. Krupinski The University of Arizona; Departments of Medical Imaging, Psychology and Public Health, Tucson, AZ, USA</p>
<p>Iman Aganj Martinos Center for Biomedical Imaging, Radiology Department, Massachusetts General Hospital, Harvard Medical School, USA</p>	<p>Laurent Risser French National Centre for Scientific Research (CNRS), Mathematics Institute of Toulouse, Paris, France</p>
Biomedical Informatics Section	
<p>Costas Iliopoulos(Section Editor-in-Chief) Department of Informatics, King's College London, Strand, London, England</p>	
<p>Andrei Kelarev School of Information Technology, Deakin University, 221 Burwood Highway, Melbourne, Vic 3125, Australia</p>	<p>Brendan James Keating D.Phil. Departments of Pediatrics and Surgery (Division of Transplantation), University of Pennsylvania, USA</p>
<p>Mai Alzamel Department of Informatics, King's College London, Strand, London</p>	<p>Lars Malmström Institute for Computational Science, University of Zurich, Zurich, Switzerland</p>
Molecular Biomedical Section	
<p>Laurent Metzinger(Section Editor-in-Chief) Faculty of Pharmacy and Medicine, University of Picardie Jules Verne, Centre De Biologie Humaine, Amiens University Medical Center, France</p>	
<p>Raul N Ondarza Department of Biochemistry, Faculty of Medicine, National Autonomous University of Mexico (UNAM), Mexico</p>	<p>Ivana. de la Serna Department of Biochemistry and Cancer Biology, University of Toledo College of Medicine Toledo, OH, USA</p>
<p>Sok Kean Khoo Department of Cell and Molecular Biology; Grand Valley State University, USA</p>	<p>Nina Gunde-Cimerman Department of Biology, Biotechnical Faculty, University of Ljubljana, Slovenia</p>
<p>Jianjie Wang Department of Biomedical Sciences; Missouri State University, Springfield, MO 65897, USA</p>	<p>Louis Ragolia NYU Winthrop Hospital, Stony Brook University School of Medicine, 101 Mineola Blvd, Suite 4-003, Mineola, NY 11501, USA</p>
<p>Marco Lucarelli Department of Cellular Biotechnologies and Hematology of the Medical Faculty of the Sapienza University of Rome, Italy</p>	<p>Patrick Legembre Universite Rennes-1; CLCC Eugene Marquis, INSERM U1242-COSS, Team Ligue Contre Le Cancer, 35042 Rennes, France</p>
<p>Chiaki Hidai Division of Physiology, Department of Biomedical Sciences, School of Medicine, Nihon University, Japan</p>	
Stomatology Section	
<p>Lei Liu Department of Oral and Maxillofacial Surgery, West China Hospital of Stomatology, Sichuan University, Chengdu, Sichuan, China</p>	<p>Theresa S. Gonzales Department of Stomatology, Medical University of South Carolina, Division of Oral Pathology, SC, USA</p>

Biomedical Engineering Section

<p>Seongkyu Yoon Francis College of Engineering, Department of Chemical Engineering, University of Massachusetts Lowell, Massachusetts 01854, USA</p>	<p>Xiaoyang Xu Department of Chemical, Biological and Pharmaceutical Engineering, New Jersey Institute of Technology, USA</p>
<p>Andrés Díaz Lantada Product Development Laboratory, Mechanical Engineering Department, Universidad Politécnica de Madrid, 28006 Madrid, Spain</p>	<p>Ji Hyun Kim Wake Forest Institute for Regenerative Medicine, Wake Forest School of Medicine, Medical Center Boulevard, Winston-Salem, NC 27157, USA</p>

Cancer Section

<p>Robert Arthur Kratzke Masonic Cancer Center, University of Minnesota Medical School, Minneapolis, MN 55455, USA</p>	<p>Azam Bolhassani Department of Hepatitis and AIDs, Pasteur Institute of Iran (IPI), Tehran, Iran</p>
<p>Gulshan Sunavala-Dossabhoy Department of Biochemistry and Molecular Biology LSU Health Sciences Center, Shreveport, USA</p>	<p>Elias El-Habr Faculty of Biology, School of Science, Sorbonne Universités, France</p>

Pathology Section

<p>Ying Sun Department of Pediatrics, Cincinnati Children's Hospital Medical Center, Division of Human Genetics, Cincinnati, Ohio, USA</p>	<p>Robert D. Odze Gastrointestinal Pathology, Brigham and Women's Hospital Harvard Medical School, Boston, MA 02115, USA</p>
<p>Jianhua Luo Department of Pathology, University of Pittsburgh, USA</p>	<p>José E. Manautou Male; Professor. Department of Pharmaceutical Sciences, School of Pharmacy, University of Connecticut, USA</p>
<p>Ahmad Oryan Department of Pathology, School of Veterinary Medicine, Shiraz University, Iran</p>	

Obstetrics Section

<p>Lee P. Shulman Department of Obstetrics and Gynecology, Feinberg School of Medicine, Northwestern University, 250 East Superior Street, Room 05-2174, Chicago, IL 60611, USA</p>	<p>Kai Wang Michael E. DeBakey Department of Surgery, Baylor College of Medicine, Houston, TX, USA</p>
<p>Jean-Marie Exbrayat Lyon Catholic University, Laboratory of Biosciences, Technologies and Ethics, EPHE, 69002 Lyon, France</p>	

Ophthalmology Section

<p>Dominique Bremond-Gignac Ophthalmology Department, University Hospital Necker Enfants Malades, Paris, France</p>	<p>Haoyu Chen Joint Shantou International Eye Center, Shantou University and the Chinese University of Hong Kong, Shantou, China</p>
<p>Ursula Schmidt-Erfurth Department of Ophthalmology, Medical University of Vienna, Austria</p>	<p>Aljoscha S. Neubauer Department of Ophthalmology, Ludwig-Maximilians University, Munich, Germany</p>

Jorge L. Alió
Division of Ophthalmology, Universidad Miguel
Hernández, Alicante, Spain

Nebbioso Marcella
Department of Sense Organs, Ocular
Electrophysiology Center, Faculty of Medicine and
Odontology, Sapienza University of Rome, Rome
00185, Italy

Cardiology Section

Pasquale Palmiero
Heart Station and Echocardiography Laboratory, ASL
Brindisi, Professor of Cardiology, Bari University
Medical School, Italy

Samir Kapadia
Cleveland Clinic Department of Cardiovascular
Medicine, Cleveland, OH 44195, USA

Claus J. Preusse
Department of Cardiac Surgery, University of Bonn,
Germany

Sandra Rugonyi
Biomedical Engineering, Oregon Health and Science
University (OHSU), Portland, USA

Bogdan Borz
Department of Cardiology, Clinique de l'Union, Saint-
Jean, France

Hemang Panchal
Department of Internal Medicine; East Tennessee State
University; Johnson City, TN 37604, USA.

Immunology Section

Giuliana Banche
School of Medicine, Department of Public Health and
Pediatrics, University of Torino, Via Santena 9, 10126
Turin, Italy

Teodor-Doru Brumeanu
Department of Medicine, Division of Immunology,
Uniformed Services University, 4301 Jones Bridge
Road, Bethesda, MD 20814, USA

Robert Todd Striker
Department of Medical Microbiology and
Immunology, Infectious Disease Staff, W.S. Middleton
Veterans Hospital, Hepatitis C Lead Clinician, USA

Sreekumar Othumpangat
Centers for Disease Control and Prevention, Health
Effects Laboratory Division, 1095 Willowdale road,
Morgantown, WV 26505, USA

Sidgi Syed Anwer Abdo Hasson
Department of Microbiology and Immunology,
College of Medicine and Health Sciences, Sultan
Qaboos University, Al-Khod, P.O. Box 35, Muscat
123, Oman

Maria Teresa Fiorillo
Department of Biology and Biotechnology, "C.
Darwin" Sapienza, Sapienza-University of Rome,
Roma

Michaela Semeraro
Clinical Investigation Center, Necker Children's
Hospital, Paris, France

Wesam Kooti
Kurdistan University of Medical Sciences, Sanandaj,
Iran

Neurology Section

Tatsuro Mutoh (Section Editor-in-chief)
Department of Neurology, Fujita Health University School of Medicine, Japan

Michael Persinger
Department of Psychology, Laurentian University,
Sudbury, Canada

David A. Loewenstein
Department of Psychiatry and Behavioral Sciences,
University of Miami, USA

Corrado Angelini
Neuromuscular Neurorehabilitative Diseases,
University of Padova, Venice, Italy

Zhifang Dong
Children's Hospital of Chongqing Medical University,
China

Yang Zhuo
College of Medicine, Nankai University, China

Sang Ki Park
Department of Life Sciences, Pohang University of
Science and Technology (POSTECH), South Korea

<p>Kurt A. Jellinger Institute of Clinical Neurobiology, Kenyongasse 18, A-1070 Vienna, Austria</p>	<p>Mohamed Ouardouz NRAC, 39 Du Meteore, Gatineau, Quebec, J9A 3B5, Canada</p>
<p>Carli Lorraine Roulston Department of Medicine, St Vincent's Campus, University of Melbourne, Melbourne 3065, Australia</p>	<p>Massimiliano Filosto Center for Neuromuscular Diseases (ERN-EURO NMD Center), Unit of Neurology, ASST "Spedali Civili" and University of Brescia, P.le Spedali Civili 1, Brescia 25100, Italy</p>
<p>Athanasios Alexiou Novel Global Community Educational Foundation, Australia and AFNP Med, Austria</p>	
<p>Pharmacology Section</p>	
<p>Tzi Bun Ng School of Biomedical Sciences, Faculty of Medicine, The Chinese University of Hong Kong(CUHK), Shatin, New Territories, Hong Kong, China</p>	<p>Yau Sang Chan School of Biomedical Sciences, Faculty of Medicine, The Chinese University of Hong Kong(CUHK), Shatin, New Territories, Hong Kong, China</p>
<p>Daniel John Sillence Health and Life Sciences Faculty; Leicester School of Pharmacy; De Montfort University, UK</p>	<p>Ramin Ataee Department of Pharmacology, Faculty of Pharmacy, Mazandaran University of Medical Sciences, Sari, Iran.</p>
<p>Gastroenterology Section</p>	
<p>Bum-Joon Kim Department of Microbiology and Immunology, College of Medicine, Seoul National University, Korea</p>	<p>Rosario Fornaro Department of Surgery, University of Genoa, Italy</p>
<p>Waled Mohsen The University of Sydney, Australia</p>	
<p>Dermatology Section</p>	
<p>Kathryn J. Martires Department of Dermatology , Kaiser Permanente Los Angeles Medical Center, Los Angeles, USA.</p>	
<p>Muscle Biology Section</p>	
<p>Wei Guo Department of Animal Science, College of Agriculture and Natural Resources. University of Wyoming, Laramie, WY 82071, USA</p>	

(Volume No. 10, Issue No. 1, January - April 2023)

Contents

Sr. No.	Article / Authors Name	Pg. No.
1	Influence of the thermomechanical behavior of NiTi wires embedded in a damper on its damping capacity: Application to a bridge cable - <i>Guillaume Helbert, Lamine Dieng, Shabnam Arbab Chirani and Philippe Pilvin</i>	1 - 22
2	Contribution to Study the effect of (Reuss, LRVE, Tamura) models on the axial and shear stress of sandwich FGM plate (Ti- 6Al- 4V/ZrO ₂) subjected on linear and nonlinear thermal loads - <i>Rebai Billel</i>	23 - 35
3	Fe-TiO ₂ /zeolite H-A photocatalyst for degradation of waste dye (methylene blue) under UV irradiation - <i>Ririn Cahyanti, Sumari Sumari, Fauziatul Fajaroh, Muhammad Roy Asrori and Yana Fajar Prakasa</i>	36 - 49
4	Effect of sub-zero treatments on hardness and corrosion properties of low-alloy nickel steel - <i>Vinda Puspasari, Satrio Herbirowo, Alvin Muhammad Habieb, Dedi Pria Utama, Rahadian Roberto and Bintang Adjiantoro</i>	50 - 62
5	Increasing the charge/discharge rate for phase-change materials by forming hybrid composite paraffin/ash for an effective thermal energy storage system - <i>Budhi Muliawan Suyitno, Dwi Rahmalina and Reza Abdu Rahman</i>	63 - 75

Influence of the thermomechanical behavior of NiTi wires embedded in a damper on its damping capacity: Application to a bridge cable

Guillaume Helbert^{1,*}, Lamine Dieng², Shabnam Arbab Chirani¹ and Philippe Pilvin³

¹ ENI Brest, UMR CNRS 6027, IRDL, Technopole Brest-Iroise, 29238 Brest, France

² Université Gustave Eiffel, MAST, Allée des Ponts et Chaussées, 44340 Bouguenais, France

³ Université Bretagne Sud, UMR CNRS 6027, IRDL, Centre de Recherche Christian Huygens, Rue

ABSTRACT

Thanks to high dissipation properties, embedding NiTi Shape Memory Alloys in passive damping devices is effective to mitigate vibrations in building and cable structures. These devices can inconceivably be tested directly on full-scale experimental structures or on structures in service. To predict their effectiveness and optimize the set-up parameters, numerical tools are more and more developed. Most of them consist of Finite Element models representing the structure equipped with the damping device, embedding parts associated with a superelastic behavior. Generally, the implemented behavior laws do not include all the phenomena at the origin of strain energy dissipation, but stress-induced martensitic transformation only. This article presents a thermomechanical behavior law including the following phenomena: (i) intermediate R-phase transformation, (ii) thermal effects and (iii) strain localization. This law was implemented in a commercial Finite Element code to study the dynamic response of a bridge cable equipped with a NiTi wire-based damping device. The numerical results were compared to full-scale experimental ones, by considering the above-mentioned phenomena taken coupled or isolated: it has been shown that it is necessary to take all of these phenomena into account in order to successfully predict the damping capacity of the device.

Keywords: bridge cable; damping device; shape memory alloys; dissipation; finite element; full-scale tests

1. Introduction

The damping capacity of a material is its ability to absorb mechanical energy by dissipation of elastic strain energy [1]. In Shape Memory Alloys (SMA), the dissipated energy is associated with their hysteretic superelastic behavior [2]. Superelasticity is the remarkable property of the material to experience a large and quasi reversible strain (6–10% or much more in the case of single crystals SMAs [3]) under isothermal mechanical loadings, above a characteristic temperature of the alloy called “Austenite finish” (Af) [4, 5]. This phenomenon is due to a reversible transformation from the parent-phase “Austenite” to a more disordered phase called “Martensite”, and more particularly to the re-orientation of the obtained lattices above a critical stress value (transformation yield stress). Thus, SMAs are good candidates to damp oscillations experienced by buildings and Civil Engineering structures [6]. In particular, NiTi-based SMAs are very attractive due to their remarkable dissipative properties, recentering ability and they combine relatively good resistance to fatigue, corrosion and fire. However, NiTi alloys are known to be very temperature-sensitive: the slope that characterizes the increase in transformation yield stress with temperature is about $7\text{--}8 \text{ MPa} \cdot \text{K}^{-1}$ [7]. Over the years, SMA-based vibration control devices (passive, active or hybrid) have been designed to protect Civil Engineering

structures from different types of external solicitations [8].

Cables are crucial parts of bridge structures (such as stay cable bridges, suspension bridges, and prestressed concrete bridges) but they experience vibrations entailed by traffic or a combination of wind and rain [9]. To increase the structural damping ratio of the cables, SMA-based external passive damping devices are well suited: they exert a transverse damping force on the cable near its anchorages to fight against transverse displacements and therefore improve its fatigue resistance. To predict the effectiveness and to optimize the use of SMA-based damping devices, numerical tools are generally required to solve strongly non-linear problems. As stated in [10, 11], it is necessary to consider the most accurate mechanical behavior (through its stiffness and loss factor changes) of the embedded SMA components to correctly capture the dynamic response of the whole system. Since it is not appropriate to identify the various model parameters describing the hysteresis loops for each of the possible test conditions, the material law should take into account all the phenomena that can affect its properties and only involve parameters intrinsic to the material. Among these phenomena, one can cite:

(1) Thermal effects:

As stated previously, the superelasticity phenomenon in NiTi-based SMAs is temperature sensitive: martensite transformation yield stress is a linear function of the material temperature [12]. Since the forward and reverse martensitic transformations are exothermic and endothermic processes respectively [13], the temperature of the material changes under mechanical loadings according to the heat exchange with its surroundings. The martensitic transformation yield stress changes as a consequence, which leads naturally to thermomechanical couplings. Thus, the slope associated to the martensitic transformation plateau and the amplitude of temperature variations over a loading cycle increase with strain rate [12]. Furthermore, the hysteresis behavior in SMA is accompanied by intrinsic dissipation [14] that entails “self-heating” of the material under cyclic mechanical loadings. It naturally shifts up the hysteresis loops and slightly affects their shape. Combination of these two phenomena is responsible for a non-monotonous change of energy dissipated by the material versus strain rate [15]. Numerous models have considered these effects [16–19].

(2) R-phase transformation:

NiTi alloys can experience an additional phase transformation allowing the formation of R-phase with a trigonal crystallographic structure [20, 21]. R-phase is often qualified as an “intermediate phase” because the yield stress associated with its transformation from austenite is lower than the martensitic transformation yield stress at room temperature [15]. The range of recoverable strain due to R-phase transformation is 0–1.5%, according to [22]. The presence of R-phase can affect the stiffness of the material: the corresponding elasticity modulus is estimated to be between 20 and 40 GPa. R-phase is associated with a low intrinsic dissipation because of a narrow hysteresis loop area but the corresponding damping capacity is not negligible. R-phase transformation is more sensitive to temperature than martensitic transformation: the slope related to R-phase domains on phases pseudo-diagram is reported to be in the range 13–17 MPa·K⁻¹ [15, 22]. Some numerical models have considered R-phase and most of them are phenomenological ones [23–26].

(3) Strain localization:

It is commonly agreed that martensitic transformation occurs with nucleation of martensite, followed by propagation of a martensitic front [27]. After [29], high shear stress values at the interface between austenite and stress-induced martensite are responsible for this localized process in NiTi wires. Under tensile loadings, the ratio of the maximum equivalent stress to the axial equivalent stress was estimated to be approximatively 1.4 to 1.6 in wires. In addition to a heterogeneous strain field, a heterogeneous

strain field, a heterogeneous thermal field was reported in [28]. Thus, these thermal effects can affect the propagation of the martensitic front, since martensite is more stable at low temperatures while the forward martensitic transformation is an exothermic process. Furthermore, this phenomenon is very dependent on the shape of the sample and boundary conditions [30, 31]: it is why the fronts generally propagate from the jaws, due to tightening. This topic is currently trendy and more and more simulations are able to predict this phenomenon [32–35].

These three phenomena are generally not considered simultaneously to numerically predict the vibratory response of cables equipped with SMA-based dampers [36–38]. The main target of the paper is to propose such a numerical tool while accurately predicting a realistic behavior of the embedded NiTi wires. In the “Experiments and modeling” section, the experimental set-up and the corresponding numerical modeling are briefly presented. In the “Results and discussion” section, several numerical configurations are compared with the experimental results, to determine the contribution of each considered phenomenon. Eventually, data available numerically only are investigated to provide a better understanding.

2. Experiments and modeling

In this section, the proposed experimental set-up and Finite Element model are presented in parallel. Firstly, the vibrating cable is considered alone. Secondly, installation of the damping device on the cable is presented. Thirdly, the thermomechanical behavior of the embedded NiTi components is dealt with. Eventually, the post-processing procedure is detailed to show how will be conducted the analysis in the “Results and discussion” section.

2.1. Full-scale bridge cable

2.1.1. Experimental set-up

A cable of length $L = 50$ m was used to measure the efficiency of the NiTi-based damping device. An axial tensile force T of approximately 900 kN was initially applied to the cable using a hydraulic jack. It must be noted that the study cases that are proposed in this paper are intentionally simplified in comparison with the loading cases experienced by cable structures in service. First, to involve the minimum number of vibration modes, punctual deviations were applied on the cable at $L/2$ or $L/4$ by applying a transverse force of 4 kN. Secondly, the force was suddenly released using an electromagnet to make the cable freely vibrating. The vibration problem is assumed to be in-plane. The cable composition and properties are given in [10].

Since $EI \ll TL^2$ Where EI is the flexural rigidity of the cable, a good approximation of the n -th mode frequency is given by [39]:

$$f_n = \frac{n}{2L} \sqrt{\frac{T}{\mu}} \left[1 + 2 \sqrt{\frac{EI}{TL^2}} + \left(4 + \frac{n\pi^2}{2} \right) \frac{EI}{TL^2} \right] \approx \frac{n}{2L} \sqrt{\frac{T}{\mu}} \quad (2.1)$$

With u the linear density of the cable. The values of the analytical modal frequencies can be used as a validation criteria of modeling. Cable transverse displacements were measured with laser sensors at three locations along the cable ($L/2$, $L/4$ and $L/16$).

2.1.2. Numerical modeling

Modeling of the cable was performed using the Finite Element Method with the MSC Marc industrial

[40]. In the proposed model, only beam or truss elements were considered, since dynamic simulations require substantial computing resources. The cable consisted of 50 two-node Euler Bernoulli beam elements. Both nodes located at the extremities of the cable were clamped (fixed degrees of freedom). An initial pre-stress corresponding to the 900 kN pretension was applied to the beam elements. The simulation was split into two parts: (i) a transverse force was progressively and slowly applied on a node until 4 kN (quasi-static formulation), (ii) the force was suddenly released (dynamic formulation) and the cable was freely vibrating for 20 s. The intrinsic damping ratio ξ of the cable due to internal frictions was estimated from experimental transverse displacement signals of the cable without any damping device using the logarithmic decrement method. A Rayleigh viscous damping was assigned on the whole cable elements to provide intrinsic damping capacity. The Rayleigh damping matrix is given by:

$$[C] = \alpha [M] + \beta [K] \quad (2.2)$$

Where $[M]$ and $[K]$ are the mass and stiffness matrices involved in the motion equilibrium equation, respectively. The coefficients $\alpha = 7.52 \cdot 10^{-3} s^{-1}$ and $\beta = 1.43 \cdot 10^{-5} s$ were calculated from the ξ value of 0.00033 [40].

2.1.3. Validation of the cable vibrating response

Figure 1a,c,d present the numerical and experimental transverse displacement of the cable at $L/2$, $L/4$ and $L/16$, respectively, while the transverse force was placed a $L/2$. Figure 1b provides the Fast Fourier Transform (FFT) spectra associated with the signals presented in Figure 1a.

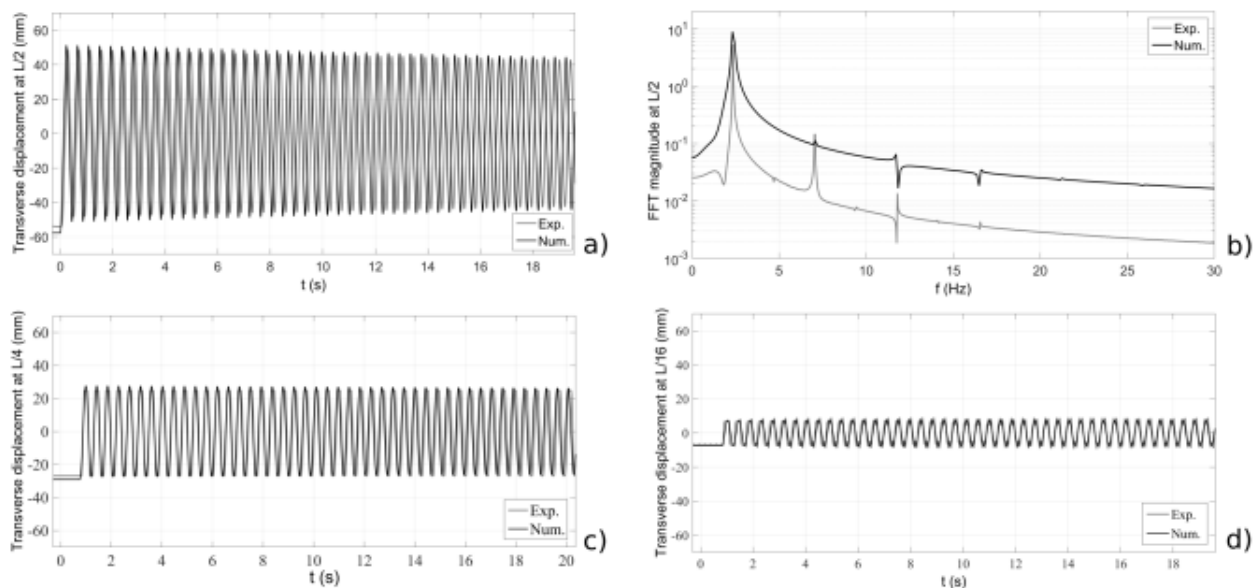


Figure 1. Transverse displacement of the cable (transverse force at $L/2$): (a) at $L/2$; (b) associated FFT frequency spectra; (c) at $L/4$; (d) at $L/16$.

The signals numerically obtained are in good agreement with the experimental signals, whatever the considered location. The frequency spectrum numerically obtained shows a good prediction of the contributions of the vibration modes. The first mode associated with a frequency value of about 2.3 Hz (as verified using Eq 2.1) had the highest contribution, since the force was placed at the corresponding anti-node. It slightly overestimated the experimental values. From the simulations, only odd-numbered modes were observable, since $L/2$ is the common node for even-numbered modes.

2.2. Design and installation of the damper

2.2.1. Developed damping device

Figure 2a presents the developed damping device. Two plates are crossed by NiTi wires. One plate was clamped to the ground, while the second plate was linked with the cable. The wires were elongated thanks to mechanical stops placed at the exterior side of each plate. Thus, the damper worked in one direction only (when the cable was moving away from the anchorage), but this system prevented wires from buckling. Figure 2b presents its installation on the full-scale cable.

The chemical composition (56.30 wt% Ni) of the NiTi alloy used in this work is detailed in [15]. The characteristic temperature A_f was measured at about 5 °C. NiTi wires were “trained” under cyclic mechanical loadings at room temperature (100 tensile cycles of 8% strain amplitude at a frequency of 0.0056 Hz) before being embedded in the damping device to limit residual strain [10]. Two wires of diameter 2.46 mm and effective length 1260 mm were embedded to reach a maximal relative elongation of 2% in service. Furthermore, the NiTi wires were pre-strained thanks to a turnbuckle system (see Figure 2a). An initial elongation of about 4 mm was chosen to increase the dissipation (for a given room temperature and a given deviating force value) as explained in [41].

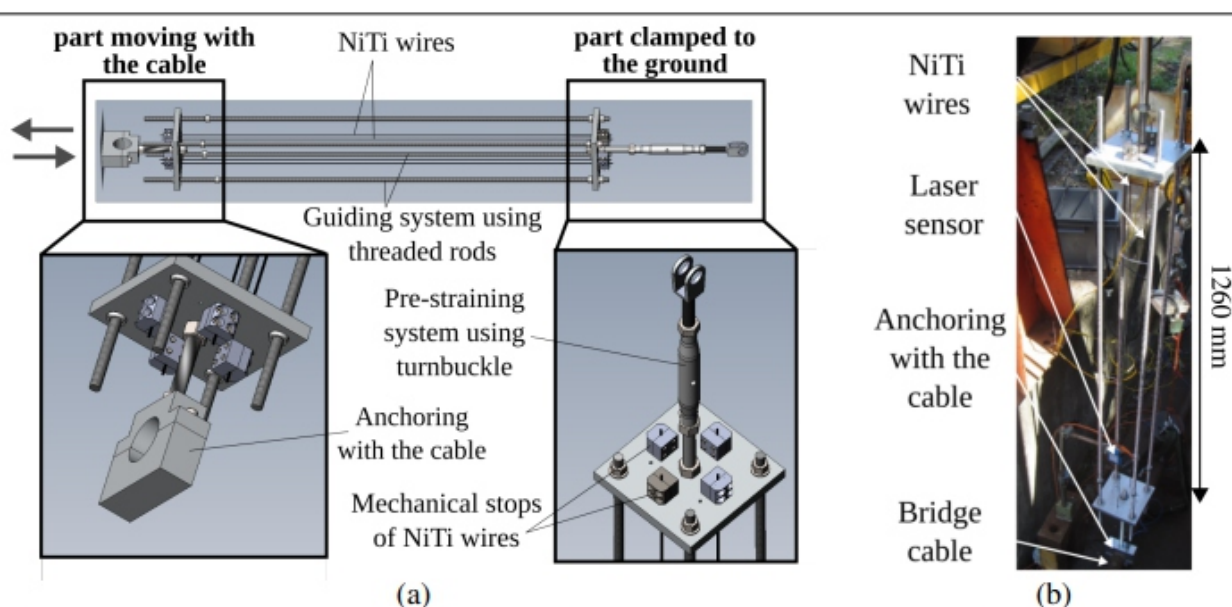


Figure 2. Damping device: (a) Scheme of the device, (b) installation on the full-scale cable.

For the sake of simplicity, the damping device was placed far from the anchorages to better understand the influence of the damper on the whole cable response. Three study cases were investigated to change the contribution of the involved vibration modes:

- (1) Damper & force at $L/2$ (reference).
- (2) Damper at $L/4$ and force at $L/2$.
- (3) Damper at $L/2$ and force at $L/4$.

The study case of reference is investigated in detail in this study.

2.2.2. Numerical assembly of the damper on the cable

Figure 3 describes the modeling of the “cable-damper” system. The damping device consisted of one or 32 (as explained later) two-node thermomechanical truss elements assembled in series. The length of the “numerical damper” was the same as the effective length of the two NiTi wires embedded in the damping device. Its cross-section area was taken as the sum of the cross-section areas of the two wires, since they

work in tension. The node at one end of the wire was fixed to the ground, while the node at the opposite end was connected with one of the nodes of the cable thanks to a spring of infinite stiffness working in the transverse direction of the cable. The selected node of the cable depends on the damper position. The stiffness of the damper was canceled in case of negative stress values to deactivate it under compression loadings. The pre-strain of the numerical damper was imposed during the very first calculation step.

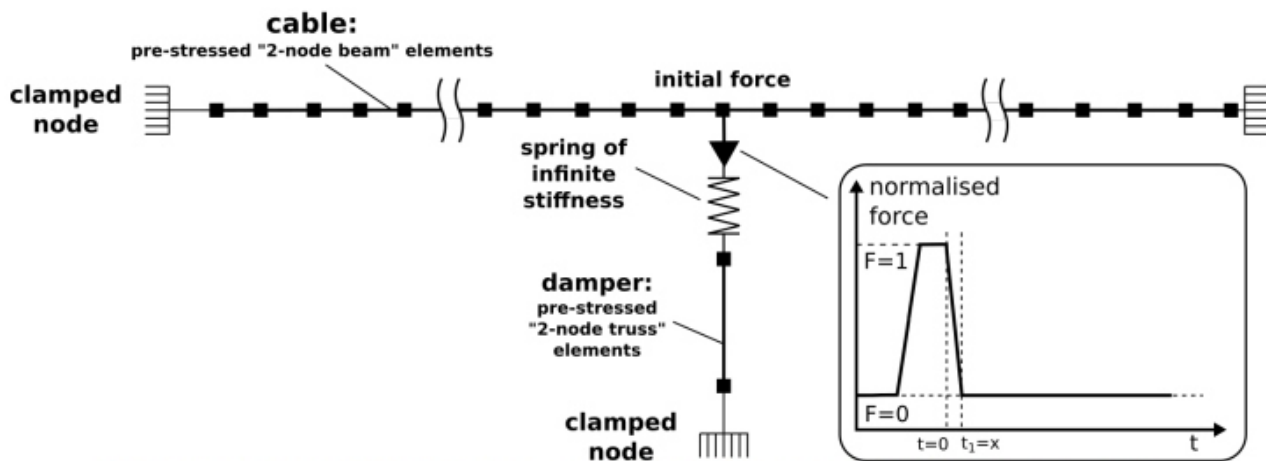


Figure 3. Scheme of the Finite Element model of the whole system “damper+cable”.

2.3. NiTi wire behavior law

2.3.1. Material behavior law

The behavior law used in what follows was presented in detail in [42]. Since the “numerical damper” was modeled by truss elements, the behavior law was written in a uniaxial version. Its role is to compute the uniaxial stress σ and tangent modulus values from the current strain E and strain increment $\Delta\epsilon$ values. The internal variables are $z_M \in [0; 1]$ and $z_R \in [0; 1]$ which are the martensite and R-phase volume fractions, respectively. The austenite volume fraction is therefore given by $z_A = 1 - z_M - z_R$.

The proposed model was based on four yield surfaces, associated with yield functions $f_{M1}(M)$ and $f_{M2}(M, X)$, driving the forward and reverse austenite-to-martensite transformations, respectively, and $f_{R3}(R, Y)$ and $f_{R4}(R, Y)$, driving the forward and reverse austenite-to-R-phase transformations, respectively. M and X are isotropic and kinematic “pseudo-hardening” functions of z_M associated with the austenite-to-martensite transformation, respectively. R and Y are isotropic and kinematic “pseudo-hardening” functions of z_R associated with austenite-to-R-phase transformation, respectively. The transformation yield stresses σ_{M0} and σ_{R0} were linear functions of the material temperature T .

The heat equation was derived from the formulated specific free energy by applying the principle of energy conservation. It involves the exchanges with the exterior by diffusion and convection, as well as the dissipation and thermomechanical coupling terms associated with both transformations.

For details on the identification procedure of the material parameters and on the model validation, the reader is referred to [42]. For this present work, the thermo-mechanical behavior law was implemented in a user subroutine coded in FORTRAN [40]. The retained material parameters corresponding to a trained NiTi wire are set out in Table 1 [43].

Table 1. Material parameters corresponding to a trained NiTi alloy.

E_A	E_M	γ_M	ω^{min}	ω^{max}	M^{max}	σ_0^M	μ^M	λ
57.0	21.6	4.9	150	20	20	340	6.3	18.0
(GPa)	(GPa)	(%)	(MPa)	(MPa)	(MPa)	(MPa)	(MPa · K ⁻¹)	(W · m ⁻¹ · K ⁻¹)
ρ	E_R	γ_R	δ^{min}	δ^{max}	R^{max}	σ_0^R	μ^R	C_p
6450	40.4	0.25	15	15	220	156	13.45	500
(kg · m ⁻³)	(GPa)	(%)	(MPa)	(MPa)	(MPa)	(MPa)	(MPa · K ⁻¹)	(J · K ⁻¹ · kg ⁻¹)

2.3.2. Strain localization along the NiTi wire

As the wire model was reduced to one dimension to restrict the computational time, the strain localization effect (associated with 3D effects) along the wire had to be considered by other means. To take into account the propagation of martensitic transformation bands, a non-local model was implemented using the Finite Element method [43]. 32 thermomechanical two-node truss elements were used and assembled as presented in Figure 4. The analysis presented in the “Results and discussion” section focuses on three reference positions associated with elements 2, 4 and 12.

**Figure 4.** Three reference positions along the numerical wire.

Instead of using the nominal stress σ in the material behavior law, an apparent stress value σ_{app} was computed for each element. It enabled us to take into account the effect of the high shear stress values at the interface between phases, in addition to the tensile stress value. Thus, it was assumed that the propagation was driven by the maximal stress value at the interface between a wire portion of martensite and a wire portion of austenite. The apparent stress of a given element m was calculated using a stress intensity factor $K_I(m)$:

$$\sigma_{app}(m) = \sigma K_I(m) \quad (2.3)$$

By assuming a linear bi-material perfectly bonded cylinder to represent the stress intensity at the interface between these two portions, the value of K_I should be a function of the stiffness properties on both sides of the interface [44]. To facilitate the convergence of the model and to consider the specific case of the element m ($1 < m < 32$), a function K^*I of z_{Mm} , z_{Mm-1} and z_{Mm+1} the martensite volume fraction of the element m and its neighbors $m-1$ and $m+1$, respectively, was introduced:

$$K_I^*(m) = 1 + \max(\langle z_{m+1}^M - z_m^M \rangle, \langle z_{m-1}^M - z_m^M \rangle) (K_I^0 - 1) \quad (2.4)$$

Where $\{x\}$ is equal to x if $x \geq 0$ and is equal to 0 if $x < 0$. Thus, $K^*I(m) = 1$ if the m element is in the same state as its direct neighbors, and $K^*I(m) = K_I^0$ if the m element is in the austenitic state and one of its neighbors is fully martensitic. The constant value of $K_I^0 = 1.6$ was chosen, in agreement with the results presented in [29]. Since bands propagation has never been observed in the case of R-phase transformation, the R-phase volume fraction was not considered in Eq 2.4.

In order to study the effect of the clamping of the jaws on the stress at the ends of the wire, it can be assumed that the wire corresponds locally to a solid cylinder subjected to an external pressure. Thus, the calculation of radial and orthoradial stresses from Lamé's equations allows to show that ' clamping under a pressure of P_0 induces a reduction of the equivalent Von Mises stress by a stress corresponding to P_0 [45]. The consequence is that the tightening effect in the jaws can be simulated in a uniaxial model by increasing the initial axial stress value of the elements placed at the two ends of the wire. To respect forces equilibrium and to avoid any technical issues, it was preferred to decrease the transformation yield stresses in these two elements (n° 1 and 32). The values of $\sigma_{M,R} = 0 - 100\text{MPa}$ was retained to ensure an initial state without martensite.

The model was validated by a force-imposed tensile test to the maximal value of 2600 N, over a cycle with a frequency of 3 Hz, which is an order of magnitude equivalent to the first modal frequency of the cable. The results are presented in Figure 5a,b. Figure 5a confronts the numerical stress-strain curve to the experimental one by considering strain localization or not. Figure 5b presents the local mechanical behavior observed numerically in several elements along the wire, for the configuration where strain localization was considered.

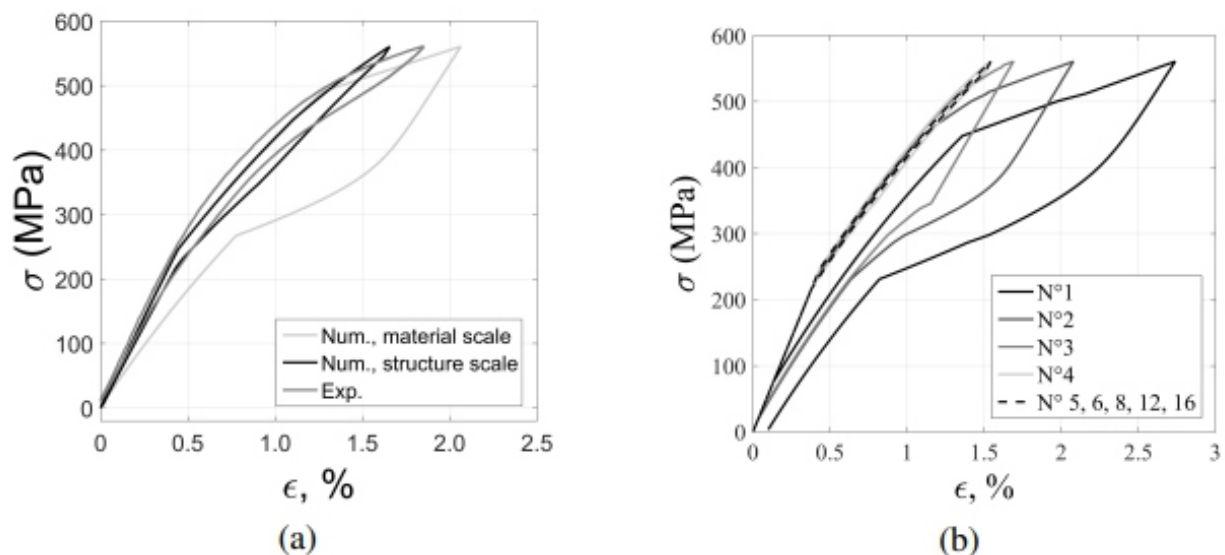


Figure 5. (a) Stress-strain curve for a force-imposed test by considering bands propagation (wire scale) or no propagation (material scale); (b) corresponding behavior of several elements along the wire structure.

From Figure 5a, the prediction of mechanical behavior was improved by considering strain localization. Due to the propagation of the martensitic transformation bands from the anchorages, the closer the elements to the anchorages, the more they experienced martensitic transformation (see Figure 5b). However, all the elements experienced R-phase transformation. In particular, elements 5 to 16 (and their symmetrical elements 17 to 28) underwent only this intermediate transformation, which resulted in thin hysteresis loops.

2.3.3. Numerically studied configurations

Table 2 presents the five studied configurations confronted in this paper. These configurations represent different levels of complexity: configuration 1 is associated with an elastic behavior of the damper (material in a pure austenitic state), while configuration 5 is associated with a superelastic behavior taking all the identified phenomena into account. All the retained configurations are presented succes

sively to discuss the contribution of each added phenomenon.

Table 2. Studied material configurations.

Configuration	Superelasticity	R-phase	Thermal effects	Strain localization	Number of elements for the damper
1	n	n	n	n	1
2	y	n	n	n	1
3	y	y	n	n	1
4	y	y	y	n	1
5	y	y	y	y	32

2.4. Post-processing

To carefully analyze the influence of the material behavior of the NiTi wires embedded in the damper on the dynamic response of the whole cable structure, it was necessary to select relevant indicators related to both scales.

First, the dynamic response of the cable was investigated. Equation 2.5 is the general form of the cable transverse displacement law $y(x, t)$, which assumes heterogeneous properties along the cable due to a punctual influence of the damping device [41].

$$y(x, t) = \sum_{n=1}^N C_n(x, t) \sin\left(\frac{n\pi x}{L}\right) \sin\left(2\pi f_n(x, t) \sqrt{1 - \xi_n^2(x, t)} t + \phi_n(x, t)\right) \exp(-2\pi f_n(x, t) \xi_n(x, t) t) \quad (2.5)$$

With f_n the natural frequency, ξ_n the damping ratio, C_n the modal contribution in the time domain, ϕ_n the phase related to each mode n . The following modal parameters (identified from Eq 2.5) were computed over time, as in [41]:

- $f_1(x, t)$, the natural frequency related to the first vibration mode by applying a Wigner-Ville transform on the transverse displacement signal at $x = L/2$, using a Matlab toolbox provided by [46],
- $\xi_1(x, t)$, the damping ratio related to the first vibration mode by plotting $\ln(\text{env}(y_1))$ the logarithm of the signal envelop after numerical filtering to isolate the first mode: the damping ratio changes correspond to the slope changes on the computed curve.

The beginning of the curves presented later were affected by side effects due to numerical filtering. Secondly, an investigation based on the material behavior performed numerically was carried. Thus, the changes in material temperature T and volume fraction of the phases (z_M and z_R) were plotted.

The loss factor was computed from strain-stress numerical values over time to quantify the damping capacity of the material. It is linked to the material dissipated energy (through ΔW corresponding to the hysteresis loop area on the stress-strain curve) and the strain energy (through W corresponding to the area below the transformation path on the same curve), after Eq 2.6 [47].

$$\eta = \frac{1}{2\pi} \frac{\Delta W}{W - \frac{1}{2}\Delta W} \quad (2.6)$$

One can say that the loss factor does not directly correspond to the damping ratio computed from the cable displacement signal, even if both are naturally linked. However, it is a precious indicator to identify the different potential damping regimes.

3. Results and discussion

In this section, the five considered configurations are presented in the reference study case. For each configuration, the transverse displacement of the cable at $L/2$ (damper and deviating force position) numerically obtained was compared to the experimental signal for 20 s from the moment the force is released. The corresponding material behavior is presented for three arbitrarily chosen time windows: (i) [0–1] s, (ii) [2–3.5] s, (iii) [19–20] s. The window of [2–3.5] s corresponded approximately to the transition between the two first damping regimes, whatever the configuration. Since temperature has a great influence on NiTi behavior, it is important to specify that all the tests were performed at a testing temperature of about 20 °C (± 2 °C).

The signals were centered on the “zero” value, which means that the cable remained at a displacement value of zero before any deviating force application. In the particular case where the wires would have not been pre-strained, the positive values of the transverse displacement measured at the damper position would have corresponded to activation stages of the device. On the contrary, negative values would have been associated with deactivation stages. By pre-straining the wires, the transition associated with the deactivation of the device is expected to be shifted to the negative values. For an initial elongation of 4 mm, this transition should be close to the value of -4 mm.

To focus the analysis on the influence of the behavior of the NiTi wires on the damping capacity of the device, the study case of reference is presented in this section and the attention is paid on the cable displacement at the force and damper position. Additional results associated with the dynamic response along the cable for the different study cases are presented in the Appendixes.

3.1. Influence of thermal effects and R-phase transformation (configurations 2, 3, 4/study case 1)

3.1.1. Results

Figures 6, 7a, 8a and 9a provide the transverse displacement of the cable at $L/2$, for configurations 1, 2, 3 and 4, respectively. The material behavior associated with the “numerical damper” is given in Figures 7b–d, 8b–d, and 9b–d, for configurations 2, 3 and 4, respectively. From Figure 6, the experimental signal illustrates a high and quite regular decrease in displacement amplitude. The cable almost reached equilibrium after 20 s following the release of the force.

By considering an elastic behavior of the numerical damper (configuration 1), no energy was dissipated. Thus, the damping capacity provided by the numerical damper was almost zero, accordingly (see Figure 6). The small damping observable was due to the intrinsic damping of the cable. However, the additional stiffness of the elastic damper enabled to “cut” the signal parts associated with the activation stages of the damper, while the signal parts associated with the deactivation stages were not affected. Eventually, the displacement amplitude was decreased compared to the configuration without any damping device (see Figure 1a) but the dynamic response obtained numerically did not reproduce the experimental signal.

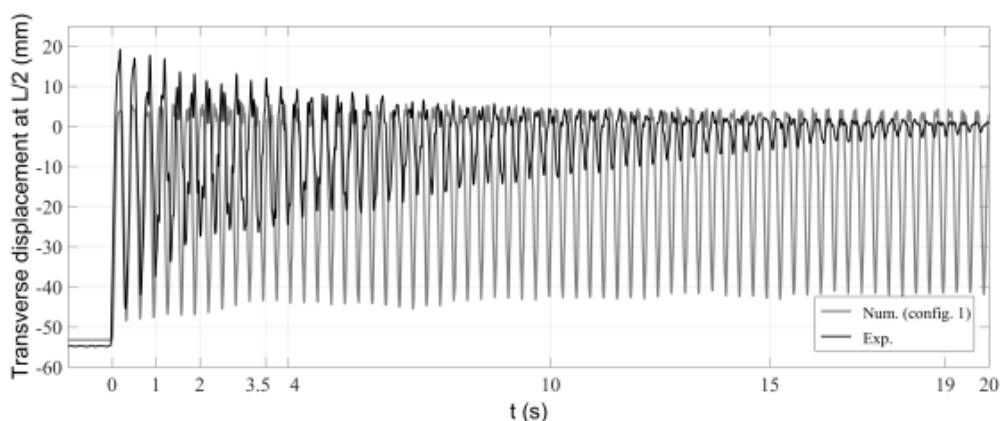


Figure 6. Transverse displacement of the cable at L/2 equipped with a damper (study case 1/configuration 1) placed at L/2.

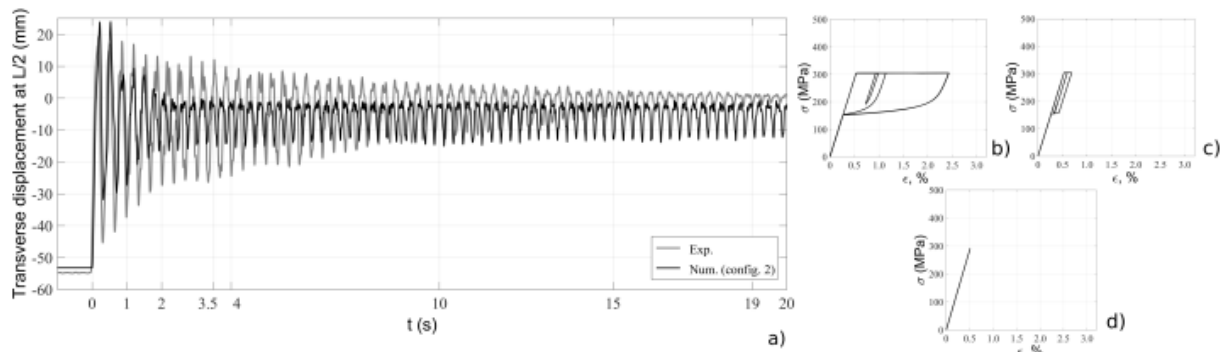


Figure 7. (a) Transverse displacement of the cable at L/2 equipped with a damper (study case 1/configuration 2) placed at L/2; Stress-Strain curves related to the behavior of the material embedded in the damper: (b) [0, 1]s, (c) [2, 3.5]s, (d) [19, 20]s.

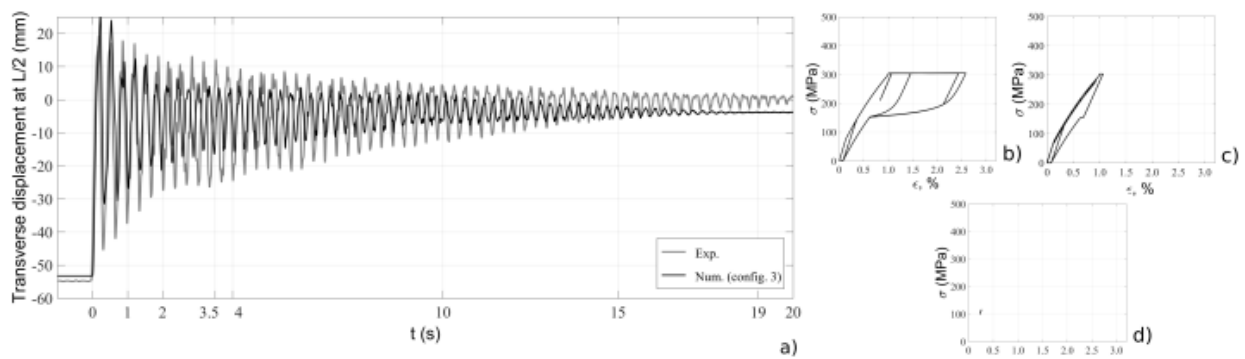


Figure 8. (a) Transverse displacement of the cable at L/2 equipped with a damper (study case 1/configuration 3) placed at L/2; Stress-Strain curves related to the behavior of the material embedded in the damper: (b) [0, 1]s, (c) [2, 3.5]s, (d) [19, 20]s.

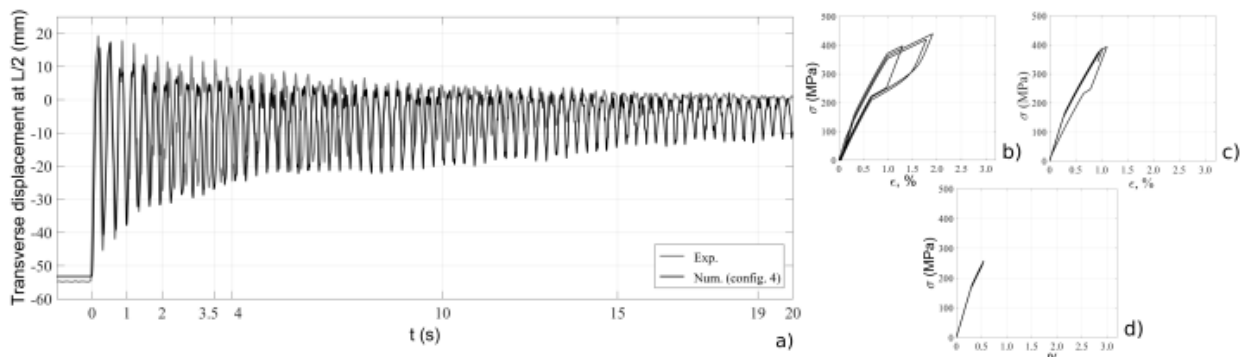


Figure 9. (a) Transverse displacement of the cable at L/2 equipped with a damper (study case 1/configuration 4) placed at L/2; Stress-Strain curves related to the behavior of the material embedded in the damper: (b) [0, 1]s, (c) [2, 3.5]s, (d) [19, 20]s.

By considering the superelasticity effect (configuration 2), a strong mitigation of the cable amplitude was observed within the first 3 s following the force release (see Figure 7a). After this first damping stage, the displacement amplitude remained constant (“undamped stage”). These observations are in agreement with the corresponding behavior of the wire. The first stage was associated with transformation into martensite (see Figure 7b,c). Once the amplitude was associated with a maximal stress value inferior to the martensite transformation yield stress value, the amplitude remained almost constant (see Figure 7d). Eventually, the response prediction was greatly improved compared to configuration 1. However, the damping capacity was overestimated during the first part of the signal and underestimated during the following part.

By considering the intermediate R-phase transformation (configuration 3), the first damping stage observed in the previous configuration was affected and an intermediate damping stage appeared, as highlighted in Figure 8a. During the first stage, austenite transformed into R-phase before martensite appearance over the loading cycles: for a given level of wire elongation, the dissipated energy decreased when compared to a material without R-phase transformation (see Figure 8b,c). In the second stage, once the loading amplitude corresponded to a maximal stress value inferior to the martensitic transformation yield stress value, the R-phase transformation still operated alone. It explains why a second and low damped stage appeared. Furthermore, the yield stress value associated with the transformation into R-phase is low at room temperature (inferior to 100 Mpa). Thus, stabilization of the cable was achieved after 20 s following the force release. One can observe that the final material state obtained numerically corresponded to an elastic behavior associated with a mixture of austenite and R-phase, due to the NiTi wires pre-strain (see Figure 8d). Due to this pre-strain, the final undamped stage was not observed unlike in configuration 2: the fully austenite elastic state could not be reached. Eventually, damping capacity was overestimated during the whole signal, although it has decreased during the first damping stage compared to configuration 2.

By considering the thermal effects (configuration 4), the first and second damping stages observed previously still operated but their respective damping capacity decreased compared to configuration 3 (see Figure 9a). From Figure 9b,c, the combination of thermomechanical couplings and intrinsic dissipation involved an increase in both martensitic plateau slope and martensitic transformation yield stress. Considering the present material, a decrease in damping performance under these loading conditions (frequency and amplitude) is in agreement with results reported in [15]. The combination of both transformation into R-phase and thermal effects provided a much better prediction of the first damping stage (see Figure 9a) compared to the previous configurations. However, the second damping stage was underestimated, despite R-phase transformation.

3.1.2. Discussion

Figure 10a–c provides zM , zR and T changes over time, while Figure 11a–c compares f_l , $\ln(\text{env}(y_l))$ (from the cable scale) and η (from the material scale) for configurations 2 to 4. For reasons of readability, only the first 10 s are plotted, in what follows.

From Figure 10a, no martensite appeared after $t = 4$ s, whatever the configuration. From Figure 10a,b, less martensite appeared when R-phase was taken into account (as reflected by a lower maximal martensite volume fraction in configurations 3 and 4). By considering R-phase transformation, the latter was observed at least during the first 10 s after the force release, in both configurations 3 and 4. These comments directly explain why a lower damping ratio during the first damping stage and a higher damping ratio during the next one were observed in configuration 3 compared to configuration 2. In configuration 4, phase transformations naturally entailed material temperature changes (see Figure 10c): in the first stage, quite high thermal variations associated with the latent heat of the martensitic transformation and a self-heating due to intrinsic dissipation were observed in parallel. The temperature

logically inhibited the transformation of austenite into R-phase and martensite by increasing the associated transformation yield stresses (see Figure 10a). In the second stage, lower thermal variations (mainly due to the thermomechanical couplings associated with transformation into R-phase only) were highlighted. However, the intrinsic dissipation associated with the intermediate transformation did no longer override thermal exchanges with the surroundings: a return to the thermal equilibrium was therefore observed. This decrease in temperature favored occasional martensite formation and maintained the amount of R-phase approximatively constant, as observed in Figure 10a,b.

From Figure 11a, a large gap can be measured between the frequency values obtained numerically by configuration 2 on one hand, and configurations 3 and 4 on the other hand. This is probably due to a difference in additional stiffness brought to the cable, associated with transformation into R-phase in the NiTi wires. Indeed, the latter was not considered in configuration 2. Another large gap can be measured between the frequency values obtained numerically in configurations 3 and 4 and the experimental values. That could be due to the fact that the stiffness associated with the mechanical parts clamped to the ground and to the moving cable (see device in Figure 2a) were not considered in the modeling. Indeed, these parts are deformable and not infinitely stiff. This should not entail significant consequences on the damping prediction because the strain rates experienced by the NiTi wires remained of the same order of magnitude. This is why the attention should be only paid on the relative increases in frequency values. The frequency changes were best reproduced by configuration 4, where a smooth increase in f_1 was observed. It can be explained by a better prediction of the behavior of the embedded material compared to configurations 2 and 3, and consequently by a better prediction of the stiffness added to the cable.

From Figure 11b,c, a first damping stage can be clearly identified from 0 to about 3–4 s in configurations 2 and 3, from the point of view of both the vibrating structure ($\ln(\text{env}(y_1))$) and the material behavior (η). It directly corresponds to the transformation into martensite. Without taking R-phase into account, the first damping stage was followed by an undamped stage, where the material behavior became elastic (configuration 2). A better prediction of the damping capacity was observed in the second damping stage thanks to R-phase transformation, that occurred at least 10 s after the force release and induced a low but non zero energy dissipation (configuration 3). From Figure 11b,c, damping capacity was more distributed over time in configuration 4, by taking into account thermal effects that smoothed the damping ratio changes. Eventually, a better prediction of the damping capacity is also observed in configuration 4.

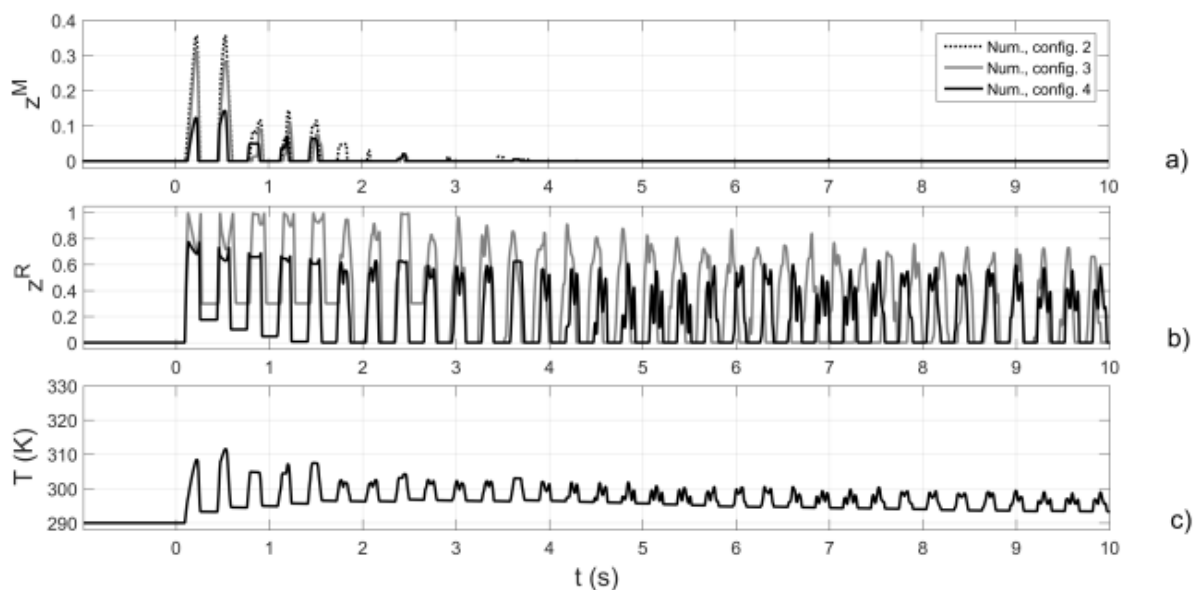


Figure 10. Comparison between configurations 2, 3, 4: (a) martensite volumic fraction; (b) R-phase volumic fraction; (c) material temperature.

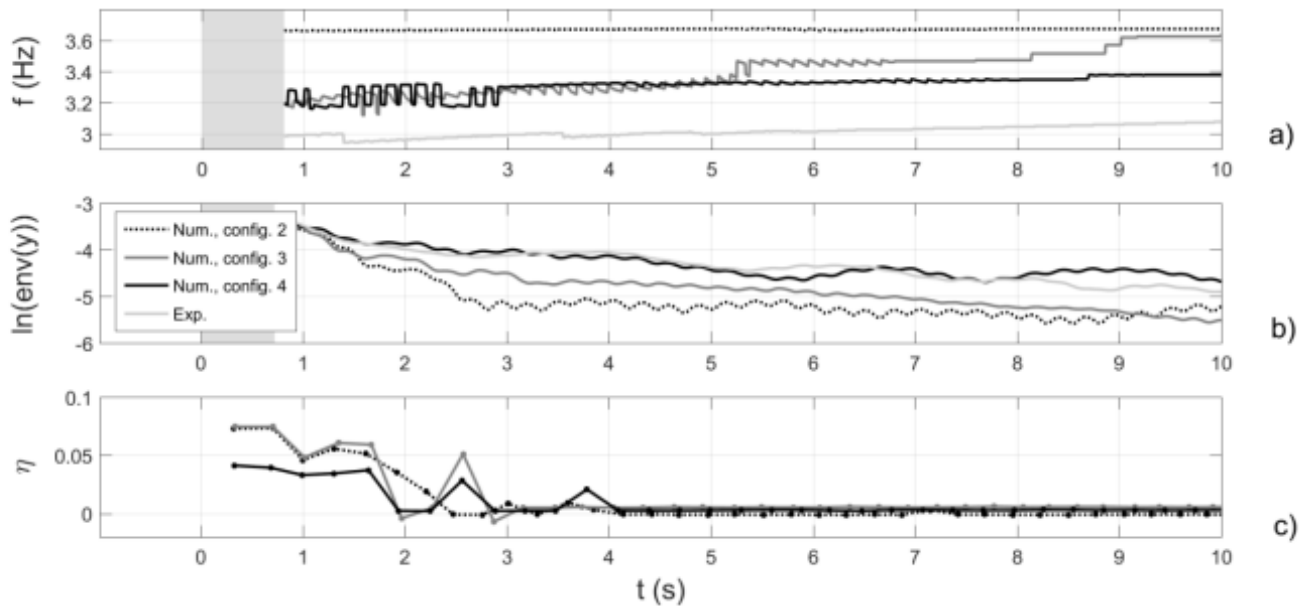


Figure 11. Comparison between configurations 2, 3, 4: (a) frequency of the 1st mode; (b) logarithm of the signal envelop; (c) loss factor η .

Up to this point, configuration 4 provided the best prediction, while the computing time was reasonable since the numerical damper consisted of one truss element only. The next and last configuration should improve the prediction but should also require more computational resources, by splitting the numerical damper into 32 truss elements to take the strain localization phenomenon into account. Thus, configuration 4 should be seriously considered for further works, regardless of the results associated with configuration 5.

3.2. Influence of strain localization (configuration 4, 5/study case 1)

3.2.1. Results

Figure 12a provides the transverse displacement of the cable at $L/2$ for configuration 5, while the material behavior associated with the “numerical damper” is presented for three elements along the wire (see Figure 4) in Figure 12b–d. The macroscopic behavior resulting from the contribution of all the elements along the wire is given in Figure 12e.

Configuration 5 provided by far the best agreement with the transverse displacement signal obtained experimentally (see Figure 12a), despite a small gap at the end of the signal due to a possible accumulation of residual strain in the wires (blocked martensite) as the experiments progressed. The obtained macroscopic behavior of the wire was much smoother than material behaviors observed in the previous configurations, due to the average of the local behaviors. Furthermore, the transitions between the different damping regimes are difficult to identify, as in the experimental signal. From Figure 12b,c, the dissipated energy was locally high at the extremities of the wire compared to the average dissipated energy (see Figure 12e) or to the dissipated energy obtained from the single “damper” element in configuration 4 (see Figure 9b). It is quite easy to explain: the transformation bands propagated from the extremities of the wires. This point is very important and highlights an advantage of configuration 5 over configuration 4: taking into account heterogeneities in the thermomechanical behavior along the wire

enables to better predict the maximal stress and dissipated energy values experienced by the wires to therefore estimate the fatigue life of the damping device. It would be a great assistance to optimize the design of the damper. Eventually, the last configuration improved the vibrating response of the whole system.

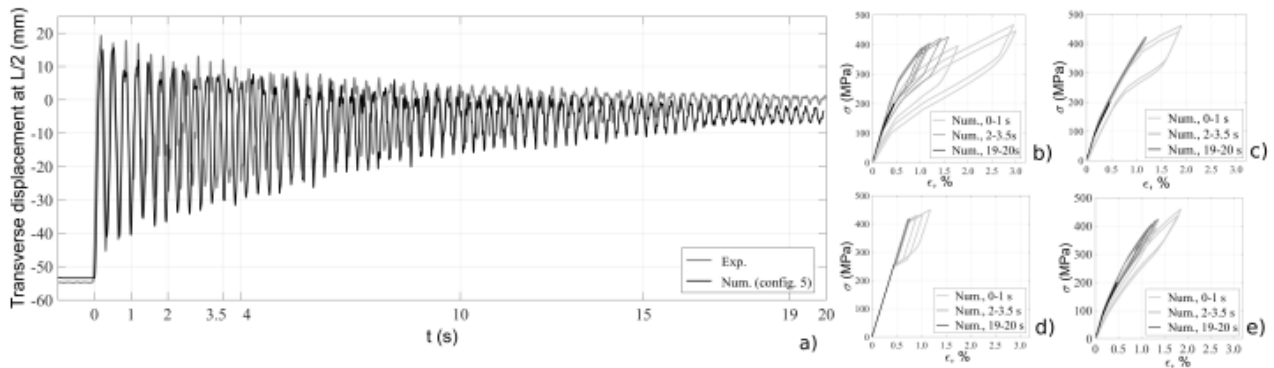


Figure 12. (a) Transverse displacement of the cable at $L/2$ equipped with a damper (study case 1/configuration 5) placed at $L/2$; Stress-Strain curves related to the local behavior of the material embedded in the damper at three reference positions: (b) element n° 2, (c) n° 4, (d) n° 12, (e) macroscopic behavior of the wire.

3.2.2. Discussion

Figure 13a–c provides z_M , z_R and T changes over time, while Figure 14a–c compares f_l , $\ln(\text{env}(y_1))$ (from the structure point of view) and η (from the material point of view), for configurations 4 and 5. In configuration 5, only values associated with the same elements as those described previously are presented. One can add that η was computed from the macroscopic behavior of the whole wire in configuration 5.

From Figure 13a, the elements that are close to the anchorages experienced more martensite transformation (and therefore dissipated more energy), since propagation of transformations bands was restricted to a very limited wire portion: due to high strain rate values, a high increase in temperature near the transformation fronts inhibited transformation into martensite beyond the front. It is confirmed by higher maximal martensite volume fraction and temperature values in element 2 for configuration 5, than in the single element for configuration 4.

This strain localization explains the decrease in damping capacity provided by configuration 5 compared to configuration 4, as observed in Figure 14a–c. Indeed, the material heterogeneity induced a distribution of the damping capacity over time. In particular, the transitions between the distinct damping regimes in configuration 4 are no longer observable in configuration 5, according to the changes in damping ratio and loss factor highlighted in Figure 14b,c. However, no significant improvement of the stiffness and damping ratio in the prediction over time was provided by configuration 5. Eventually, the main difference between configurations 4 and 5 lies in the prediction of the local behavior of the material in order to study its damage and fatigue life.

In order to fully validate the numerical tool, it was necessary to study the response of the cable at positions different from that of the damper. The two others study cases and additional results regarding the reference study case are briefly presented in Appendixes. Both configurations 4 and 5 showed good agreements with the experimental curves.

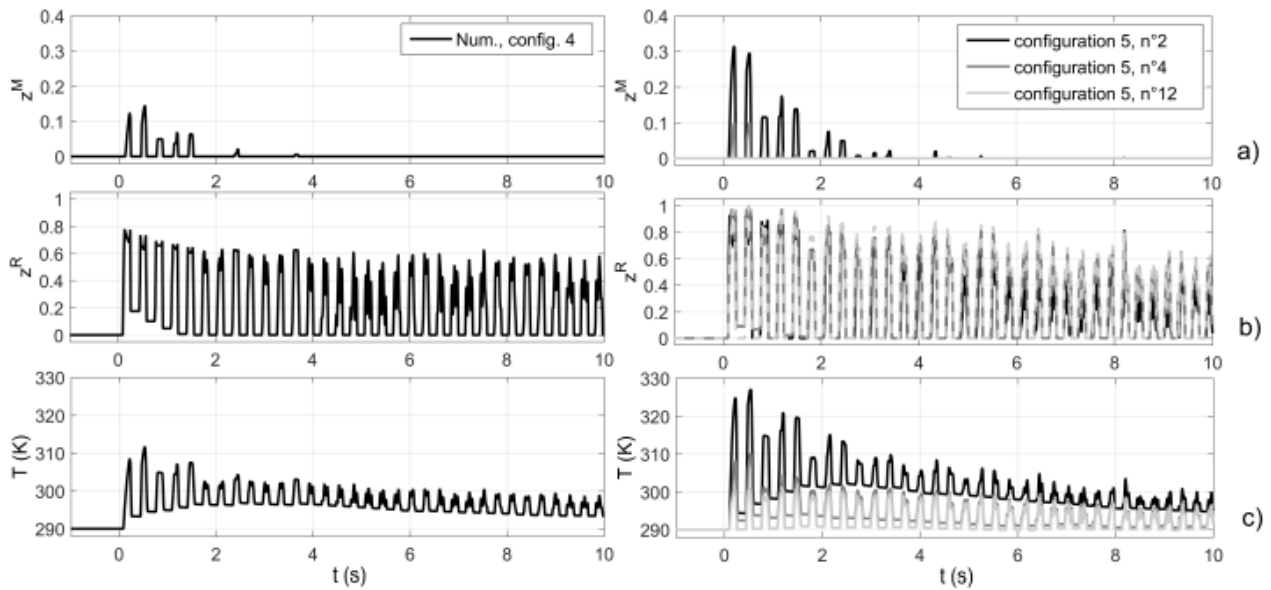


Figure 13. Comparison between configurations 4 and 5: (a) martensite volumic fraction; (b) R-phase volumic fraction; (c) material temperature.

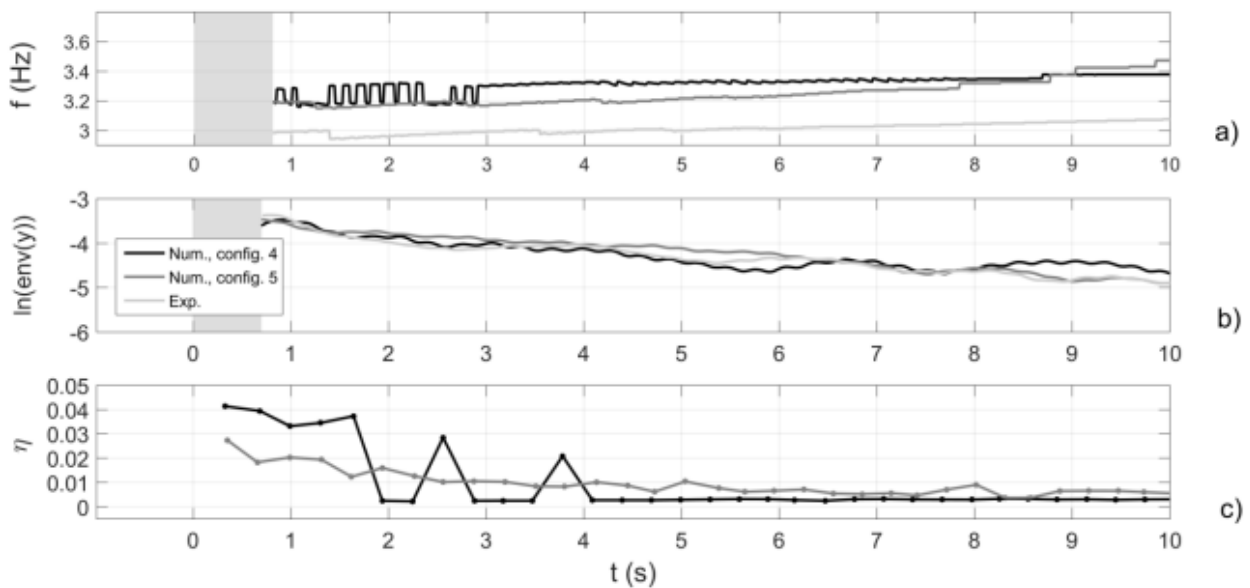


Figure 14. Comparison between configurations 4 and 5: (a) frequency of the 1st mode; (b) logarithm of the signal envelop; (c) loss factor η .

4. Conclusions

In conclusion, the following points can be highlighted:

- A numerical tool was developed to predict the dynamic response of a cable equipped with a NiTi wire-based damping device and was validated using three study cases (where the contribution of the different modes was different).
- In particular, the influence of the material behavior of the NiTi wires embedded in the damping device was investigated. To do this, several configurations taking into account the phenomena that influence the energy dissipated by these wires were studied. The importance of taking both the thermal effects, the intermediate R-phase transformation and the strain localization into account was demonstrated.

• Two configurations (4 and 5) that proved to be the best to predict damping capacity of the damper were studied in detail. Their respective interest was discussed. For instance, configuration 4 (thermal effects and intermediate R-phase transformation) requires less computing resources and can be used to optimize the damping setting-up (by acting on the effective length and number/section of the wires, pre-strain of the wires, position of the damping device along the cable), since these optimization procedures are computationally intensive. Configuration 5 that takes propagation of transformation bands into account in addition to the previous phenomena provided a better description of the material behavior along the wire by discretizing it into several elements. It can roughly be used for optimization, but the fatigue life of the embedded wires can be considered to dimension the device regarding its service life, in addition to its effectiveness.

Several perspectives have been identified to pursue this work:

- More realistic loading cases experienced by cables should be studied, such as harmonic or random forced loadings, punctual or distributed heterogeneously along the cable.
- The numerical tool should be used to define the tuning of the damping device setting-up according to the constraints of a given structure (angle of the cable chord, natural frequency of the cable, kind of solicitations).
- The link between the dissipated energy by NiTi alloys and their fatigue resistance should be investigated to be considered in the optimization of NiTi-based damping devices.
- Heterogeneity of the material behavior (due to propagation of transformation bands) should be investigated to optimize damping capacity and fatigue resistance. For instance, periodic localized cross-section decrease and/or stress increase, modification of clamping system or well-suited thermomechanical training could be considered.

Acknowledgments

To Daniel Bruhat, Richard Michel, Jean-François David and Yannick Falaise (MAST/Université Gustave Eiffel) for their participation in the experimental set-up, the development of the damping device and the measurements.

Conflict of interest

The authors declare that they have no known competing financial interests or personal relationships that could have appeared to influence the work reported in this paper.

References

1. Ungar EE, Kerwin EM (1962) Loss factors of viscoelastic systems in terms of energy concepts. *J Acoust Soc Am* 34: 954–957. <https://doi.org/10.1121/1.1918227>
2. Cai J, Mao S, Liu Y, et al. (2022) Nb/NiTi laminate composite with high pseudoelastic energy dissipation capacity. *Mater Today Nano* 19: 100238. <https://doi.org/10.1016/j.mtnano.2022.100238>
3. Oliveira JP, Zeng Z, Berveiller S, et al. (2018) Laser welding of Cu–Al–Be shape memory alloys: Microstructure and mechanical properties. *Mater Design* 148: 145–152. <https://doi.org/10.1016/j.matdes.2018.03.066>
4. Patoor E, Berveiller M (1994) *Les Alliages à Mémoire de Formes*, Hermes.
5. Otsuka K, Wayman C (1998) *Shape Memory Materials*, Cambridge: Cambridge University Press.
6. Udovenko VA (2003) Damping, In: Brailovski V, Prokoschkin S, Terriault P, et al., *Shape Memory Alloys Fundamentals, Modelling and Applications*, University of Quebec, Montreal, Canada, 279–309.
7. Orgeas L, Favier D (1998) Stress-induced martensitic transformation of a NiTi alloy in isothermal shear, tension and compression. *Acta Mater* 46: 5579–5591.
8. Menna C, Auricchio F, Asprone D (2014) *Application of shape memory alloys in structural engi-*

- neering, In: Lecce L, Concilio A, *Shape Memory Alloy Engineering: for Aerospace, Structural and Biomedical Applications*, Elsevier; 369–403. <https://doi.org/10.1016/B978-0-08-099920-3.00013-9>
9. Matsumoto M, Daito Y, Kanamura T, et al. (1998) Wind-induced vibration of cables of cable-stayed bridges. *J Wind Eng Ind Aerod* 74: 1015–1027. [https://doi.org/10.1016/S0167-6105\(98\)00093-2](https://doi.org/10.1016/S0167-6105(98)00093-2)
10. Dieng L, Helbert G, Arbab Chirani S, et al. (2013) Use of shape memory alloys damper device to mitigate vibration amplitudes of bridge cables. *Eng Struct* 56: 1547–1556. <https://doi.org/10.1016/j.engstruct.2013.07.018>
11. Nespoli A, Rigamonti D, Riva M, et al. (2016) Study of pseudoelastic systems for the design of complex passive dampers: static analysis and modeling. *Smart Mater Struct* 25: 105001. <https://doi.org/10.1088/0964-1726/25/10/105001>
12. Tobushi H, Shimeno Y, Hachisuka T, et al. (1998) Influence of strain rate on superelastic properties of TiNi shape memory alloys. *Mech Mater* 30: 141–150. [https://doi.org/10.1016/S0167-6636\(98\)00041-6](https://doi.org/10.1016/S0167-6636(98)00041-6)
13. Liu Y, Favier D (2000) Stabilisation of martensite due to shear deformation via variant reorientation in polycrystalline NiTi. *Acta Mater* 48: 3489–3499. [https://doi.org/10.1016/S1359-6454\(00\)00129-4](https://doi.org/10.1016/S1359-6454(00)00129-4)
14. Bouvet C, Calloch S, Lexcellent C (2004) A phenomenological model for pseudoelasticity of shape memory alloys under multiaxial proportional and nonproportional loadings. *Eur J Mech A-Solid* 23: 37–61. <https://doi.org/10.1016/j.euromechsol.2003.09.005>
15. Helbert G, Saint-Sulpice L, Arbab Chirani S, et al. (2014) Experimental characterisation of three-phase NiTi wires under tension. *Mech Mater* 79: 85–101. <https://doi.org/10.1016/j.mechmat.2014.07.020>
16. Zhu S, Zhang Y (2007) A thermomechanical constitutive model for superelastic SMA wire with strain-rate dependence. *Smart Mater Struct* 16: 1696. <https://doi.org/10.1088/0964-1726/16/5/023>
17. Heintze O, Seelecke S (2008) A coupled thermomechanical model for shape memory alloys-From single crystal to polycrystal. *Mater Sci Eng A-Struct* 481–482: 389–394. <https://doi.org/10.1016/j.msea.2007.08.028>
18. Shariat BS, Liu Y, Rio G (2012) Thermomechanical modelling of microstructurally graded shape memory alloys. *J Alloys Compd* 541: 407–414. <https://doi.org/10.1016/j.jallcom.2012.06.027>
19. Xiao Y, Zeng P, Lei L (2019) Micromechanical modelling on thermomechanical coupling of superelastic NiTi alloy. *Int J Mech Sci* 153–154: 36–47. <https://doi.org/10.1016/j.ijmecsci.2019.01.030>
20. Otsuka K, Ren X (2005) Physical metallurgy of Ti-Ni-based shape memory alloys. *Prog Mater Sci* 50: 511–678. <https://doi.org/10.1016/j.pmatsci.2004.10.001>
21. Oliveira JP, Mirande RM, Braz Fernandez FM (2017) Welding and joining of NiTi shape memory alloys: A review. *Prog Mater Sci* 88: 412–466. <https://doi.org/10.1016/j.pmatsci.2017.04.008>
22. Sittner P, Sedláček P, Landa M, et al. (2006) In situ experimental evidence on R-phase related deformation processes in activated NiTi wires. *Mater Sci Eng A-Struct* 438–440: 579–584. <https://doi.org/10.1016/j.msea.2006.02.200>
23. Sengupta A, Papadopoulos P (2009) Constitutive modeling and finite element approximation of B2-R-B19' phase transformations in Nitinol polycrystals. *Comput Method Appl M* 198: 3214–3227. <https://doi.org/10.1016/j.cma.2009.06.004>
24. Sedláček P, Frost M, Benešová B, et al. (2012) Thermomechanical model for NiTi-based shape memory alloys including R-phase and material anisotropy under multi-axial loadings. *Int J Plast* 39: 132–151. <https://doi.org/10.1016/j.ijplas.2012.06.008>
25. Rigamonti D, Nespoli A, Villa E, et al. (2017) Implementation of a constitutive model for different annealed superelastic SMA wires with rhombohedral phase. *Mech Mater* 112: 88–100. <https://doi.org/10.1016/j.mechmat.2017.06.001>
26. Zhou T, Yu C, Kang G, et al. (2020) A crystal plasticity based constitutive model accounting for R

- phase and two-step phase transition of polycrystalline NiTi shape memory alloys. *Int J Solids Struct* 193–194: 503–526. <https://doi.org/10.1016/j.ijsolstr.2020.03.001>
27. Shaw JA, Kyriakides S (1995) Thermomechanical aspects of NiTi. *J Mech Phys Solids* 43: 1243–1281. [https://doi.org/10.1016/0022-5096\(95\)00024-D](https://doi.org/10.1016/0022-5096(95)00024-D)
28. Favier D, Louche H, Schlosser P, et al. (2007) Homogeneous and heterogeneous deformation mechanisms in an austenitic polycrystalline Ti-50.8 at% Ni thin tube under tension. Investigation via temperature and strain fields measurements. *Acta Mater* 55: 5310–5322. <https://doi.org/10.1016/j.actamat.2007.05.027>
29. Sedmak P, Pilch J, Heller L, et al. (2016) Grain-resolved analysis of localized deformation in nickel-titanium wire under tensile load. *Science* 353: 559–562. <https://doi.org/10.1126/science.aad6700>
30. He YJ, Sun QP (2010) Rate-dependent domain spacing in a stretched NiTi strip. *Int J Solids Struct* 47: 2775–2783. <https://doi.org/10.1016/j.ijsolstr.2010.06.006>
31. Shariat BS, Bakhtiari S, Yang H, et al. (2020) Controlled initiation and propagation of stress-induced martensitic transformation in functionally graded NiTi. *J Alloys Compd* 851: 156103. <https://doi.org/10.1016/j.jallcom.2020.156103>
32. Sun QP, Zhong Z (2000) An inclusion theory for the propagation of martensite band in NiTi shape memory alloy wires under tension. *Int J Plast* 16: 1169–1187. [https://doi.org/10.1016/S0749-6419\(00\)00006-1](https://doi.org/10.1016/S0749-6419(00)00006-1)
33. Chan CW, Chan SHJ, Man HC, et al. (2012) 1-D constitutive model for evolution of stress-induced R-phase and localized Luders-like stress-induced martensitic transformation of super-elastic NiTi wires. *Int J Plast* 32–33: 85–105. <https://doi.org/10.1016/j.ijplas.2011.12.003>
34. Soul H, Yawny A (2013) Thermomechanical model for evaluation of the superelastic response of NiTi shape memory alloys under dynamic conditions. *Smart Mater Struct* 22: 035017. <https://doi.org/10.1088/0964-1726/22/3/035017>
35. Xiao Y, Jiang D (2020) Constitutive modelling of transformation pattern in superelastic NiTi shape memory alloy under cyclic loading. *Int J Mech Sci* 182: 105743. <https://doi.org/10.1016/j.ijmecsci.2020.105743>
36. Zuo XB, Li AQ (2011) Numerical and experimental investigation on cable vibration mitigation using shape memory alloy damper. *Struct Control Health Monit* 18: 20–39.
37. Ben Mekki O, Auricchio F (2011) Performance evaluation of shape-memory-alloy superelastic behavior to control a stay cable in cable-stayed bridges. *Int J Non-Linear Mech* 46: 470–477. <https://doi.org/10.1016/j.ijnonlinmec.2010.12.002>
38. Torra V, Auguet C, Isalgue A, et al. (2013) Built in dampers for stayed cables in bridges via SMA. The SMARTeR-ESF project: A mesoscopic and macroscopic experimental analysis with numerical simulations. *Eng Struct* 49: 43–57. <https://doi.org/10.1016/j.engstruct.2012.11.011>
39. Morse P, Ingard K (1968) *Theoretical Acoustics*, Princeton University Press.
40. MSC (2008) *Marc/mentat volume A: Theory and user information*.
41. Helbert G, Dieng L, Arbab Chirani S, et al. (2018) Investigation of NiTi based damper effects in bridge cables vibration response: Damping capacity and stiffness changes. *Eng Struct* 165: 184–197. <https://doi.org/10.1016/j.engstruct.2018.02.087>
42. Helbert G, Saint-Sulpice L, Arbab Chirani S, et al. (2017) A uniaxial constitutive model for superelastic NiTi SMA including R-phase and martensite transformations and thermal effects. *Smart Mater Struct* 26: 025007. <https://doi.org/10.1088/1361-665X/aa5141>
43. Helbert G (2014) Contribution à la durabilité des câbles de Génie Civil vis-à-vis de la fatigue par un dispositif amortisseur à base de fils NiTi, Université de Bretagne Sud.
44. Qian ZQ, Akisanya AR (1999) An investigation of the stress singularity near the free edge of scarf

joints. Eur J Mech A-Solid 18: 443–463. [https://doi.org/10.1016/S0997-7538\(99\)00118-7](https://doi.org/10.1016/S0997-7538(99)00118-7)

45. Harvey JF (1974) *Theory and Design of Modern Pressure Vessels*, Van Nostrand Reinhold.

46. Auger F, Gonc, alves P, Lemoine O, et al. (1996) *Time-frequency toolbox: For use with Matlab.* Available from: <https://tftb.nongnu.org/>

47. Piedboeuf MC, Gauvin R, Thomas M (1998) *Damping behaviour of shape memory alloys: strain amplitude, frequency and temperature effects. J Sound Vib* 214: 895–901. <https://doi.org/10.1006/jsvi.1998.1578>

Appendix

A. Damper at L/2 and deviation at L/2 (study case 1)

Figure 15a,b provides cable transverse displacements at L/4 and L/16, while the force and the damper were placed at L/2.

For both positions L/4 and L/16, a good agreement is observed between numerical and experimental results. In [41], the authors distinguished the local effect of the damper (due to a punctual increase of the stiffness near the device) from the global effect (function of the distance from the antinodes of the considered modes). These results validate how the cable and the damper were connected in the Finite Element model.

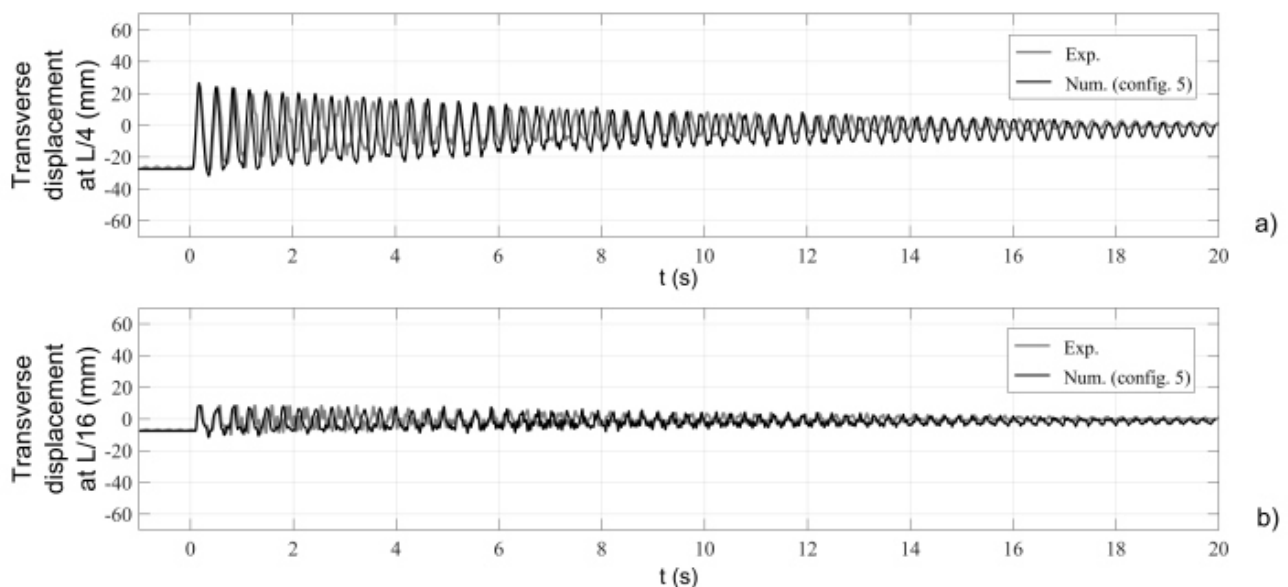


Figure 15. Transverse displacement of the cable equipped with a damper (configuration 5) placed at L/2: (a) sensor at L/4, (b) sensor at L/16.

B. Damper at L/4 and deviation at L/2 (study case 2)

Figure 16a–c provides the cable transverse displacement at L/2, L/4 and L/16, while the damper was moved to L/4.

It should be noted that the sensor placed at L/2 was an accelerometer for this study case. The transverse displacement signal obtained experimentally was integrated from the transverse acceleration and information was lost during numerical integrations. It explains why the initial deviation before the cable release is not observable (see Figure 16a). This point is not a major problem since the initial deviation is similar to those obtained in study case 1 (the deviating force was placed at the same position and the initial deviation was associated with the deactivated stage of the damper). A very good agreement is observed between numerical and experimental results in both configurations, although configuration 4

overestimated the damping even more than configuration 5. One can observe a lower damping compared to the reference study case. Indeed, the damping device was no longer placed at the antinode of the first and main involved vibration mode in study case 2.

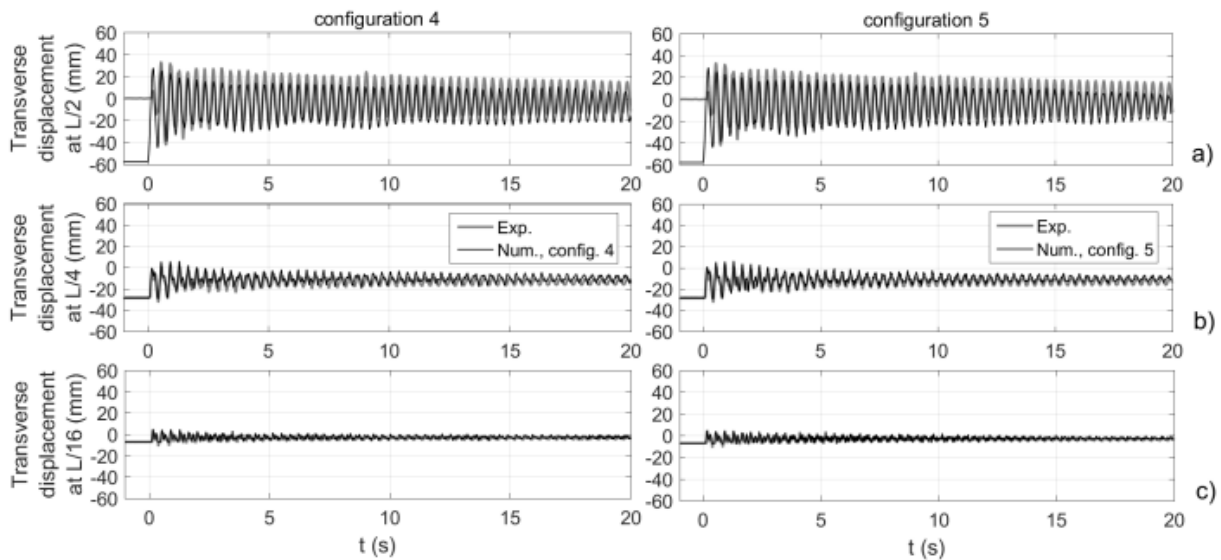


Figure 16. Transverse displacement of the cable equipped with a damper placed at $L/4$: sensor placed (a) at $L/2$, (b) at $L/4$, (c) at $L/16$.

C. Damper at $L/2$ and deviation at $L/4$ (study case 3)

Figure 17a–c provides the cable transverse displacement at $L/2$, $L/4$ and $L/16$, while the force was moved to $L/4$ and the damper was placed at $L/2$. This study case is the least favorable with respect to the second vibration mode since the force was placed at its antinode and the damper was placed at its node. From Figure 17a–c, a strong damping was observed experimentally and numerically at $L/2$ where was placed the damper, while a low damping was observed at $L/4$ and $L/16$ where the second vibration mode had a higher contribution. This confirms that placing the device in the middle of the cable is not relevant regarding the even-numbered modes. For both configurations 4 and 5, a good agreement is observed regarding the transverse displacement amplitude and its mitigation. However, an offset can be observed regarding the initial amplitude at $L/2$ and $L/4$, whatever the configuration. This offset can be explained by a small error on the pre-strain value of the “numerical wire” due to the potential accumulation of residual strain in the wires during the test campaign or a small error on the cable bending stiffness. Once again, a better damping prediction was obtained in configuration 5.

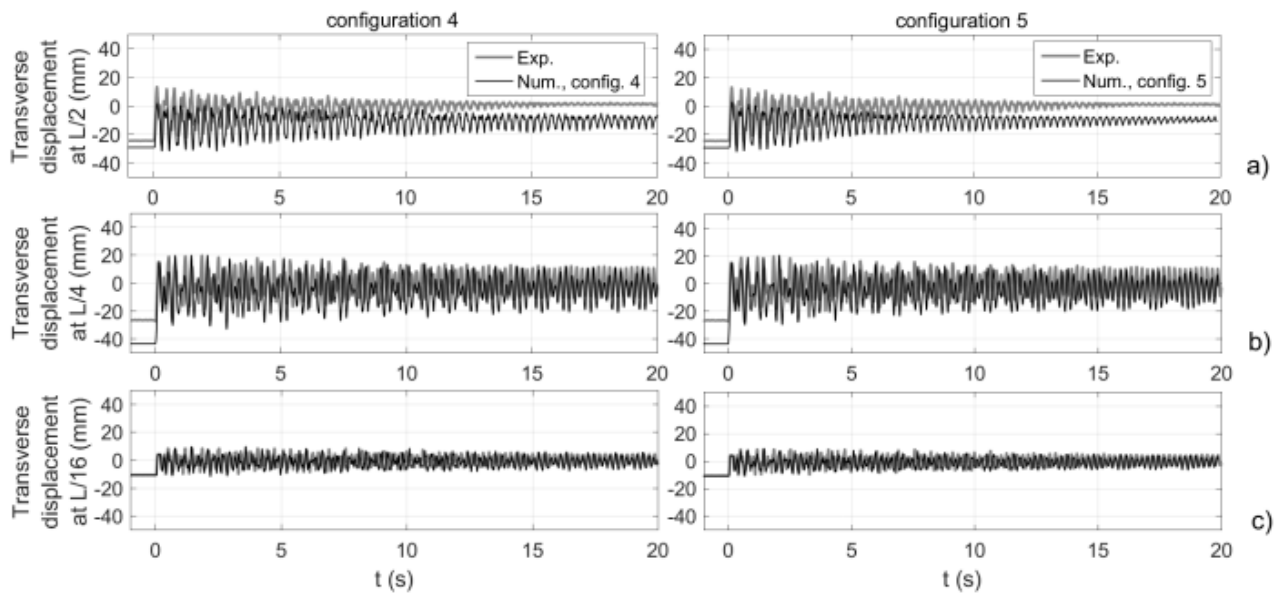


Figure 17. Transverse displacement of the cable equipped with a damper placed at $L/2$: sensor placed (a) at $L/2$, (b) at $L/4$, (c) at $L/16$.

Contribution to Study the effect of (Reuss, LRVE, Tamura) models on the axial and shear stress of sandwich FGM plate (Ti- 6Al- 4V/ZrO₂) subjected on linear and nonlinear thermal loads

Rebai Billel*

Faculty of Sciences & Technology, Civil Engineering Department, University of Abbes Laghrour
Khenchela, Algeria

ABSTRACT

The principal goal of the current work is to study the impact of three homogenization models (Reuss, LRVE, Tamura) on the axial and shear stress of sandwich functionally graded plate materials subjected on linear and nonlinear thermal loads with static and elastic behavior and it is simply supported using an integral higher shear deformation theory (HSDT). The governing partial differential equations are solved in the spatial coordinate by Navier solution. Those Numerous micromechanical models have been examined to attain the effective material properties of the two-phase FGM plate. The numerical results are compared with those given by other model existing in the literature to confirm the accuracy of the (HSDT). The present results are in good agreement with all models studied of homogenization for all values of the material index and all geometry configurations of the FG-sandwich plates.

Keywords: micromechanics; sandwich FG plate; stress; thermal loads

1. Introduction

Functionally graded materials (FGM) are an advanced composite material class whose vary gradually and continuously in the composition of microstructure constituents through the dimension of the material [1–3]. The behavior composition of FGM reduce the structural weight with increasing its coefficient modulus of stiffness and strength [4–8]. The properties of all constituents can be employed, for example, the toughness of a metal can be mated with the refractoriness of a ceramic, without any compromise in the toughness of the metal side or the refractoriness of the ceramic side [9–14]. The simple rule of mixture (Voigt law) is used to obtain the effective micromechanics material properties in the commencement of research papers. But to assess the effect of the micromechanical models on the structural responses of FG plates several micromechanical models of FGMs have been studied in [14–16]. Gasik has studied different micromechanical models to obtain the effective material properties of FGMs with power-law, Sigmoid, and exponential function distributions of volume fraction across the thickness of the static, buckling, free and forced vibration analyses for simply-supported FG plates resting on an elastic foundation [17]. Akbarzadeh et al. [18] have investigated about the influences of different forms of micromechanical models on FGM pressurized hollow cylinders. They have used the numerical results via finite element method (FEM) analyses for detailed and homogenized models of functionally graded (FG) carbon nanotube reinforced composite (CNTRC) beams. The effect of the imposed temperature field on the response of the FGM plate composed of Metal and Ceramic with the Mori–Tanaka micromechanical method is discussed [19,20].

Shen et al. [21] have studied the small and large amplitude frequency of vibrations are presented for a functionally graded rectangular plate resting on a two-parameter elastic foundation with two kinds of micromechanics models, namely, Voigt model and Mori–Tanaka model. The comparison studies reveal that the difference between these two models is much less compared to the difference caused by different solution methodologies and plate theories. In literature there is no available work

treating the impact of the homogenization models on the sandwich FGM plate. In this paper we have studied the impact of (Reuss, LRVE, Tamura) homogenization or micromechanical models on the axial and shear stress of sandwich functionally graded materials plate subjected to linear and nonlinear thermal loads. The static and elastic behavior of the simply supported is considered. Using an integral higher shear deformation theory (HSDT), the governing partial differential equations are solved in the Cartesian coordinate via Navier solution method. Those Numerous micromechanical models have been examined to attain the effective material properties of the two-phase FGM plate (Metal and ceramic). The numerical results are compared with those given by other model existing in the literature to confirm the accuracy of the (HSDT). The present results are in good agreement with all models studied of homogenization for all values of the material index and all geometry configurations of the FG-sandwich plates.

2. Materials and methods

The geometry domain is assumed as a uniform rectangular plate with thickness “h”, length “a”, and width “b” as shown in Figure 1. The plate has three layers. The FG-face sheets are made by two materials metal and ceramic.

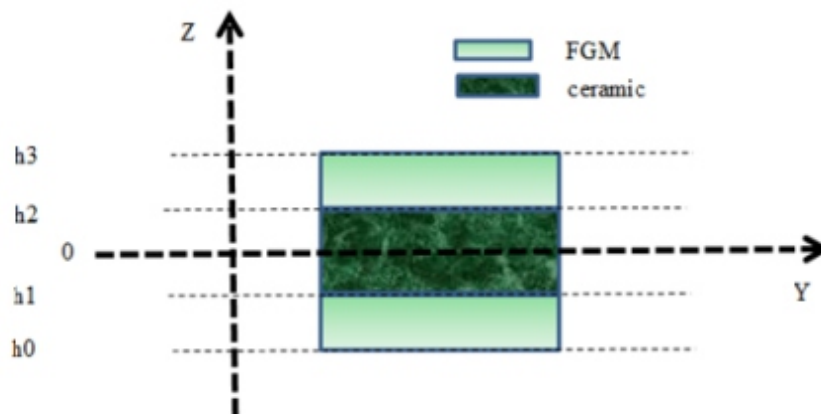


Figure 1. The geometry domain of functionally graded materials plate.

1.1. Materials characteristics

The mechanical and thermal properties of Metal (Titanium) are Young modulus $E(z)$ is 66.2 GPa, thermal expansion coefficients α is $10.3 (10^{-6}/K)$. The mechanical and thermal properties of Ceramic (Zirconia) are Young modulus $E(z)$ is 117 GPa, thermal expansion coefficients α is $7.11 (10^{-6}/K)$. The Poisson coefficient is supposed the same in the metal and the ceramic (ν is $1/3$). In the following.

Several types of geometries configurations are examined depending the thickness of each layer as shown in Table 1.

Table 1. Configurations of the plate.

Configurations of the plate	Geometries with Layers thickness
(1-0-1)	
(1-1-1)	
(1-2-1)	
(2-1-2)	
(2-2-1)	

The volumes fraction of the FG- faces sheet are assumed varies as following functions (Eq 1).

$$\begin{aligned}
 V^{(1)} &= \left(\frac{z - h_0}{h_1 - h_0} \right)^k & z \in [h_0, h_1] \\
 V^{(2)} &= 1 & z \in [h_1, h_2] \\
 V^{(3)} &= \left(\frac{z - h_3}{h_2 - h_3} \right)^k & z \in [h_2, h_3]
 \end{aligned} \tag{1}$$

Where K is the material index.

A number of micromechanics models have been proposed for the determination of effective properties of FGMs. K is the material index.

(1) Voigt model

The Voigt model is relatively simple; this model is frequently used in most FGM analyses estimates properties of FGMs as:

$$P(T, z) = P_c(T, z)V(z) + P_m(T, z)(1 - V(z)) \quad (2)$$

(2) Reuss model

Reuss assumed the stress uniformity through the material and obtained the effective properties as:

$$P(T, z) = \frac{P_c(T, z)P_m(T, z)}{P_c(T, z)(1 - V(z)) + P_m(T, z)V(z)} \quad (3)$$

(3) Tamura model

The Tamura model uses actually a linear rule of mixtures, introducing one empirical fitting parameter known as “stress-to-strain transfer”. For $q = 0$ correspond to Reuss rule and with $q = \pm \infty$ to the Voigt rule, being invariant to the consideration of with phase is matrix and which is particulate. The effective property is found as:

$$P(T, z) = \frac{(1 - V(z))P_m(T, z)(q - P_c(T, z)) + V(z)P_c(T, z)(q - P_m(T, z))}{(1 - V(z))(q - P_c(T, z)) + V(z)P_c(T, z)(q - P_m(T, z))} \text{ with} \quad (4)$$

$$q = \frac{\sigma_1 - \sigma_2}{\varepsilon_1 - \varepsilon_2}$$

(4) Description by a representative volume element (LRVE)

The LRVE is developed based on the assumption that the microstructure of the heterogeneous material is known. The input for the LRVE for the deterministic micromechanical framework is usually volume average or ensemble average of the descriptors of the microstructures. The effective property is expressed as follows by the LRVE method:

$$P(T, z) = P_m(T, z) \left(1 + \frac{V(z)}{\frac{1}{1 - \frac{P_m(T, z)}{P_c(T, z)}} - \sqrt[3]{V(z)}} \right) \quad (5)$$

2.2. Displacement base field

Based on the same assumptions of the conventional HSST (with five variables or more). The

displacement field of the proposed HSDT is only with four unknown variables and can be written in a simpler form as:

$$\begin{cases} u(x, y, z) = u_0(x, y) - z \frac{\partial w_0}{\partial x} + k_1 f(z) \int \theta(x, y) dx \\ v(x, y, z) = v_0(x, y) - z \frac{\partial w_0}{\partial y} + k_2 f(z) \int \theta(x, y) dy \\ w(x, y, z) = w_0(x, y) \end{cases} \quad (6)$$

Where $u_0(x, y)$, $v_0(x, y)$, $w_0(x, y)$ and $\theta(x, y)$ are the four-unknown displacement functions of middle surface of the FG-sandwich plate. $f(z)$ is the warping function and (k_1 and k_2) are constants.

In the current research work the proposed combined (exponential/hyperbolic) warping function ensures the nullity condition of the free surfaces of the FG-sandwich plate (zero transverse shear stresses at top and the Bottom of the FG-sandwich plate). The present exponential/hyperbolic warping function $f(z)$ is expressed as:

$$f(z) = \left[\ln \left(\pi \exp \left(\frac{1}{20} \right) \right) - \left((0.1407)^{(5/6)} \right) \cosh(\pi z) \right] z \quad (7)$$

The stresses/strains linear relation of the PFG-sandwich plate can be expressed as:

$$\begin{Bmatrix} \sigma_x \\ \sigma_y \\ \tau_{xy} \\ \tau_{yz} \\ \tau_{xz} \end{Bmatrix}^{(n)} = \begin{bmatrix} C_{11} & C_{12} & 0 & 0 & 0 \\ C_{12} & C_{22} & 0 & 0 & 0 \\ 0 & 0 & C_{66} & 0 & 0 \\ 0 & 0 & 0 & C_{44} & 0 \\ 0 & 0 & 0 & 0 & C_{55} \end{bmatrix}^{(n)} \begin{Bmatrix} \varepsilon_x - \alpha T \\ \varepsilon_y - \alpha T \\ \gamma_{xy} \\ \gamma_{yz} \\ \gamma_{xz} \end{Bmatrix}^{(n)} \quad (8)$$

Where

$$\begin{cases} C_{11}^{(n)} = C_{22}^{(n)} = \frac{E^{(n)}(z)}{1 - (\nu^{(n)})^2} \\ C_{12}^{(n)} = \nu^{(n)} C_{11}^{(n)} \\ C_{44}^{(n)} = C_{55}^{(n)} = C_{66}^{(n)} = \frac{E^{(n)}(z)}{2(1 + \nu^{(n)})} \end{cases} \quad (9)$$

The variation of the temperature field across the thickness is assumed to be:

$$T(x, y, z) = T_1(x, y) + \frac{z}{h} T_2(x, y) + \frac{\Psi(z)}{h} T_3(x, y) \quad (10)$$

Where

$$\Psi(z) = \frac{h}{\pi} \sin \left(\frac{\pi z}{h} \right) \quad (11)$$

The principle of virtual works of the considered PFG-sandwich plates is expressed as $gU + gV = 0$ where gU is the variation of strain energy; and gV is the variation of the virtual work done by external load applied to the plate. The governing equations can be obtained as follows:

$$\left\{ \begin{array}{l} \delta u_0 : \frac{\partial N_x}{\partial x} + \frac{\partial N_{xy}}{\partial y} = 0 \\ \delta v_0 : \frac{\partial N_{xy}}{\partial x} + \frac{\partial N_y}{\partial y} = 0 \\ \delta w_0 : \frac{\partial^2 M_x^b}{\partial x^2} + 2 \frac{\partial^2 M_{xy}^b}{\partial x \partial y} + \frac{\partial^2 M_y^b}{\partial y^2} = 0 \\ \delta \theta : -k_1 M_x^s - k_2 M_y^s - (k_1 A' + k_2 B') \frac{\partial^2 M_{xy}^s}{\partial x \partial y} + k_1 A' \frac{\partial S_x^s}{\partial x} + k_2 B' \frac{\partial S_y^s}{\partial y} = 0 \end{array} \right. \quad (12)$$

Based on the Navier method, the following expansions of displacements are

$$\left\{ \begin{array}{l} u_0 \\ v_0 \\ w_0 \\ \theta \end{array} \right\} = \left\{ \begin{array}{l} U \cos(\alpha x) \sin(\beta y) \\ V \sin(\alpha x) \cos(\beta y) \\ W \sin(\alpha x) \sin(\beta y) \\ X \sin(\alpha x) \sin(\beta y) \end{array} \right\} \quad (13)$$

where (U, V, W, X) are unknown functions to be determined and $\alpha = \pi / a$ and $\beta = \pi / b$.

In the present work, the transverse temperature loads T1, T2, and T3 in double sinus series form as:

$$\left\{ \begin{array}{l} T_1 \\ T_2 \\ T_3 \end{array} \right\} = \left\{ \begin{array}{l} \bar{T}_1 \\ \bar{T}_2 \\ \bar{T}_3 \end{array} \right\} \sin(\alpha x) \sin(\beta y) \quad (14)$$

The closed-form solution can be written as following matrix form:

$$\left[\begin{array}{cccc} S_{11} & S_{12} & S_{13} & S_{14} \\ S_{12} & S_{22} & S_{23} & S_{24} \\ S_{13} & S_{23} & S_{33} & S_{34} \\ S_{14} & S_{24} & S_{34} & S_{44} \end{array} \right] \left\{ \begin{array}{l} U \\ V \\ W \\ X \end{array} \right\} = \left\{ \begin{array}{l} P_1 \\ P_2 \\ P_3 \\ P_4 \end{array} \right\} \quad (15)$$

Where

$$\left\{ \begin{array}{l} S_{11} = -(A_{11} \alpha^2 + A_{66} \beta^2) \\ S_{12} = -\alpha \beta (A_{12} + A_{66}) \\ S_{13} = \alpha (B_{11} \alpha^2 + B_{12} \beta^2 + 2B_{66} \beta^2) \\ S_{14} = \alpha (k_1 B_{11}^s + k_2 B_{12}^s - (k_1 A' + k_2 B') B_{66}^s \beta^2) \\ S_{22} = -(A_{66} \alpha^2 + A_{22} \beta^2) \\ S_{23} = \beta (B_{22} \beta^2 + B_{12} \alpha^2 + 2B_{66} \alpha^2) \end{array} \right. \quad (16)$$

$$\begin{cases} S_{24} = \beta(k_2 B_{22}^s + k_1 B_{12}^s - (k_1 A^s + k_2 B^s) B_{66}^s \alpha^2) \\ S_{33} = -(D_{11} \alpha^4 + 2(D_{12} + 2D_{66}) \alpha^2 \beta^2 + D_{22} \beta^4) \\ S_{34} = -k_1 (D_{11}^s \alpha^2 + D_{12}^s \beta^2) + 2(k_1 A^s + k_2 B^s) D_{66}^s \alpha^2 \beta^2 - k_2 (D_{22}^s \beta^2 + D_{12}^s \alpha^2) \\ S_{44} = -k_1 (H_{11}^s k_1 + H_{12}^s k_2) - (k_1 A^s + k_2 B^s)^2 H_{66}^s \alpha^2 \beta^2 - k_2 (H_{12}^s k_1 + H_{22}^s k_2) - (k_1 A^s)^2 A_{33}^s \alpha^2 - (k_2 B^s)^2 A_{44}^s \beta^2 \end{cases}$$

And

$$\begin{cases} P_1 = \alpha(A^T T_1 + B^T T_2 + {}^a B^T T_3) \\ P_2 = \beta(A^T T_1 + B^T T_2 + {}^a B^T T_3) \\ P_3 = -h(\alpha^2 + \beta^2)(B^T T_1 + D^T T_2 + {}^a D^T T_3) \\ P_4 = -h(\alpha^2 + \beta^2)({}^s B^T T_1 + {}^s D^T T_2 + {}^s F^T T_3) \end{cases} \tag{17}$$

Where and (LT, aLT, RT) are coefficients calculated by integral summation formulations, in which $\bar{z} = z/h, \bar{f}(z) = f(z)/h$ and $\bar{\psi}(z) = \psi(z)/h$.

3. Results and discussion

In the following three sections, the results have been presented.

3.1. Comparisons and validation

A comparison has been done to verify the accuracy of the present theory of different models of homogenization (Reuss, Tamura and LRVE). Results are compared with the mixture model (Voigt) using by Zankour and Algamidi [22].

The dimensionless transverse and normal stress are expressed as:

$$\begin{cases} \bar{\sigma}_x = \frac{h^2}{\alpha_0 \bar{T}_2 E_0 a^2} \sigma_x \left(\frac{a}{2}, \frac{b}{2}, \frac{h}{2} \right) \\ \bar{\tau}_{xz} = \frac{10h}{\alpha_0 \bar{T}_2 E_0 a} \tau_{xz} \left(0, \frac{b}{2}, 0 \right) \end{cases} \tag{18}$$

with $E_0 = 1GPa$ and $\alpha_0 = 10^6 K$.

Table 2. Axial stresses $\bar{\sigma}_x$ of the FG square plates ($T_3 = 0$).

k	Theory		$\bar{\sigma}_x$				
			1-0-1	1-1-1	1-2-1	2-1-2	2-2-1
0	Zankour	Voigt	-2.079675000	-2.079675000	-2.079675000	-2.079675000	-2.079675000
		Present	-2.079675000	-2.079675000	-2.079675000	-2.079675000	-2.079675000
		LRVE	-2.079675000	-2.079675000	-2.079675000	-2.079675000	-2.079675000
		Tamura	-2.079675000	-2.079675000	-2.079675000	-2.079675000	-2.079675000
1	Zenkour	Voigt	-1.993962994	-2.144483622	-2.262070783	-2.071720141	-2.276270538
		Present	-2.054001279	-2.206426851	-2.319985581	-2.133961897	-2.328859434
		LRVE	-2.019721781	-2.170723580	-2.286705796	-2.098127768	-2.298783479
		Tamura	-2.054001279	-2.206426851	-2.319985581	-2.133961897	-2.328859434

3	Zenkour	Voigt	-1.764722947	-1.912070024	-2.065545648	-1.830280890	-2.099358095
	Present	Reuss	-1.780352582	-1.937106476	-2.093543390	-1.851668884	-2.122979641
		LRVE	-1.772412913	-1.923584710	-2.078438949	-1.840257943	-2.110349605
		Tamura	-1.780352582	-1.937106476	-2.093543390	-1.851668884	-2.122979641
5	Zenkour	Voigt	-1.726018586	-1.851951252	-2.008943548	-1.775782946	-2.052753400
	Present	Reuss	-1.731998461	-1.865654772	-2.025948107	-1.786255940	-2.066835810
		LRVE	-1.729130531	-1.858346729	-2.016889735	-1.780777417	-2.059428200
		Tamura	-1.731998461	-1.865654772	-2.025948107	-1.786255940	-2.066835810

Table 2 presents the variation of dimensionless axial stress “ σ_x ” of the square FG-sandwich plate subjected to linearly thermal load “ $T_3 = 0$ ” versus volumes fractions (material index “ k ”) for different values of layer thickness ratio. It is remarkable that there is a proportional relationship between the index “ k ” the dimensionless normal stress “ σ_x ”

Table 3. Shear stresses $\bar{\tau}_{xz}$ of the FGM square plates ($T_3 = -100$).

k	Theory		$\bar{\tau}_{xz}$				
			1-0-1	1-1-1	1-2-1	2-1-2	2-2-1
0	Zenkour	Voigt	0.4146850492	0.4146850448	0.4146850391	0.4146850437	0.4146850439
	Present	Reuss	0.4146850492	0.4146850448	0.4146850391	0.4146850437	0.4146850439
		LRVE	0.4146850492	0.4146850448	0.4146850391	0.4146850437	0.4146850439
		Tamura	0.4146850492	0.4146850448	0.4146850391	0.4146850437	0.4146850439
1	Zenkour	Voigt	0.5088666494	0.5057769569	0.5120235930	0.5028076163	0.5078946003
	Present	Reuss	0.5136021296	0.4984428129	0.4996166330	0.4989271190	0.4972491537
		LRVE	0.5087063178	0.5006052702	0.5045310781	0.4991788650	0.4946850439
		Tamura	0.5136021296	0.4984428129	0.4996166330	0.4989271190	0.4972491537
3	Zenkour	Voigt	0.5103204312	0.5033093833	0.5165886526	0.4976909215	0.5100386919
	Present	Reuss	0.5238780098	0.5054862362	0.5169250930	0.5015862328	0.5102636411
		LRVE	0.5156350522	0.5037663327	0.5159615534	0.4988965994	0.5012769094
		Tamura	0.5238780098	0.5054862362	0.5169250930	0.5015862328	0.5102636411
5	Zenkour	Voigt	0.5212843911	0.4908722755	0.5036863726	0.4852538506	0.5661515630
	Present	Reuss	0.5357072550	0.4919895199	0.5166537262	0.4878864038	0.5084226158
		LRVE	0.5281264494	0.4913047274	0.5153580228	0.4862334163	0.5071304901
		Tamura	0.5357072550	0.4919895199	0.5166537262	0.4878864038	0.5084226158

The Table 3 presents the variation of the dimensionless shear stress “ τ_{xz} ” of the square FG sandwich plate subjected to nonlinearly thermal load “ $T_3 = -100$ ” versus volumes fractions (material index “ k ”) for different values of layer thickness ratio. From the Table 3 the shear stress “ τ_{xz} ” and the index k have direct relation. We can see from the Tables 2 and 3 that the present results are in good agreement with all models studied of homogenization (Voigt Zenkour et al. [22], Reuss, LRVE and Tamura) for all values of the material index “ k ” and all configurations of the FG-sandwich plate (1-0-1, 1-1-1, 1-2-1, 2-1-2 and 2-2-1).

3.2. Parametric study

In this section, the parametric studies are presented in the explicit graphs form. Figure 2 plots the

variation of the axial stress “ σ_x ” across the total thickness “ h ” of FG-sandwich plate ($k=1$) under linear thermal loads “ $T_3 = 0$ ” with different micromechanical models. From the plotted graphs, it is clear that the compressive stresses are obtained at the top of the plate. We can see that the present results are in good agreement with different models Voigt, Reuss, LRVE and Tamura for configurations of the FG-sandwich plate (1-0-1, 1-2-1 and 2-2-1) and the material index $k=1$ (Figure 2a-c).

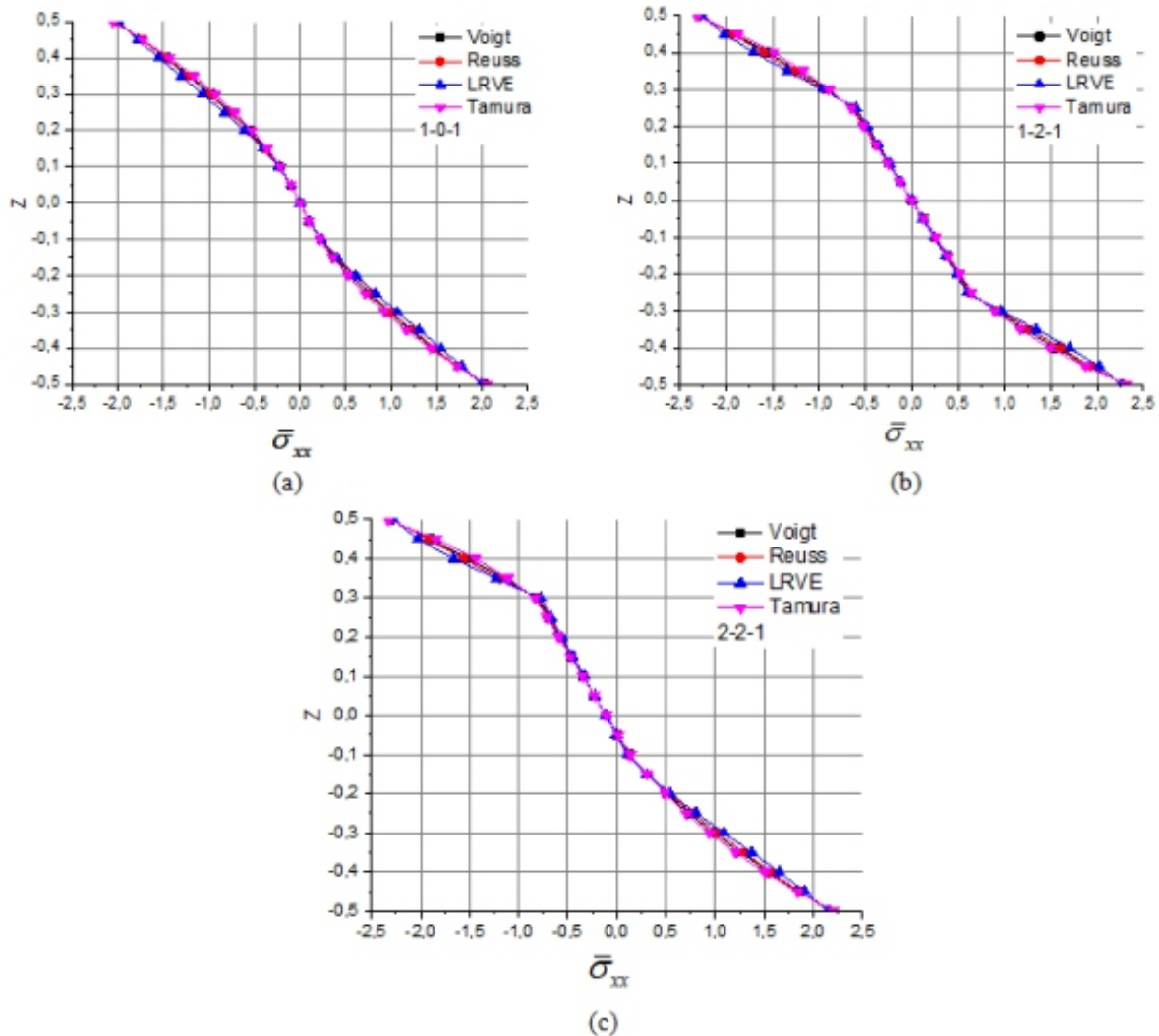


Figure 2. Effect of different micromechanical models on the axial stress $\bar{\sigma}_{xx}$ of FG-sandwich.

Figure 3 illustrates the variation of the “ τ_{xz} ” through the total thickness of the 1-0-1, 1-2-1 and 2-2-1 FG-sandwich plate under linear thermal loads “ $T_3 = 0$ ”. It is noted that the shear stress “ τ_{xz} ” is parabolically varied through the total thickness of the FG-sandwich plate. We can see that the present results are in good agreement with different models Voigt, Reuss, LRVE and Tamura for configurations of the FG-sandwich plate (1-0-1, 1-2-1 and 2-2-1) and the material index $k=1$ (Figure 3a-c).

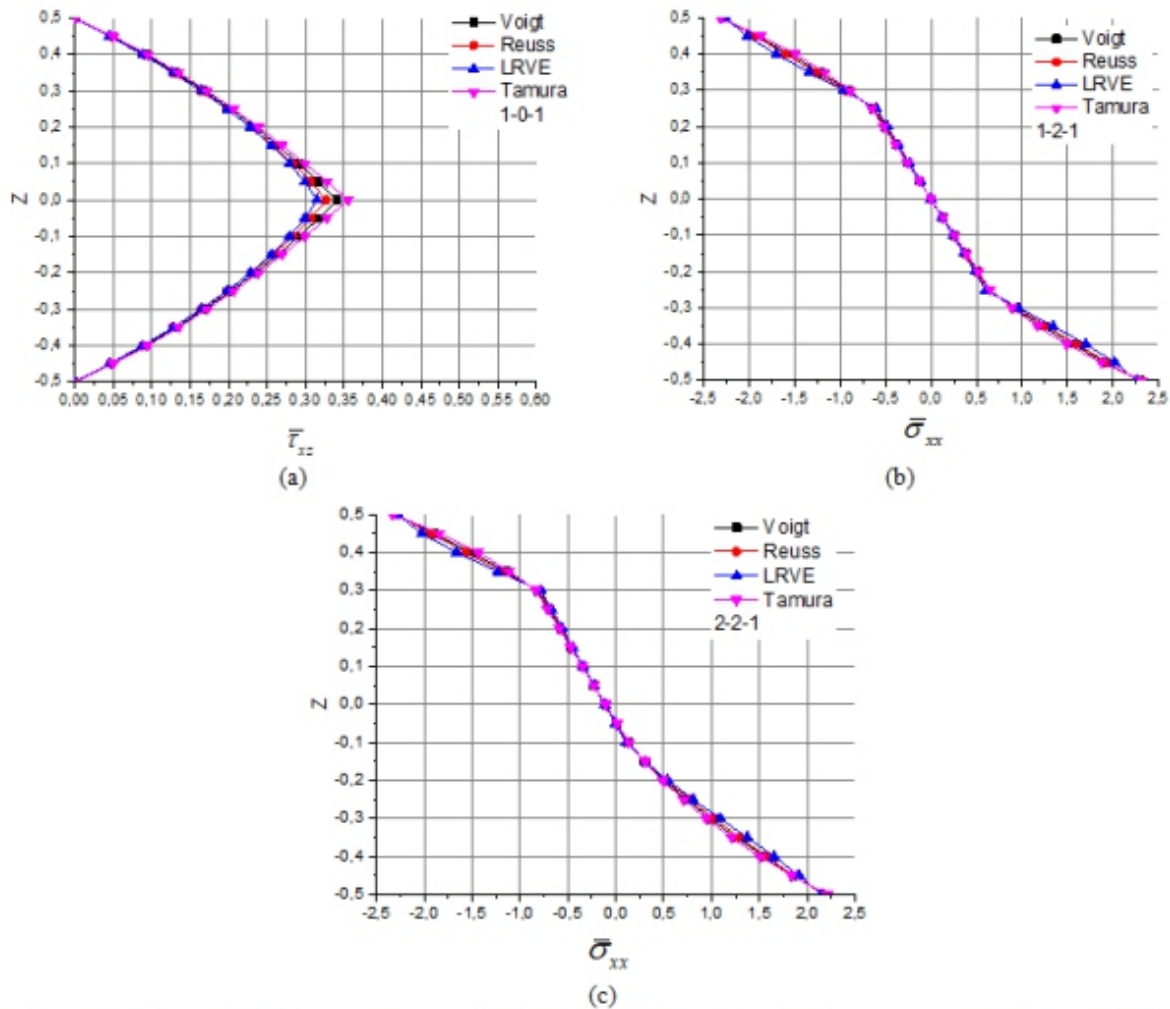


Figure 3. Effect of different micromechanical models on the axial stress $\bar{\sigma}_{xx}$ of FG-sandwich.

3.3. Effect of the thermal loads on the normal and shear stress

In the present section three types of the temperature distribution across the thickness are considered. The first one, the temperature is linearly distributed through the thickness $T = zT_2$, in the second type the temperatures vary nonlinearly across h ($T = zT_2 + \psi(z)T_3$) and the third type is reserved for a combination of linear and nonlinear distributions $T(z) = T_1 + (z/h)T_2 + (\psi(z)/h)T_3$

Figure 4a shows the distributions of the axial stress “ σ_x ” through the total thickness of the simply supported 2-2-1 FG-sandwich plate for various values of the thermal load ($T_1=100$), $T_2=100$ and $T_3=100$ with ($k=1$). From the plotted curves, it can be observed that the axial stress “ σ_x ” is influenced by the values of the thermal load.

Figure 4b plot the variation of the shear stress “ π_{xz} ” through the thickness h of the 2-2-1 square FG-sandwich plate ($k=1$). For different values of the thermal load ($T_1=100$), $T_2=100$ and $T_3=100$. It can be noted from the graphs that the shear stress “ π_{xz} ” has a parabolic variation through the thickness. The maximal values of the shear stress “ π_{xz} ” are obtained at the mid-plane axis “ $z=0$ ”. And it is clearly influenced by the values of the thermal load.

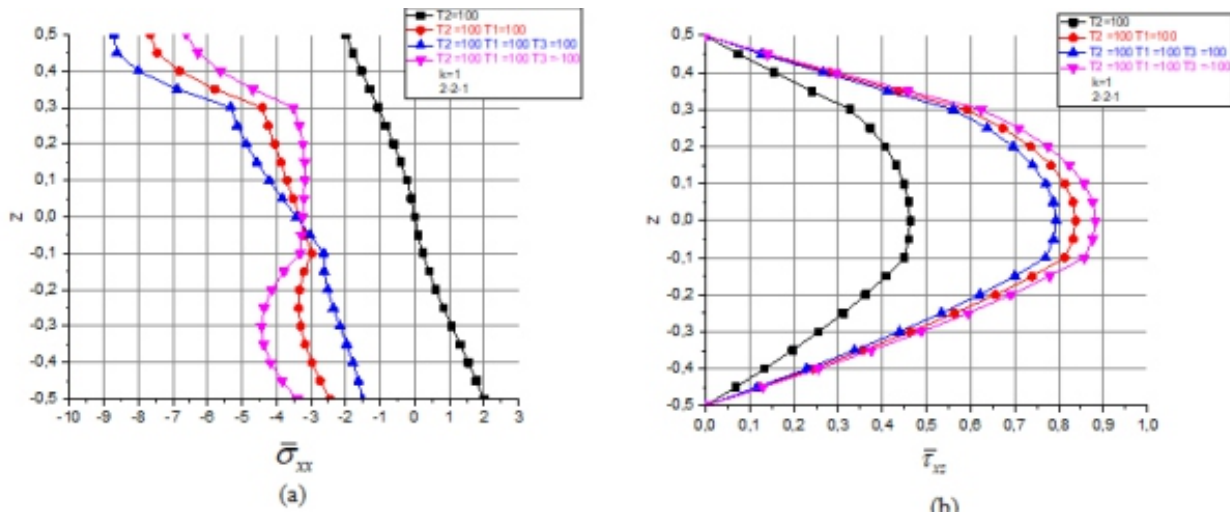


Figure 4. Effect of the thermal load T_1 , T_2 and T_3 on the axial and transverse stress (σ_{xx} , τ_{xz}) of the (2-2-1) FG-sandwich plate ($k=1$) for Voigt model.

4. Conclusions

In this investigation, the impact of (Reuss, LRVE, Tamura) homogenization or micromechanical models on the axial and shear stress of sandwich functionally graded materials plate subjected to linear and nonlinear thermal loads have studied. The static and elastic behavior of the simply supported is considered. Using an integral higher shear deformation theory (HSST), the governing partial differential equations are solved in the Cartesian coordinate via Navier solution method.

Those Numerous micromechanical models have been examined to attain the effective material properties of the two-phase FGM plate (Metal and ceramic). The numerical results are compared with those given by other model existing in the literature to confirm the accuracy of the (HSST). The present results are in good agreement with all models studied of homogenization for all values of the material index and all geometry configurations of the FG-sandwich plates.

Acknowledgments

The authors gratefully acknowledge the support provided by University of Sidi Bel Abbes, Algeria while the preparation of the doctorate thesis.

Conflict of interest

The authors declare no conflict of interest.

References

1. Venâncio MAS, Loja A (2016) A study on the behavior of laminated and sandwich composite plates using a layerwise theory. *AIMS Mater Sci* 3: 1587–1614. <https://doi.org/10.3934/matersci.2016.4.1587>
2. Salleh Z, Islam MM, Epaarachchi JA, et al. (2016) Mechanical properties of sandwich composite made of syntactic foam core and GFRP skins. *AIMS Mater Sci* 3: 1704–1727. <https://doi.org/10.3934/matersci.2016.4.1704>
3. Abood AM, Khazal H, Hassan AF (2022) On the determination of first-mode stress intensity factors and T-stress in a continuous functionally graded beam using digital image correlation method. *AIMS Mater Sci* 9: 56–70. <https://doi.org/10.3934/matersci.2022004>
4. Bash AM, Mnawe SE, Salah SA (2020) Numerical buckling analysis of carbon fibre-epoxy composite plates with different cutouts number by finite element method. *AIMS Mater Sci* 7: 46–59.

<https://doi.org/10.3934/matersci.2020.1.46>

5. Sánchez CA, Cardona-Maya Y, Morales AD, et al. (2021) Development and evaluation of polyvinyl alcohol films reinforced with carbon nanotubes and alumina for manufacturing hybrid metal matrix composites by the sandwich technique. *AIMS Mater Sci* 8: 149–165. <https://doi.org/10.3934/matersci.2021011>

6. Saberi S, Abdollahi A, Inam F (2021) Reliability analysis of bistable composite laminates. *AIMS Mater Sci* 8: 29–41. <https://doi.org/10.3934/matersci.2021003>

7. Ishchuk V, Kuzenko D, Sobolev V (2018) Piezoelectric and functional properties of materials with coexisting ferroelectric and antiferroelectric phases. *AIMS Mater Sci* 5: 711–741. <https://doi.org/10.3934/matersci.2018.4.711>

8. Kozhakhmetov Y, Skakov M, Wieleba W, et al. (2020) Evolution of intermetallic compounds in Ti-Al-Nb system by the action of mechanoactivation and spark plasma sintering. *AIMS Mater Sci* 7: 182–191.

9. Costa S, Souza MS, Braz-César MT, et al. (2021) Experimental and numerical study to minimize the residual stresses in welding of 6082-T6 aluminum alloy. *AIMS Mater Sci* 8: 271–282. <https://doi.org/10.3934/matersci.2021018>

10. Abdellah MY, Alharthi H, Hassan MK, et al. (2020) Effect of specimen size on natural vibration of open hole copper/glass-reinforced epoxy laminate composites. *AIMS Mater Sci* 7: 499–517. <https://doi.org/10.3934/matersci.2020.4.499>

11. Soyama H, Okura Y (2018) The use of various peening methods to improve the fatigue strength of titanium alloy Ti6Al4V manufactured by electron beam melting. *AIMS Mater Sci* 5: 1000-1015. <https://doi.org/10.3934/matersci.2018.5.1000>

12. Esquivel Merino MD, Van Der Voort P, Romero-Salguero F (2014) Designing advanced functional periodic mesoporous organosilicas for biomedical applications. *AIMS Mater Sci* 1: 70–86. <https://doi.org/10.3934/matersci.2014.1.70>

13. Nie G, Zhong Z (2010) Dynamic analysis of multi-directional functionally graded annular plates. *Appl Math Model* 34: 608–616. <https://doi.org/10.1016/j.apm.2009.06.009>

14. Tucker III, Charles L, Liang E (1999) Stiffness predictions for unidirectional short-fiber composites: Review and evaluation. *Compos Sci Technol* 59: 655–671. [https://doi.org/10.1016/S0266-3538\(98\)00120-1](https://doi.org/10.1016/S0266-3538(98)00120-1)

15. Kim JH, Paulino GH (2003) An accurate scheme for mixed-mode fracture analysis of functionally graded materials using the interaction integral and micromechanics models. *Int J Numer Meth Eng* 58: 1457–1497. <https://doi.org/10.1002/nme.819>

16. Zuiker JR (1995) Functionally graded materials: Choice of micromechanics model and limitations in property variation. *Comp Eng* 5: 807–819. [https://doi.org/10.1016/0961-9526\(95\)00031-H](https://doi.org/10.1016/0961-9526(95)00031-H)

17. Gasik MM (1998) Micromechanical modelling of functionally graded materials. *Comp Mater Sci* 13: 42-55. [https://doi.org/10.1016/S0927-0256\(98\)00044-5](https://doi.org/10.1016/S0927-0256(98)00044-5)

18. Akbarzadeh AH, Abedini A, Chen ZT (2015) Effect of micromechanical models on structural responses of functionally graded plates. *Compos Struct* 119: 598-609. <https://doi.org/10.1016/j.compstruct.2014.09.031>

19. Praveen GN, Reddy JN (1998) Nonlinear transient thermoelastic analysis of functionally graded ceramic-metal plates. *Int J Numer Meth Eng* 35: 4457–4476. [https://doi.org/10.1016/S0020-7179\(98\)00253-9](https://doi.org/10.1016/S0020-7179(98)00253-9)

20. Jin X, Wu LZ, Guo LC, et al. (2009) Prediction of the variation of elastic modulus of ZrO₂/NiCr functionally graded materials. *Compos Sci Technol* 69: 1587–1591. <https://doi.org/10.1016/j.compscitech.2009.02.032>

21. Shen HS, Wang ZX (2012) Assessment of Voigt and Mori-Tanaka models for vibration analysis of functionally graded plates. *Compos Struct* 94: 2197 – 2208.

<https://doi.org/10.1016/j.compstruct.2012.02.018>

1. Zenkour AM, Alghamdi NA (2008) Thermoelastic bending analysis of functionally graded sandwich plates. *J Mater Sci* 43: 2574–2589. <https://doi.org/10.1007/s10853-008-2476-6>

Fe-TiO₂/zeolite H-A photocatalyst for degradation of waste dye (methylene blue) under UV irradiation

Ririn Cahyanti, Sumari Sumari*, Fauziatul Fajarah, Muhammad Roy Asrori and Yana Fajar Prakasa

Department of Chemistry, Faculty of Mathematics and Natural Sciences Universitas Negeri Malang, Jl. Semarang No. 5, Malang, 65145, Indonesia

ABSTRACT

Industrial wastewater contains non-biodegradable dyes that are highly toxic to humans and aquatic life. As solution from photocatalytic degradation, TiO₂ is one of the effective photocatalysts for wastewater degradation, but it has low adsorption power. To overcome this deficiency, this study synthesized a new photocatalyst by Fe-TiO₂/zeolite H-A. The photocatalyst was successfully synthesized by the impregnation method and was systematically characterized by XRD, XRF, SEM, FT-IR and UV-Vis DRS. XRD diffractogram at $2\theta = 25.3^\circ$ showed anatase phase of the photocatalyst. SEM results showed a rough and soft surface with a size of 491.49 nm. FT-IR analysis obtained the zeolite-A characteristic band, vibration of Ti-O-Ti groups and the vibration of the Fe-O group. The bandwidth of the band gap was 3.16 eV. The photocatalytic efficiency of methylene blue degradation reached 89.58% yield with optimum conditions: irradiation time of 50 min, pH 9 and concentration of methylene blue about 20 mg/L. Fe-TiO₂/zeolite H-A as a new photocatalyst can be an alternative photocatalyst to purify methylene blue.

Keywords: dye degradation; photocatalyst; TiO₂; zeolite A; ferrous material.

1. Introduction

Textile dye come from the dyeing process, in which 10–15% of the used dyes cannot be recycled that still contain non-degradable dyes [1,2]. This is because the structure of the textile dye has one or more azo groups (R–N=N–R') and an aromatic ring which are mostly replaced by a sulfonate group and an aromatic structure [3]. Therefore, waste dye must be separated before it is discharged into rivers.

Several methods of removing waste dye, known as Advanced Oxidation Processes (AOPs), have been developed previously, including physical, biological and chemical process such as ultra-filtration, reverse osmosis, adsorption, coagulation, flocculation, ozonation, membrane filtration, biological treatment, chemical oxidation, electrochemistry and ion exchange [4,5]. However, the technique has several disadvantages, such as high cost, high chemical dosage and incompetent separation results, because it produces secondary wastes (by-products) such as sulfonates, phenols and many aromatic compounds which are more toxic than the initial wastewater contaminants [6]. The removal technique by photocatalytic degradation is reported as one of the appropriate and efficient techniques because the separation does not produce secondary contaminants [7,8]. The photocatalytic degradation process occurs when electron-hole pairs (e⁻ and h⁺) interact with industrial wastes to produce highly reactive hydroxyl radicals (OH•), which are capable of oxidizing various contaminants (organic compounds) into simpler molecules such as CO₂, H₂O and low levels of acidic minerals [6,9,10].

Titanium (IV) oxide (TiO₂) is one of the important semiconductor compounds for photocatalysts because of its high photocatalytic activity, low toxicity, good electrochemical properties, excellent

chemical stability, high redox potential, non-toxicity, inexpensiveness, erosion-resistance, abundance in nature, excellent stability over a wide pH range and environmental friendliness [11–14]. One TiO₂ phase is the anatase phase, which has bandgap energies of 3.2 eV [15,16]. Fe³⁺ ion sources are abundant in nature, cheap and easy to modify [17]. Fe³⁺ can reduce the recombination rate of electron and hole pairs [18] and establish energy levels inside the forbidden band gap [19]. Fe³⁺ cations have a smaller ionic radius of 0.55 Å compared to Ti⁴⁺ cations (0.61 Å) and are expected to be able to partially replace Ti⁴⁺ cations in the TiO₂ lattice structure. In the previous study, 1.75 wt% Fe-TiO₂ nanoparticles (anatase phase) were used for photocatalytic degradation of Methylene Blue at about 76% with conditions of 0.03 g/L catalyst dosage, 30 mg/L Methylene Blue (50 mL), UV lamp and 2 h reaction [20]. For increasing the degradation efficiency, zeolite can be an option, because it can delocalize excited electrons of TiO₂ and minimize e⁻/h⁺ recombination [21,22].

Zeolite Linde Type A (Zeolite LTA or zeolite A) is a synthetic zeolite with a very small pore diameter of 4 Å. Zeolite A is generally synthesized in the form of Na-zeolite with the formula Na₁₂[(AlO₂)₁₂(SiO₂)₁₂]-27H₂O and has a 3D pore structure consisting of a sodalite cage connected through a hollow double ring 4 (D4R) of [SiO₄]⁴⁻ and [AlO₄]⁵⁻. 3D structure: D4R, sodalite cage and α-cage [23]. The pore diameter of zeolite A is 0.23–0.42 nm, and it has a Si/Al molar ratio of 1 or close to 1 [23]. The property advantages of zeolite A were low molar ratio, low cost and high thermal stability. Therefore, zeolite A has great potential for separation, catalyst, adsorbent and wastewater treatment applications [24].

The research carried out synthesis of a photocatalyst by adding 2 materials at once: Fe³⁺ ions are impregnated into TiO₂ (anatase phase), known as Fe-TiO₂, and it is then impregnated into Zeolite H-A. The purpose of this research is to investigate and study the photocatalyst TiO₂ with the modification of the addition of Fe metal and zeolite H-A (called Fe-TiO₂/Zeolite H-A), by confirmation of the results of XRD, XRF, SEM, FT-IR and UV-DRS. In addition, another objective is to study the resulting photocatalytic activity. The photocatalyst activity of Fe-TiO₂/zeolite H-A was studied by using it for the degradation of methylene blue dye as a model pollutant. The photocatalytic performance of the synthesized photocatalyst was investigated under UV. The degradation was carried out with several parameters of contact time, pH and initial concentration of dye. In addition, until now, the development of photocatalysts with the addition of metal and a porous matrix (zeolite) as well as with TiO₂ is still rarely done.

2. Materials and methods

All reagents were used from analytical grade: Zeolite A (Merck), ammonium chloride (NH₄Cl 1 M), TiO₂ powder (Sigma Aldrich), Fe(NO₃)₃·9H₂O (Sigma Aldrich), ethanol (99%), demineralized water.

2.1. Preparation of zeolite A

Preparation of zeolite A was carried out using the ion exchange method. The process was assisted with an acid solution to obtain zeolite H-A. First, 5 g of zeolite Na-A was added, and then 50 mL of 1M NH₄Cl (1:10) was added with stirring using a shaker for 1 h at 150 rpm. After that, it was allowed to stand for 24 h. The mixture was filtered and neutralized with demineralized water to get a neutral pH. After that, the powder (residue) was dried in an oven at 115 °C for 2 h. The dried powder was calcined at 450 °C for 4 h. The calcined powder was zeolite H-A.

2.2. Synthesis of Fe-TiO₂/zeolite H-A

Synthesis of Fe-TiO₂/zeolite H-A photocatalyst was begun with the synthesis of Fe-TiO₂. The synthesis of Fe-TiO₂ was carried out with a modified method [25]. The synthesis method was the impregnation method. Fe(NO₃)₃·9H₂O powder was added to TiO₂ powder with 3% of TiO₂ weight in 100 mL of

demineralized water. The solution was stirred with a magnetic stirrer for 1 hour and then heated at a temperature of 80–90 °C. The residue was centrifuged and washed with demineralized water to pH 7. The obtained solid was then calcined at 400 °C for 2 h. Furthermore, the synthesis of Fe-TiO₂/zeolite H-A was carried out by a modified method [26]. 1.4 g of Fe-TiO₂ and 8 g of zeolite H-A were added into 10 mL of ethanol with stirring for 5 h. The mixture was filtered and neutralized. The residue was dried in an oven at 120 °C for 5 h. The solid was then calcined at 450 °C for 3 h.

2.3. Characterization for Fe-TiO₂/zeolite H-A

Crystal structure and phase were identified by Powder X-ray Diffraction (PXRD) (PANalytical E'xpert Pro). The crystalline element content was analyzed by X-ray Fluorescence (XRF) (brand: PANalytical; type: Minipal 4). Surface morphology analysis with various magnifications was performed by Scanning Electron Microscopy (SEM) (FEI Inspect-S50).

Functional group investigations were carried out by Fourier Transform Infra-Red (FT-IR) (Shimadzu IRPrestige 21). UV-Vis DRS (Analytik Jena Specord 200 plus) with a wavelength of 1100–200 nm was used to obtain band gap values, absorbance data. The obtained data was then processed using the Tauc plot equation with Origin software.

2.4. Photocatalytic degradation of Methylene Blue

The photocatalytic degradation process with UV irradiation was carried out in a cube-shaped box. All sides of the box covered in the dark (black light) box, and a 20-watt UV lamp was used. A stirrer was provided in the cube as a stirring device.

The degradation process was carried out as follows: 50 mg of Fe-TiO₂/zeolite H-A photocatalyst was put into a 50 mL Beaker glass. 10 mg/L of methylene blue was pipetted and diluted to 25 mL. Then, methylene blue was added to the photocatalyst. The mixture was stirred and irradiated with UV for 10–50 min with an interval of 10 min. After the irradiation process, the suspension was filtered to separate the supernatant and the precipitate. The supernatant obtained from each beaker was measured for absorbance with a UV-Vis spectrophotometer at a wavelength of 664 nm. The absorbance value obtained was then analyzed to get the linear regression equation, so the optimum time was obtained. The obtained data was then used in the formula for the percentage of degradation (Efficiency percentage) through the following equation.

$$\text{Efficiency percentage} = \frac{C_0 - C_t}{C_0} \times 100 \quad (1)$$

C₀ and C_t are the initial concentration of methylene blue and the concentration after the degradation process, respectively. The same procedure was repeated for pH (3, 5, 7, 9) and concentration of methylene blue (10, 20, 30, 40, 50 mg/L).

3. Results and discussions

3.1. Activation of zeolite A

In Zeolite H-A form, the acidic site in the zeolite framework transformed into a soft acid site (zeolite H-A), so it is more easily substituted by Ti⁴⁺ ions [27]. On the other hand, zeolite pretreatment or zeolite activation is to reduce impurities that cover the external surface and pores of the zeolite [28]. The modification of zeolite A to zeolite H-A was carried out using a solution of ammonium chloride (NH₄Cl) through the ion exchange method. The ion exchange process occurs between metal cations alkali metals (Na⁺, K⁺) and alkaline earths (Ca⁺, Ba²⁺) with ammonium cations (Nh₄⁺) from HH₄Cl, because metal cations have weak ion-dipole interactions with zeolites. The interactions support ion-exchange as shown in XRF results (Table 1) [29].

The XRD results are shown in Figure 1. Based on Figure 1, diffraction peaks of raw material appear at $2\theta = 10.24^\circ, 12.53^\circ, 16.19^\circ, 20.51^\circ, 21.76^\circ, 24.09^\circ, 26.22^\circ, 27.22^\circ, 30.95^\circ, 32.66^\circ, 33.49^\circ$ and 34.29° , which have the same crystal characteristics as zeolite A or zeolite Linde Type A (LTA) as the ICSD database No. 150097. This confirmed that the used raw material of zeolite was zeolite A. The XRD pattern of the zeolite H-A (Figure 1b) showed no peak shift and no significant diffractogram changes. This showed that the treatment of zeolite A to zeolite H-A did not change the crystal structure of the zeolite and the crystal phase compared to the initial zeolite. In addition, Figure 1 showed a fairly sharp diffraction peak, and this indicated the formation of zeolite H-A.

Based on the FT-IR results (Figure 1), the spectrum of zeolite LTA material appeared. The presence of the OH group of H₂O was indicated by the absorption band at 3365 cm^{-1} (bending vibration). The stretching vibration of the OH group of the silanol group (Si-OH) was shown in the absorption band of 1648 cm^{-1} . The absorption bands of the O-T-O group (T = Si, Al) were shown at 677 cm^{-1} (symmetrical) and 1000 cm^{-1} (asymmetrical). The absorption at 552 cm^{-1} indicated the external vibration of the double ring (D4R or D6R), which is a characteristic of the zeolite LTA structure [30]. The absorption band at 475 cm^{-1} indicated a bending vibration of the T-O group (T = Si, Al), and the absorption band at $400\text{--}370\text{ cm}^{-1}$ indicated the open pores of the zeolite framework material [31]. Furthermore, the FT-IR spectrum of the zeolite H-A showed a slight shift in the absorption wavenumber and intensity, so it did not have much different results from the initial zeolite A. The absorption band at $1400\text{--}400\text{ cm}^{-1}$ appeared in the zeolite H-A spectrum; the absorption band is a typical absorption band of LTA zeolite (zeolite A) [32]. This shows that the preparation process of zeolite A to zeolite H-A was successful without damaging the structure of the zeolite.

Supporting data confirmed by looking at changes in the level of elemental composition in the zeolite using XRF characterization. The XRF results are shown in Table 1. The data was used to calculate the Si/Al zeolite ratio. It was known that the ratio of Si/Al zeolite from zeolite A to H-A has changed from 2.03 to 1.98, but this zeolite has a ratio value of more than 1, which is different from the molar ratio of zeolite A in general. For example, zeolite A with a Si/Al molar ratio more than 1 was zeolite ZK-4 [30]. Thus, the used zeolite material is still a group of zeolite A. This study still uses the term zeolite A because the complexity of dimensions, structure and impurities are the same as zeolite A [32].

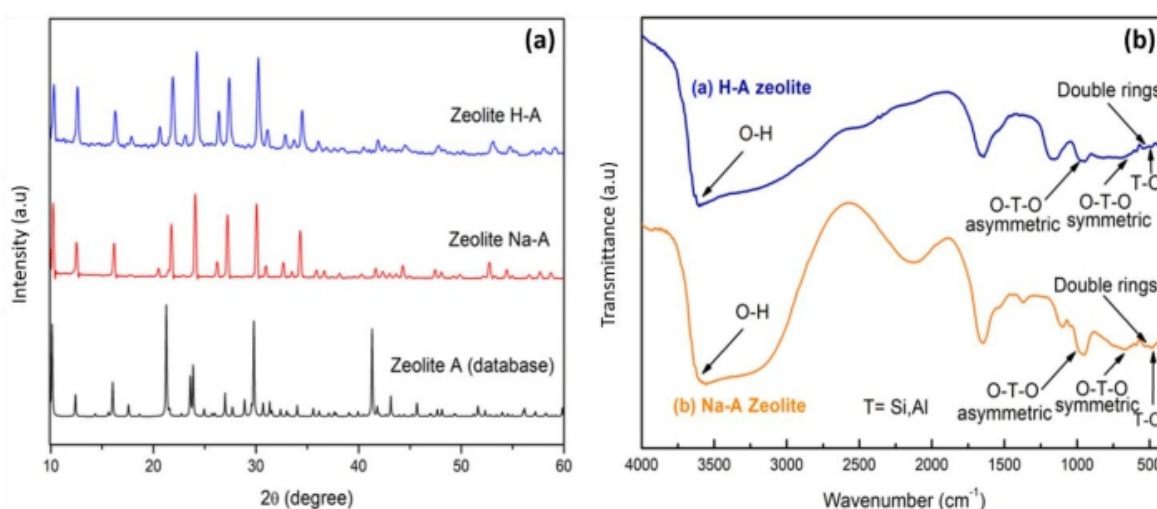
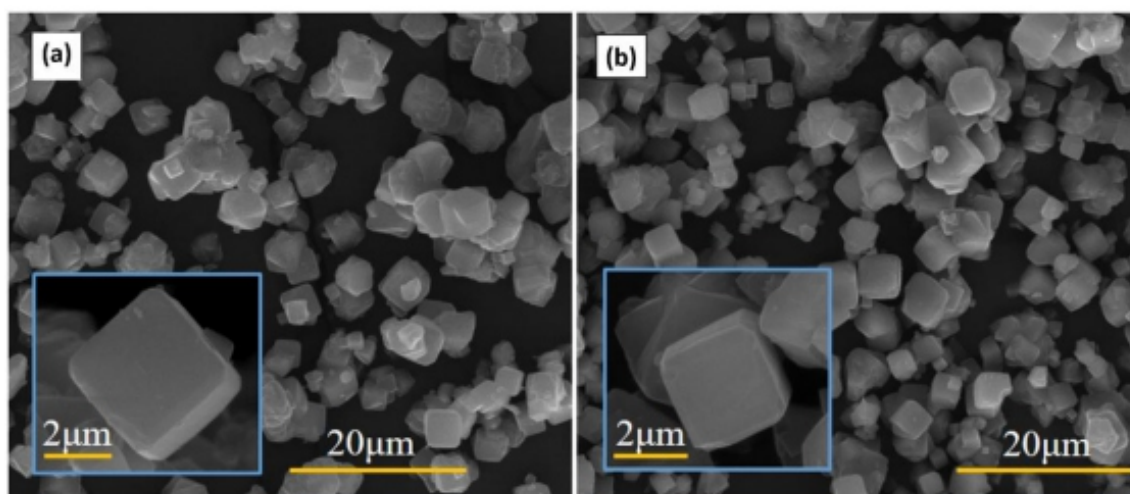


Figure 1. XRD pattern (a) and FTIR (b) of zeolite H-A and zeolite A.

Table 1. XRF results for activation of zeolite A.

Pretreatment	Al	Si	Na	P	K	Ti	Cr	Fe	Ni	Cu	Ba	Yb
Zeolite A (%)	31.8	64.7	5.7	1.3	0.62	0,97	0.11	0.23	0.054	0.14	-	-
Zeolite H-A (%)	32.8	65.0	3.3	-	0.31	0,90	0.096	0.24	0.01	0.11	0.2	0.2

The SEM results are shown in Figure 2. Figure 2a presented a typical cube-shaped micrograph with zeolite LTA morphology [30]. Figure 2b presented a micrograph of the pretreated zeolite that is not different from the initial zeolite. The zeolite has a uniform size even though there is a small crystal size around it. This shows the zeolite pretreatment from Na-A to H-A does not damage the initial zeolite structure. The average particle sizes of zeolite Na-A and H-A were 516.50 nm and 511.74 nm.

**Figure 2.** SEM of (a) zeolite Na-A and (b) zeolite H-A.

3.2. Characterization of Fe-TiO₂/zeolite H-A photocatalyst

XRD patterns of TiO₂, Fe-TiO₂, zeolite H-A, TiO₂/zeolite H-A and Fe-TiO₂/zeolite H-A are shown in Figure 3. The used TiO₂ showed sharp peaks at $2\theta = 25.34^\circ$, 37.83° , 48.07° , 53.92° , 55.09° , 62.72° , and these peaks indicated an anatase structure, which is in accordance with JCPDS card No.21-1272 [33,34]. The XRD pattern of Fe-TiO₂ did not show a significant diffractogram difference with pure TiO₂, as well as the characteristic peak of anatase at $2\theta = 25.3274^\circ$. After the impregnation, no diffractogram pattern related to the characteristics of Fe element was observed. This is possible because the amount of the added Fe(NO₃)₃·9H₂O powder was too low, so it is difficult to detect in XRD. On the other hand, the size of the Fe³⁺ ion radius (0.69 Å) is almost the same as the Ti⁴⁺ ion (0.74 Å), so Fe³⁺ ions can easily replace Ti⁴⁺ ions and combine into the structure of TiO₂ [35]. The XRD results show that there is no significant difference between TiO₂/zeolite H-A and Fe-TiO₂/zeolite H-A. XRD peaks at $2\theta = 25.34^\circ$ (TiO₂/zeolite H-A) and $2\theta = 25.31^\circ$ (Fe-TiO₂/zeolite H-A) indicate the presence of an anatase phase of TiO₂ and a typical zeolite diffractogram pattern, respectively. This shows that the addition of Fe³⁺ impregnation does not change the phase of TiO₂. Further characterization was carried out by looking at the elemental composition using XRF. The results of XRF characterization can be seen in Table 2.

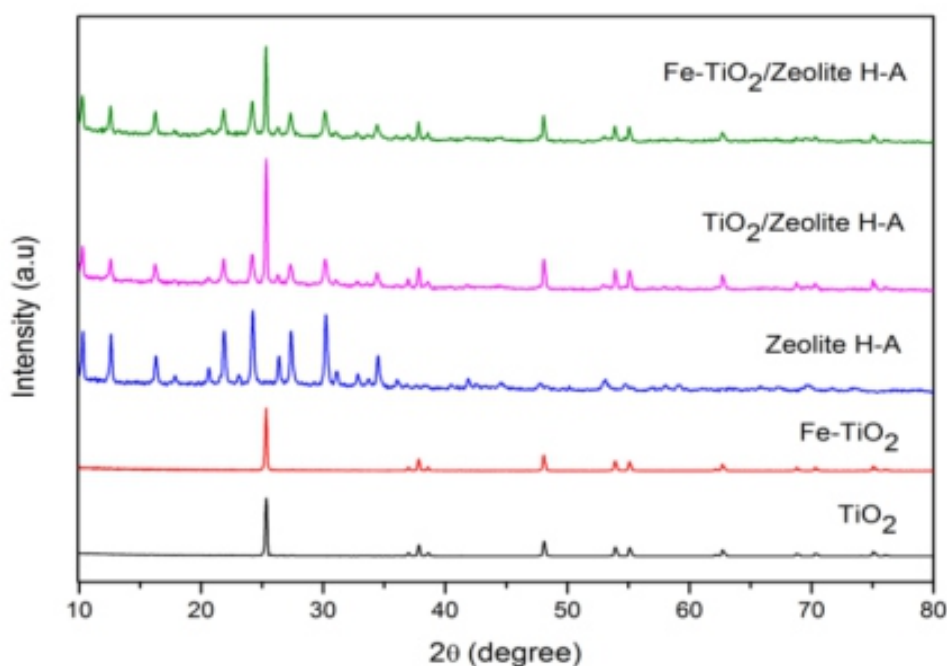


Figure 3. XRD pattern of TiO₂, Fe-TiO₂, zeolite H-A, TiO₂-zeolite H-A and Fe-TiO₂/zeolite H-A.

Table 2. XRF results of TiO₂, Fe-TiO₂, zeolite H-A, TiO₂/zeolite H-A, Fe-TiO₂/zeolite H-A.

Content (%)	TiO ₂	Fe-TiO ₂	Zeolite H-A	TiO ₂ /zeolite H-A	Fe-TiO ₂ /zeolite H-A
Ti	98.74	97.46	0.1	53.8	41.1
Fe	-	1.01	0.24	0.15	0.723
Si	-	-	65.0	26.7	23.2
Al	-	-	32.8	19.5	33.1
P	0.22	0.18	-	-	0.56
Ca	0.11	-	-	-	-
Z	0.22	-	-	-	-
Tm	0.21	-	-	-	-
W	0.24	-	-	-	-
Re	0.05	-	-	-	-
Pt	0.20	0.31	-	-	-
Os	-	0.91	-	-	-
Cu	-	-	0.11	0.10	0.096

Based on Table 2, the composition of the synthesized Fe-TiO₂/zeolite H-A photocatalyst consisted of Ti (TiO₂), Fe, Si and Al (zeolite component) with elemental contents of 41.1%, 0.723%, 23.2% and 33.1%, respectively. This confirmed that the synthesis of Fe-TiO₂/zeolite H-A photocatalyst was successfully carried out. However, from XRF and XRD results, it is not certain whether Fe-TiO₂ and TiO₂ have been evenly dispersed into the external surface of the zeolite.

The FT-IR measurement is carried out with a wavenumber range of 4000–400 cm⁻¹. The FT-IR spectra of TiO₂, Fe-TiO₂, zeolite H-A, TiO₂/zeolite H-A and Fe-TiO₂/zeolite are presented in Figure 4. The absorption band at 1400–400 cm⁻¹ was a typical absorption band for zeolite A. In addition, absorption bands appeared at 705.91 cm⁻¹ (symmetric) and 1002.16 cm⁻¹ (asymmetry) of stretching vibrations of

the T-O-T group (T = Si, Al). The absorption at 1644.7 cm^{-1} confirmed the stretching vibration of the O-H group produced from the silanol group (Si-O-H) and was strengthened by the appearance of the bending vibration of the O-H group of H₂O which was adsorbed on the absorption band $3306\text{--}3562\text{ cm}^{-1}$. The TiO₂ in the zeolite surface was confirmed by the appearance of absorption at $491.85\text{--}1049.28\text{ cm}^{-1}$, which was the vibrational absorption of the Ti-O-Ti group [36]. The impregnation of Fe³⁺ ions into the TiO₂ structure gave rise to new absorption at a wavenumber of 1063 cm^{-1} , which indicated the presence of vibrations from the Fe-O group. Previous studies reported that absorption at $1054\text{--}1065\text{ cm}^{-1}$ indicated Fe-O vibrations [37]. Overall, the spectrum can be observed to have a typical absorption of each component and does not overcome a significant spectrum shift in the final structure of the synthesized Fe-TiO₂/zeolite H-A photocatalyst. This indicated that the photocatalyst was reacted without any particular reaction [9].

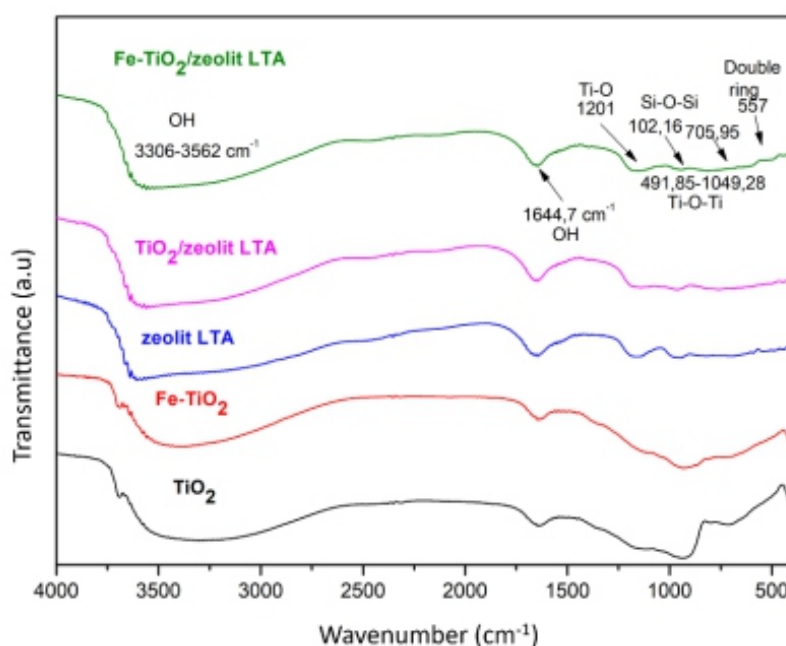


Figure 4. Comparison of the FT-IR Spectra of pure TiO₂, Fe-TiO₂, Zeolite H-A, TiO₂/zeolite H-A and Fe-TiO₂/zeolite H-A.

The SEM results are presented in Figure 5. The surface morphologies of TiO₂ and Fe-TiO₂ have no significant differences in shape and changes. The surface morphologies were spherical, and agglomerate with average particle sizes of 40.96 nm (TiO₂) and 40.56 nm (Fe-TiO₂), respectively. Figure 5c shows the surface morphology of the zeolite H-A with an average particle size of 511.74 nm. Figure 5d shows a change in the surface morphology of the zeolite after TiO₂ addition. It was observed that the TiO₂ agglomerates spread over the surface of the zeolite framework [38,39]. The photocatalyst micrograph of Fe-TiO₂/zeolite H-A in Figure 5e shows that more agglomerates are spread over the surface of the zeolite and cover the surface of the zeolite H-A framework, so the surface becomes rough and uneven after the addition of Fe in TiO₂. This indicates that Fe-TiO₂ has been well distributed on the surface of the zeolite and there is no typical change in morphology of zeolite after the addition of Fe-TiO₂ [5]. The average particle size of the Fe-TiO₂/zeolite H-A photocatalyst was 491.49 nm, and TiO₂/zeolite H-A was 487.29 nm.

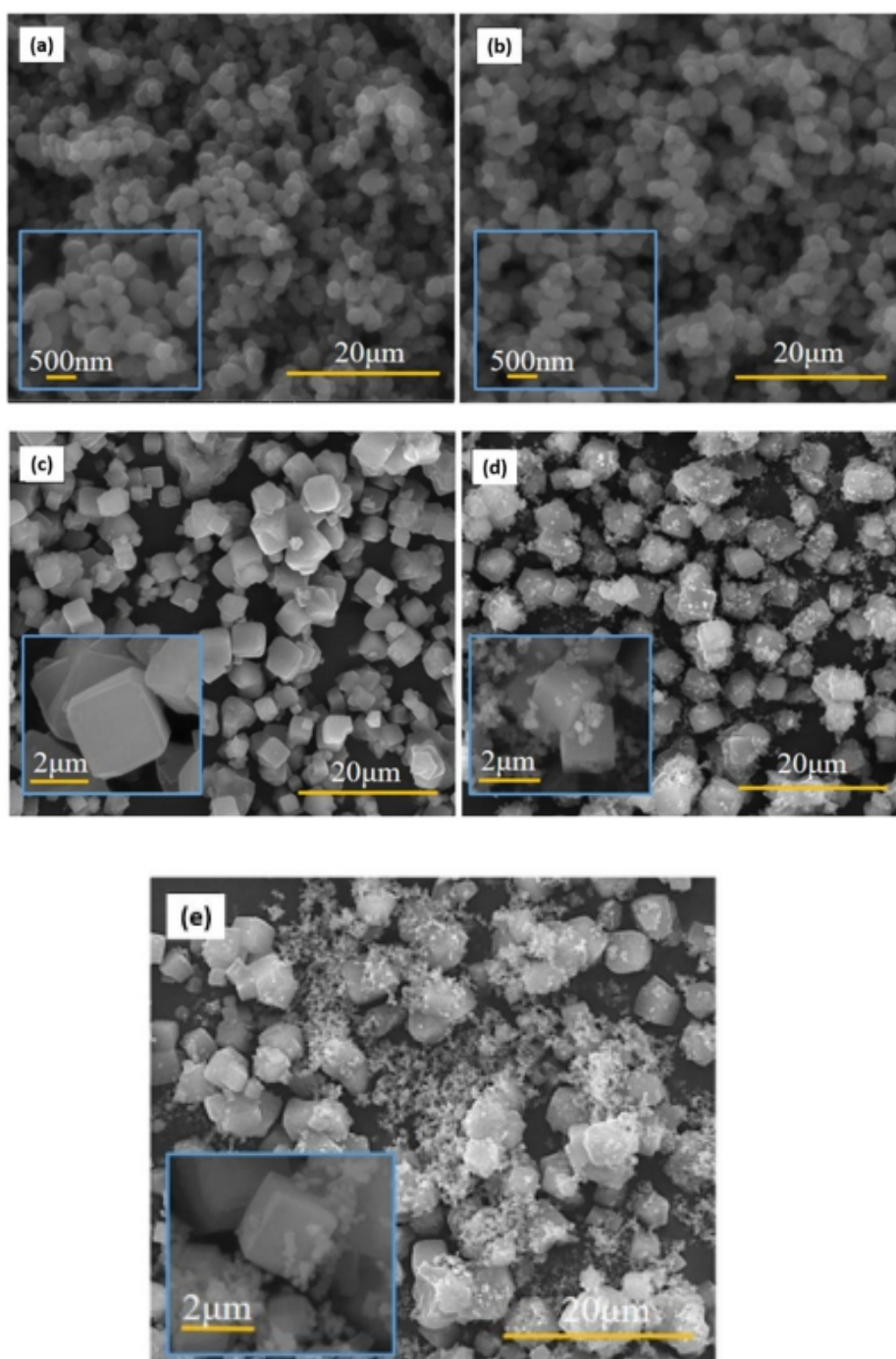


Figure 5. SEM results from (a) TiO₂, (b) Fe-TiO₂, (c) Zeolite H-A, (d) TiO₂/zeolite H-A and (e) Fe-TiO₂/zeolite H-A.

DRS analysis was used to investigate the optical properties of the synthesized photocatalyst. UV-Vis DRS analysis (Figure 6) was carried out at a wavelength of 200–1100 nm, and then the Tauc plot shown in Figure 7 was created. The energy band gaps of Fe-TiO₂, TiO₂/zeolite H-A and Fe-TiO₂/zeolite H-A obtained from the calculation of the Tauc plot (Figure 7a–c) were 3.18 eV, 3.24 eV and 3.16 eV, respectively. These results indicated that the energy band gap of the Fe-TiO₂/zeolite H-A photocatalyst has the smallest value. In addition, there was a decrease in the band gap after TiO₂ was added with Fe³⁺ ion and the zeolite. This indicates that the reducing of the energy band gap has been achieved.

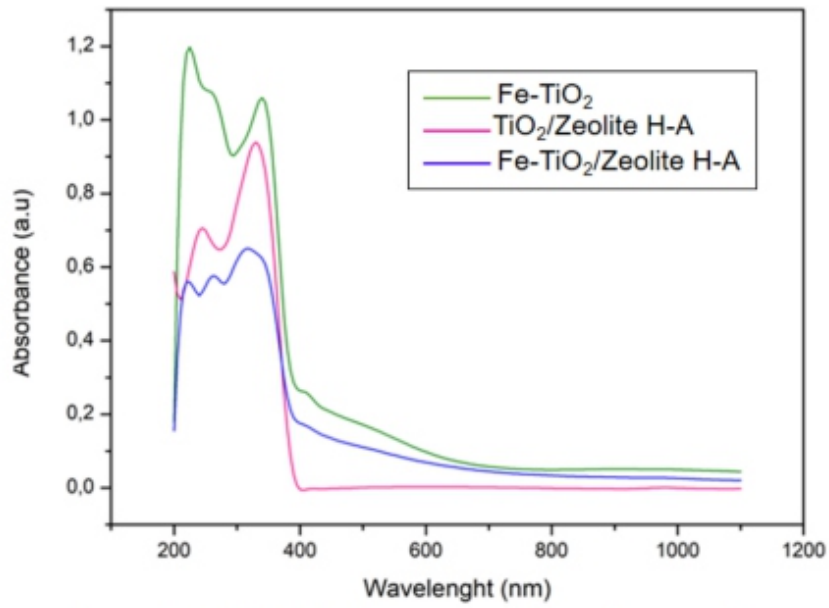


Figure 6. UV-Vis/DRS spectra of the photocatalyst.

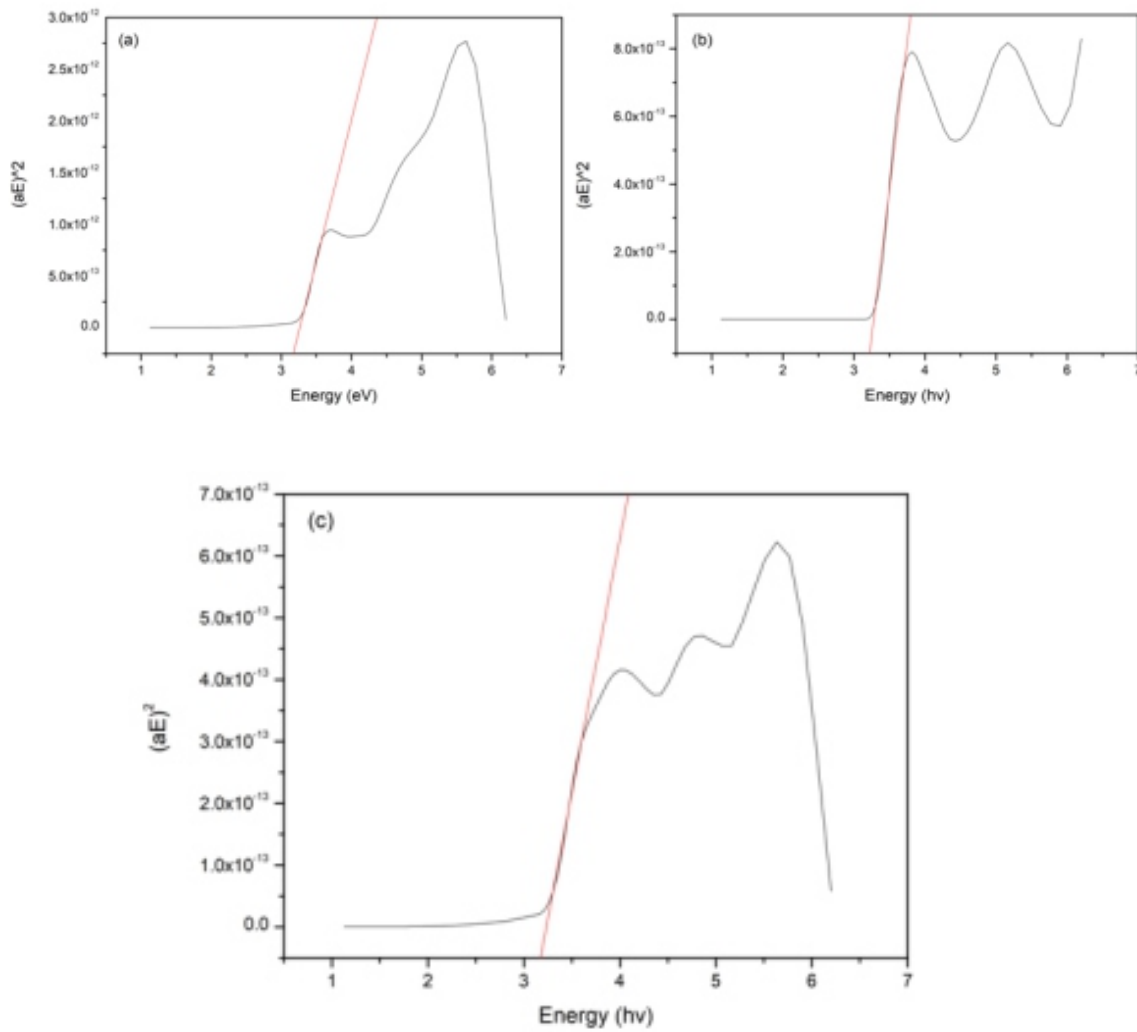


Figure 7. Result of Tauc plots for (a) Fe-TiO₂, (b) TiO₂/zeolite H-A and (c) Fe-TiO₂/zeolite H-A.

3.3. Study of the photocatalytic degradation

Methylene blue degradation with Fe-TiO₂/zeolite H-A through a photocatalytic process can be seen in Figure 8.

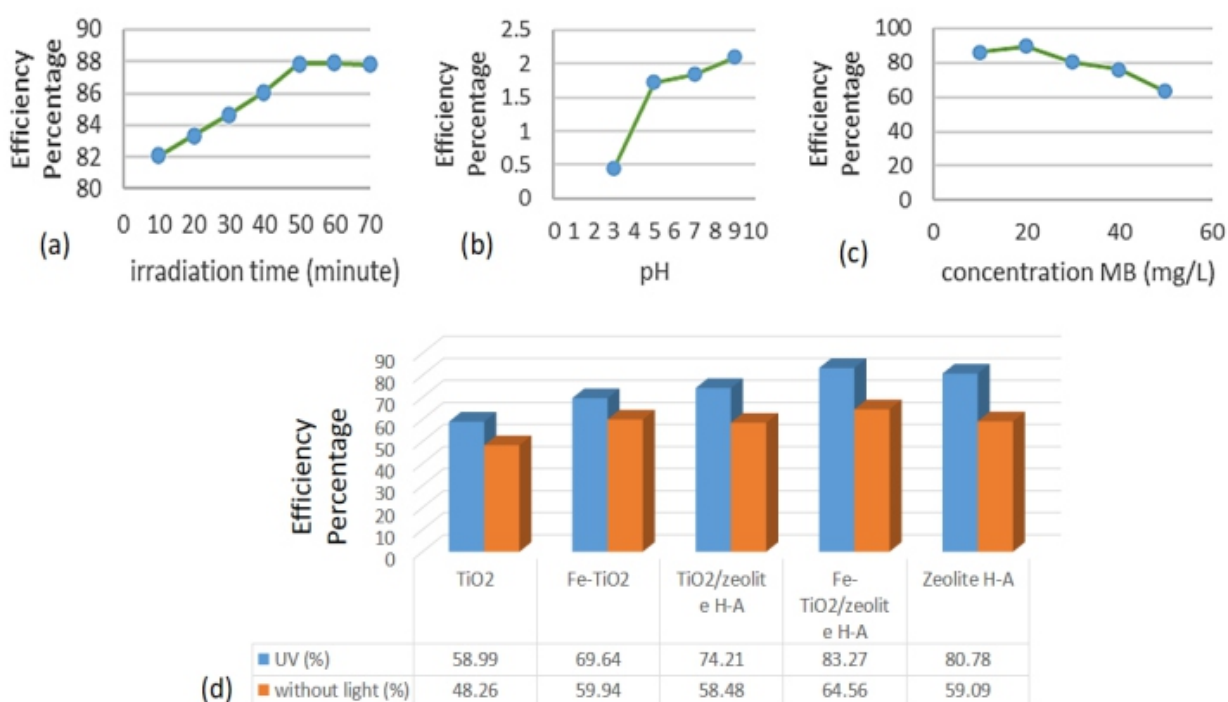


Figure 8. Methylene blue degradation: Efficiency percentage versus Irradiation (a), pH (b), dye concentration (c) and the photocatalyst (d).

Based on Figure 8, the optimum irradiation time of the Fe-TiO₂/zeolite H-A photocatalyst to degrade methylene blue was 50 min with a degradation of 87.87%. After it, the decrease of irradiation time occurred due to the Fe-TiO₂/zeolite H-A photocatalyst being saturated. Moreover, pH plays a very important role in the formation of hydroxyl radicals (OH•) [40]. The optimum pH was pH 9, because methylene blue is a cationic dye (positive charge), so at alkaline pH it can increase the photocatalytic degradation. At alkaline pH, the surface of TiO₂ is negatively charged, which causes an increase in the electrostatic attraction between methylene blue and TiO₂ in the photocatalyst. This can be explained by the theory of pH_{pzc} (pH Point of Zero Charge). TiO₂ has a pH_{pzc} value of 6.8 when the oxide surface is uncharged. The surface of TiO₂ is positively charged when the pH value is less than 6.8 (acidic pH) and negatively charged when pH more than 6.8 (alkaline pH). Finally, efficiency percentage of methylene blue degradation increased with increasing initial methylene blue concentration until it reached a certain limit and then decreased with increasing concentration. Optimum concentration of Methylene Blue was 20 mg/L. If a small amount of UV light reaches the photocatalyst, then the number of electrons will reduce [41]. The presence of zeolite as a support for TiO₂ will result in the preservation of nearby dye molecules, thereby increasing the rate of degradation [5]. Another reason is that, with the presence of Fe element and zeolite H-A as a photocatalyst, Fe-TiO₂/zeolite H-A has a smaller band gap energy than pure TiO₂. The narrower energy band gap means that the distance between the valence band and the conduction band is narrower, so electron excitation is easier, and consequently photocatalytic activity is increasing [42]. So, the degradation performance of the modified TiO₂ was higher than the pure TiO₂ [43].

4. Conclusions

Fe-TiO₂/zeolite H-A photocatalyst was synthesized using the impregnation method. The synthesized photocatalyst was used for the cationic degradation of methylene blue as a model pollutant in wastewater. The successful synthesis of Fe-TiO₂/zeolite H-A was proven by XRD, SEM, FT-IR and UV-Vis/DRS. XRD results at $2\theta = 25.3^\circ$ showed an anatase phase of the photocatalyst, SEM results showed particle size about 491.49 nm, FT-IR analysis obtained typical bands of zeolite at wavenumbers 490 and 1720 cm⁻¹, and the absorption appeared at 491.85–1049.28 cm⁻¹, which was the vibrational absorption of the Ti-O-Ti group. The addition of Fe³⁺ ions into the TiO₂ structure gave rise to new absorption at 1063 cm⁻¹, which indicated the presence of vibrations from the Fe-O group. The band gap width of the synthesized nanocomposite was 3.16 eV, and this value was very close to the band gap of pure TiO₂. Furthermore, the photocatalytic efficiency of Fe-TiO₂/zeolite H-A against methylene blue was 89.58% with optimum conditions: irradiation time of 50 minutes, pH 9 and concentration of methylene blue about 20 mg/L. The Fe-TiO₂/zeolite H-A photocatalyst has been successfully synthesized and can be developed as a promising photocatalyst for the degradation of wastewater dyes.

Acknowledgments

We would like to thank to LPPM Universitas Negeri Malang for supporting the study.

Conflict of interests

The authors stated that there is no conflict of interest for the study.

References

1. Areerob Y, Cho KY, Oh WC (2017) Microwave assisted synthesis of graphene-Bi₈La₁₀O₂₇-Zeolite nanocomposite with efficient photocatalytic activity towards organic dye degradation. *J Photoch Photobio A* 340: 157–169. <https://doi.org/10.1016/j.jphotochem.2017.03.018>
2. Karuppasamy P, Nisha NRN, Pugazhendhi A, et al. (2021) An investigation of transition metal doped TiO₂ photocatalysts for the enhanced photocatalytic decoloration of methylene blue dye under visible light irradiation. *J Environ Chem Eng* 9: 105254. <https://doi.org/10.1016/j.jece.2021.105254>
3. Qaderi J, Mamat CR, Jalil AA (2021) Preparation and characterization of copper, iron, and nickel doped titanium dioxide photocatalysts for decolorization of methylene blue. *Sains Malays* 50: 135–149. <https://doi.org/10.17576/jism-2021-5001-14>
4. Javanbakht V, Ghoreishi SM (2017) Application of response surface methodology for optimization of lead removal from an aqueous solution by a novel superparamagnetic nanocomposite. *Adsorpt Sci Technol* 35: 241–60. <https://doi.org/10.1177/0263617416674474>
5. Aghajari N, Ghasemi Z, Younesi H, et al. (2019) Synthesis, characterization and photocatalytic application of Ag-doped Fe-ZSM-5@TiO₂ nanocomposite for degradation of reactive red 195 (RR 195) in aqueous environment under sunlight irradiation. *J Environ Health Sci* 17: 219–232. <https://doi.org/10.1007/s40201-019-00342-5>
6. Znad H, Abbas K, Hena S, et al. (2018) Synthesis a novel multilamellar mesoporous TiO₂/ZSM-5 for photo-catalytic degradation of methyl orange dye in aqueous media. *J Environ Chem Eng* 6: 218–227. <https://doi.org/10.1016/j.jece.2017.11.077>
7. Shan AY, Ghazi TIM, Rashid SA (2010) Immobilisation of titanium dioxide onto supporting materials in heterogeneous photocatalysis: A review. *Appl Catal A-Gen* 389: 1–8. <https://doi.org/10.1016/j.apcata.2010.08.053>
8. Vaez Z, Javanbakht V (2020) Synthesis, characterization and photocatalytic activity of ZSM-5/ZnO nanocomposite modified by Ag nanoparticles for methyl orange degradation. *J Photoch Photobiol A* 388: 112064. <https://doi.org/10.1016/j.jphotochem.2019.112064>

9. Badvi K, Javanbakht V (2021) Enhanced photocatalytic degradation of dye contaminants with TiO₂ immobilized on ZSM-5 zeolite modified with nickel nanoparticles. *J Clean Prod* 280:124518. <https://doi.org/10.1016/j.jclepro.2020.124518>
10. Massoudinejad M, Sadani M, Gholami Z, et al. (2019) Optimization and modeling of photocatalytic degradation of Direct Blue 71 from contaminated water by TiO₂ nanoparticles: Response surface methodology approach (RSM). *Iran J Catal* 9: 121–132.
11. Ghasemi Z, Younesi H, Zinatizadeh AA (2016) Preparation, characterization and photocatalytic application of TiO₂/Fe-ZSM-5 nanocomposite for the treatment of petroleum refinery wastewater: Optimization of process parameters by response surface methodology. *Chemosphere* 159: 552–564. <https://doi.org/10.1016/j.chemosphere.2016.06.058>
12. Safajou H, Khojasteh H, Salavati-niasari M, et al. (2017) Enhanced photocatalytic degradation of dyes over graphene/Pd/TiO₂ nanocomposites: TiO₂ nanowires versus TiO₂ nanoparticles. *J Colloid Interf Sci* 498: 423–432. <https://doi.org/10.1016/j.jcis.2017.03.078>
13. Bian H, Zhang Z, Xu X, et al. (2020) Photocatalytic activity of Ag/ZnO/AgO/TiO₂ composite. *Physica E* 124: 114236. <https://doi.org/10.1016/j.physe.2020.114236>
14. Derakhshan-Nejad A, Rangkooy HA, Cheraghi M, et al. (2020) Removal of ethyl benzene vapor pollutant from the air using TiO₂ nanoparticles immobilized on the ZSM-5 zeolite under UV radiation in lab scale. *J Environ Health Sci* 18: 201–209. <https://doi.org/10.1007/s40201-020-00453-4>
15. Pedroza-herrera G, Medina-ramírez IE, Lozano-álvarez JA, et al. (2020) Evaluation of the photocatalytic activity of copper doped TiO₂ nanoparticles for the purification and/or disinfection of industrial effluents. *Catal Today* 341: 37–48. <https://doi.org/10.1016/j.cattod.2018.09.017>
16. Al-Mamun MR, Kader S, Islam MS, et al. (2019) Photocatalytic activity improvement and application of UV-TiO₂ photocatalysis in textile wastewater treatment: A review. *J Environ Chem Eng* 7: 103248. <https://doi.org/10.1016/j.jece.2019.103248>
17. Arifiyana D, Murwani IK (2013) Pengaruh doping Logam Fe pada CaF₂ terhadap Struktur Ca_{1-x}F_xF₂. *J Sains dan Seni Pomits* 2: 54–56.
18. Khatamian M, Hashemian S, Yavari A, et al. (2012) Preparation of metal ion (Fe³⁺ and Ni²⁺) doped TiO₂ nanoparticles supported on ZSM-5 zeolite and investigation of its photocatalytic activity. *Mater Sci Eng B-Adv* 177: 1623–1627. <https://doi.org/10.1016/j.mseb.2012.08.015>
19. Khairy M, Zakaria W (2014) Effect of metal-doping of TiO₂ nanoparticles on their photocatalytic activities toward removal of organic dyes. *Egypt J Pet* 23: 419–426. <https://doi.org/10.1016/j.ejpe.2014.09.010>
20. Hosseini MS, Ebratkhan M, Shayegan Z, et al. (2020) Investigation of the effective operational parameters of self-cleaning glass surface coating to improve methylene blue removal efficiency; application in solar cells. *Sol Energy* 207: 398–408. <https://doi.org/10.1016/j.solener.2020.06.109>
21. Noorjahan M, Kumari VD, Subrahmanyam M, et al. (2004) A novel and efficient photocatalyst: TiO₂-HZSM-5 combine thin film. *Appl Catal B-Environ* 47: 209–213. <https://doi.org/10.1016/j.apcatb.2003.08.004>
22. Mahalakshmi M, Priya SV, Arabindoo B, et al. (2009) Photocatalytic degradation of aqueous propoxur solution using TiO₂ and H β zeolite-supported TiO₂. *J Hazard Mater* 161: 336–343. <https://doi.org/10.1016/j.jhazmat.2008.03.098>
23. Loiola AR, Andrade JCRA, Sasaki JM, et al. (2012) Structural analysis of zeolite NaA synthesized by a cost-effective hydrothermal method using kaolin and its use as water softener. *J Colloid Interf Sci* 367: 34–39. <https://doi.org/10.1016/j.jcis.2010.11.026>
24. Wuntu AD, Kamu VS, Kumaunang M (2019) Crystallization temperature of NaA zeolite prepared from gel and aluminum hydroxide. *Chem Prog* 4: 1–4.
25. Afrozi AS, Salam R, R A, et al. (2016) Pengolahan limbah methylen blue secara fotokatalisis TiO₂

- dengan penambahan Fe dan zeolit. *Prosiding Seminar Nasional Teknologi Pengelolaan Limbah*, 29–36. Available from: <http://repo-nkm.batan.go.id/7417/>.
26. Pratama NA, Artsanti P (2019) Effect of aeration treatment on methylene blue removal using TiO₂-zeolite. *Proceeding International Conference on Science and Engineering 2*: 219–224. <https://doi.org/10.14421/icse.v2.89>
27. Estiaty LM (2015) Synthesis and characterization of zeolite-TiO₂ from modified natural zeolite. *Teknologi Miner dan Batubara 11*: 181–190.
28. Erwanto E, Yulinda Y, Nabela Q (2020) Pengaruh Penambahan Ion Nitrat (NO₃⁻) terhadap Kinetika Fotodegradasi Zat Warna Metilen Biru Menggunakan Zeolit-TiO₂. *J Inovasi Teknik Kimia 5*: 59–67. Available from: <http://dx.doi.org/10.31942/inteka.v5i2.3812>.
29. Septian DD, Sugiarti S (2019) Modifikasi Zeolit Alam Ende dengan Garam Logam serta Potensinya Sebagai Katalis Transformasi Glukosa Menjadi 5-Hidroksimetilfurfural (HMF). *ALCHEMY J Penelit Kim 15*: 203–218. <https://doi.org/10.20961/alchemy.15.2.28180.203-218>
30. Rigo RT, Prigol C, Antunes Á, et al. (2013) Synthesis of ZK4 zeolite: An LTA-structured zeolite with a Si/Al ratio greater than 1. *Mater Lett 102*: 87–90. <https://doi.org/10.1016/j.matlet.2013.03.120>
31. Ginting SB, Sari DP, Iryani DA, et al. (2019) Sintesis Zeolit T Lynde Type-A (LTA) Dari Zeolit Alam Lampung (ZAL) Menggunakan Metode Step Change Temperature Of Hydrothermal Dengan Variasi SiO₂/Al₂O₃ Diaplikasikan Untuk Dehidrasi Etanol. *J Chem Process Eng 4*: 32–44. <https://doi.org/10.33536/jcpe.v4i1.324>
32. Asrori MR, Santoso A, Sumari S (2022) Initial defect product on immiscible mixture of palm oil: Ethanol by amphiphilic chitosan/Zeolite LTA as optimization of microemulsion fuel. *Ind Crops Prod 180*: 114727. <https://doi.org/10.1016/j.indcrop.2022.114727>
33. Treacy MMJ, Higgins JB (2007) *Collection of Simulated XRD Powder Patterns for Zeolites*, 5 Eds., Elsevier.
34. Sescu AM, Favier L, Latic D, et al. (2021) TiO₂ doped with noble metals as an efficient solution for the photodegradation of hazardous organic water pollutants at ambient conditions. *Water (Switzerland) 13*: 1–18. <https://doi.org/10.3390/w13010019>
35. Sood S, Umar A, Mehta SK, et al. (2015) Highly effective Fe-doped TiO₂ nanoparticles photocatalysts for visible-light driven photocatalytic degradation of toxic organic compounds. *J Colloid Interf Sci 450*: 213–223. <https://doi.org/10.1016/j.jcis.2015.03.018>
36. Cacciato G, Zimbone M, Ruffino F, et al. (2016) TiO₂ nanostructures and nanocomposites for sustainable photocatalytic water purification, In: Larramendy ML, Soloneski S, *Green Nanotechnology-Overview and Further Prospects*, Croatia: Janeza Trdine. <https://doi.org/10.5772/62620>
37. Pratiwi E, Harlia H, Aritonang AB (2020) Sintesis TiO₂ terdoping Fe³⁺ untuk Degradasi Rhodamin B Secara Fotokatalisis dengan Bantuan Sinar Tampak. *Positron 10*: 57–63. <https://doi.org/10.26418/positron.v10i1.37739>
38. Al-Harbi LM, Kosa SA, Abd El Maksod IH, et al. (2015) The photocatalytic activity of TiO₂-zeolite composite for degradation of dye using synthetic UV and Jeddah sunlight. *J Nanomater 16*: 46. <https://doi.org/10.1155/2015/565849>
39. Li H, Zhang W, Liu Y (2020) HZSM-5 zeolite supported boron-doped TiO₂ for photocatalytic degradation of ofloxacin. *J Mater Res Technol 9*: 2557–2567. <https://doi.org/10.1016/j.jmrt.2019.12.086>
40. Sahel K, Perol N, Chermette H, et al. (2007) Photocatalytic decolorization of Remazol Black 5 (Rb5) and Procion Red MX-5B-Isotherm of adsorption, kinetic of decolorization and mineralization. *Appl Catal B-Environ 77*: 100–109. <https://doi.org/10.1016/j.apcatb.2007.06.016>
41. Khan I, Saeed K, Zekker I, et al. (2022) Review on methylene blue: Its properties, uses, toxicity and

photodegradation. *Water* 14: 242. <https://doi.org/10.3390/w14020242>

42. Sutanto H, Wibowo S (2015) *Semikonduktor Fotokatalis Seng Oksida dan Titania: Sintesis, Deposisi dan Aplikasi*. Available from: <http://eprints.undip.ac.id/49049/>.

43. Asiltürk M, Sayilkan F, Arpaç E (2009) *Effect of Fe³⁺ ion doping to TiO₂ on the photocatalytic degradation of Malachite Green dye under UV and vis-irradiation*. *J Photoch Photobiol A* 203:64–71. <https://doi.org/10.1016/j.jphotochem.2008.12.021>

Effect of sub-zero treatments on hardness and corrosion properties of low-alloy nickel steel

Vinda Puspasari^{1,*}, Satrio Herbirowo¹, Alvin Muhammad Habieb^{1,2}, Dedi Pria Utama¹, Rahadian Roberto¹ and Bintang Adjiantoro¹

¹ Research Center for Metallurgy and Materials, National Research and Innovation Agency, Gedung 470, South Tangerang, Banten, 15314, Indonesia

² Nano Center Indonesia, South Tangerang, Banten, 15314, Indonesia

ABSTRACT

Low alloy nickel steel was chosen for this experiment because it is suitable for grinding balls application due to its high hardness and corrosion resistance. This study aimed to see the effect of different sub-zero treatments on the hardness, fractography and corrosion properties of low alloy nickel steel. The prepared specimens were heated to the austenitizing temperature of 980 °C in a furnace for one hour and water-quenched until they reached room temperature. Furthermore, the quenched specimens were chilled in liquid nitrogen for a varied time of 10, 60 or 360 min, followed by tempering treatment at 200 °C for one hour. According to the hardness test, the sub-zero treatment is effective in hardening materials, where the hardness value increases as the sub-zero treatment time increases, ranging from 204.93 to 417.98 HV. The fractography test indicated ductile fracture characterized by dimples at the fractured surface. Moreover, the corrosion test showed an enhancement of corrosion resistance with increased sub-zero treatment time.

Keywords: sub-zero treatment; grinding ball; hardness; fractography; corrosion

1. Introduction

Grinding in the milling process is an essential process to reduce the sizes of particles in mining metallurgy, the cement industry and the chemical and power industries using steel grinding balls [1]. Almost half of the world's milling circuits use ball mills, and 90% of mining operations utilize balls as grinding devices [2]. One of the most popular milling machines is the cement mill, which is used to crush raw materials such as lime, silicate, alumina and iron oxide using grinding balls [3]. The quality and efficiency of the grinding process are greatly affected by the grade and characteristics of grinding balls [4]. The minerals usually have high hardness, meaning the grinding ball must maintain its shape during the milling process [5]. Therefore, the grinding balls must meet the requirements such as good hardness and corrosion resistance [6].

Grinding balls are commonly made from low alloy steel with different carbon contents (0.7 to 0.8 wt%) and alloyed with manganese, chromium (up to 1 wt%), molybdenum (up to 0.025 wt%) and copper (up to 1 wt%) [7]. The alloying method is useful not only to maintain a suitable value of hardness but also to improve corrosion resistance along the ball cross-section [8]. The low alloy nickel steel was chosen in this experiment because it performs better than high carbon martensitic iron for grinding ball application due to the work hardening effect during the service [9].

Furthermore, the presence of chromium and nickel in these alloys will significantly improve mechanical properties and corrosion resistance [10]. According to the previous work, the low alloy steels are proven to have high hardness and abrasion resistance properties, which are suitable for grinding balls [11]. The addition of Cr, Mo and Cu also affects the hardness gradient of the grinding ball from the hard surface (martensite) to the soft core (perlite) [12].

The critical factor in grinding ball application is the total wear of the grinding balls, which consists of abrasion, corrosion and impact properties [13]. For that reason, it is hard to divide the contributions of each mechanism toward wear properties [14]. The corrosion and dissolution of metal surfaces during grinding becomes more than half of the complete wear of grinding balls [15]. The

corrosion mechanism is also important to explore because of its significant effect on the total wear of grinding balls [16]. Furthermore, to obtain the best performance and durability of grinding balls, the affecting factors such as fabricating methods based on properties, heat treatment and chemical composition become crucial [5]. In this paper, the value of hardness, surface cracking and corrosion properties will be evaluated.

The utilization of heat treatment with the rolled steel balls, such as quenching followed by tempering, is appropriate to enhance the mechanical properties [17]. The addition of sub-zero treatment as the hardening treatment to the grinding balls is believed to enhance the durability of grinding balls [18]. Sub-zero treatment (also called cryogenic treatment) refers to the treatment process at low temperatures (lower than $-80\text{ }^{\circ}\text{C}$) added to the conventional heat treatment (CHT) [19]. The effect of the sub-zero treatment can cause a significant reduction of the retained austenite and martensite refinement and balance out the products [20]. The essential factor in subzerotreatment is that the treatment should be done as quickly as possible after quenching to avoid the degradation of the properties of materials [21]. This study investigated the effects of different sub-zero treatments on the hardness, fractography and corrosion properties of low alloy nickel steel.

2. Materials and methods

The chemical composition of low alloy nickel steel is presented in Table 1. The process was started by specimen preparation using the machining process to customize sample testing standards. The prepared specimens were subjected to the conventional heat treatment, which consisted of gradual heating up to the austenitizing temperature of $980\text{ }^{\circ}\text{C}$ in the furnace for 1 h. Then, the specimens were quenched until they reached room temperature using water. After that, the quenched specimens were cooled using liquid nitrogen for 10 (C10), 60 (C60) and 360 (C360) min. Furthermore, the Fe-Ni-Cr-Mo specimens were removed from the nitrogen reaction tube and placed in the open air until their temperature reached room temperature. Then, the Fe-Ni-Cr-Mo specimens were tempered at $200\text{ }^{\circ}\text{C}$ for 1 h to minimize residual stress.

Table 1. Chemical compositions of Fe-Ni-Cr-Mo specimens.

Specimen	Al (wt%)	Mn (wt%)	Si (wt%)	Cr (wt%)	Ni (wt%)	Mo (wt%)	C (wt%)	Fe (wt%)
FeNiCrMo-3	0.01	0.35	0.42	0.03	2.26	0.0008	0.02	Bal.
FeNiCrMo-4	0.08	0.47	0.48	1.23	2.03	0.89	0.04	Bal.

The mechanical properties of samples were examined using the micro-Vickers test with 0.3 kN of loading and 10 s of pressing time. The fractography images of specimens after the impact test were observed using SEM-EDS. Furthermore, the electrochemical measurement test was done using the Gamry G750 corrosion measurement system in 3.5% NaCl solution. The 1.1 cm² specimens were cut using a cutting machine and installed to copper wire for electrical contact. After that, the specimens were mounted using resin to cover the unexposed area. The mounted specimens were ground using 120–1200 grit SiC paper with the help of distilled water. Electrochemical measurements were performed using GAMRY Series G-750 Corrosion Measurement System. The electrochemical measurement utilized Pt electrode as the counter electrode, saturated calomel as thereference electrode and the specimens as the working electrode. The open-circuit potential (Eocp) was measured, which is continued by the Tafel polarization and cyclic polarization test. The potentiodynamic polarization test was performed at a scan rate of 1 mV/s in $\pm 250\text{ mV}$ from the OCP potential. The measurement of cyclic polarization was done based on ASTM G-61 using potential of -500 mV to $+1500\text{ mV}$, current density of 10 mA/cm², forward scan rate of 5 mV/s and reverse scan of 2.5 mV/s. The corroded samples were observed using SEM-EDS

to determine corrosion morphology and elements contained in corrosion products.

3. Results and discussion

3.1. Effect of sub-zero treatment on micro-Vickers hardness test results

The hardness properties were characterized using micro-Vickers at six spot locations, and the averaged value was calculated. The labels of specimens showed the time of sub-zero treatment and material type; for instance, C10-3 indicated 10 min of sub-zero treatment and FeNiCrMo-3 specimens. The analytical graph of micro-Vickers results was also processed using IBM-SPSS statistical software and the normality test method using Kolmogorov-Smirnov and Shapiro-Wilk. Figure 1 illustrates the results of the micro-Vickers hardness test of FeNiCrMo specimens that experienced the sub-zero treatment process, as illustrated. The sub-zero treatment is effective in hardening materials, where the hardness value increases as the sub-zero treatment time increases. The hardness value of FeNiCrMo-3 specimens shows values of 204.93 for C10, 228.18 for C60, and 238.55 for C360, indicating an increase in hardness value. An increase of hardness with increasing sub-zero treatment time can enhance plastic deformation resistance because of restricted dislocation movement [22]. The longer the sub-zero treatment duration is, the more dislocation movement is prevented, resulting in a greater hardness value. The hardness and modulus values dropped as the indenter displacement expanded [23]. Furthermore, the enhancement of flow stress (α hardness) with decreasing temperatures can also enhance sub-zero treatment specimen's wear and friction behavior [24].

The hardness values of FeNiCrMo-4 specimens show the values of 390.27 for C10, 417.98 for C60 and 333.65 for C360. The hardness value of FeNiCrMo-4 specimens with 60 minutes of subzero treatment time is the highest of all the specimens worth 418 Hv. The increase of hardness value is caused by the uniform distribution and refinement of the grains after sub-zero treatment [25]. The hardness value of FeNiCrMo-4 specimens is higher than FeNiCrMo-3 with the same sub-zero treatment time. This phenomenon is affected by CrMo chemical composition in the alloy, where the FeNiCrMo-4 specimens have a higher content of element alloying [26]. Table 2 shows that the significance value is above 0.05 using Kolmogorov-Smirnov and Shapiro-Wilk normality test, so the hardness properties results are normally distributed. Table 3 shows the results of ANOVA for hardness using micro-Vickers hardness measurements, which reveals that the Sig value $< \alpha$ (0.05) proves the variation in process treatment has an effect.

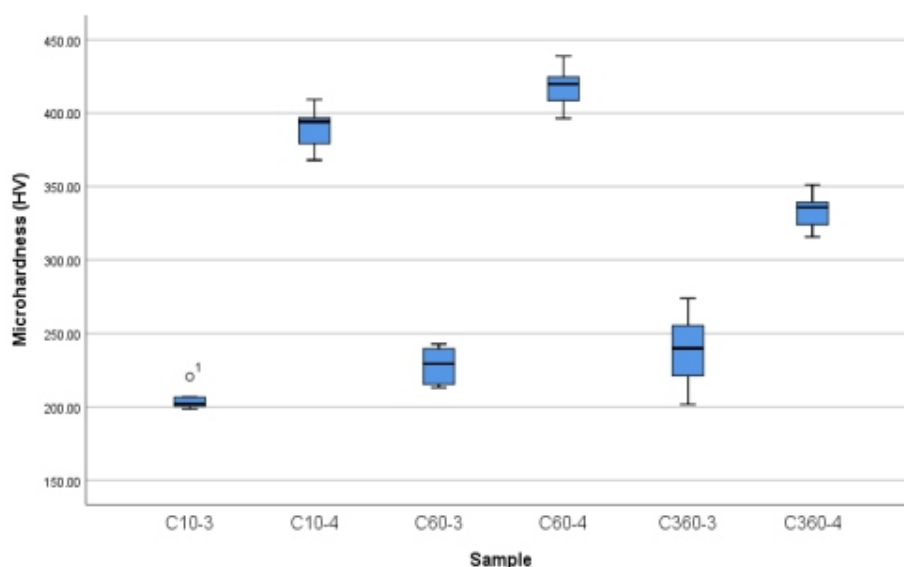


Figure 1. The hardness properties of the FeNiCrMo with various quenched.

Table 2. The hardness test data of FeNiCrMo with normality test.

	Specimens	Kolmogorov-Smirnov ^a			Shapiro-Wilk		
		Statistic	df	Sig.	Statistic	df	Sig.
Hardness	C10-3	0.261	6	0.200*	0.789	6	0.047
	C10-4	0.222	6	0.200*	0.953	6	0.765
	C60-3	0.276	6	0.169	0.837	6	0.123
	C60-4	0.159	6	0.200*	0.986	6	0.978
	C360-3	0.158	6	0.200*	0.987	6	0.980
	C360-4	0.200	6	0.200*	0.973	6	0.910

Table 3. The hardness test data of FeNiCrMo with one-way ANOVA test.

Hardness	Sum of squares	df	Mean square	F	Sig.
Between groups	246847.152	5	49369.430	197.946	0.000019
Within groups	7482.253	30	249.408		
Total	254329.406	35			

3.2. Effect of Sub-zero treatment on fractography of Fe-Ni-Cr-Mo results

Figure 2a–d indicates SEM characterization results of low alloy nickel steel specimens' fracture surfaces, showing dimples (black arrows) and brittle fracture (red arrows) in all specimens. Figure 2a characterizes ductile fracture, which reveals dimples (black arrows) in the fractured surface for the FeNiCrMo C10-4 sample. Figure 2c shows fine dimples (black arrows) in the fractured surface conforming to ductile fracture characteristics. This phenomenon is caused by increased formability from low alloy nickel steel alloy and the temperature sensitivity of stress required for dislocation motion [27]. The shorter time of sub-zero treatment causes lower stress involved to move dislocation, which causes deformation is preferred. Figure 2b,d indicate ductile tearing and quasi cleavage facets [28]. This phenomenon happened due to the enhancement of sub-zero treatment time, which increases the difficulty in cross slip in the material, affecting the enhancement of flow stress, strain hardening exponent, and decreasing the plasticity of materials [29].

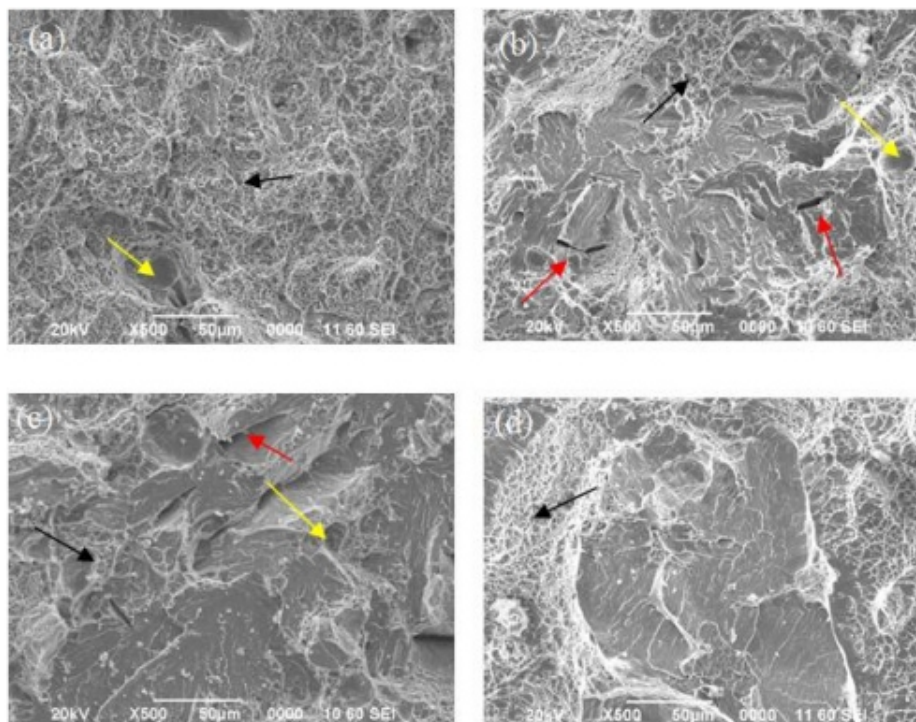


Figure 2. Fractography images of (a) FeNiCrMo C10-3, (b) FeNiCrMo C60-3, © FeNiCrMo C10-4, (d) FeNiCrMo C60-4 showing topological changes.

The microvoids with spherical shapes were also found in Figure 2a–c with yellow arrow marks, but Figure 2d is not showing the microvoids. The microvoids were formed in heterogeneous areas where the size and distribution of heterogeneities influence void formation, growth and coalescence [30]. The higher hardness of the matrix will enhance the number of voids required to propagate a fracture [22]. Figure 3a–d refers to EDS mapping of low alloy nickel steel fracture surfaces. Figure 3a,b indicates C, Fe and Ni elements in the specimens where the dark areas are less elemental. Figure 3c,d shows the elements C, Cr, Fe, Ni and Mn evenly distributed in the FeNiCrMo-4 specimens.

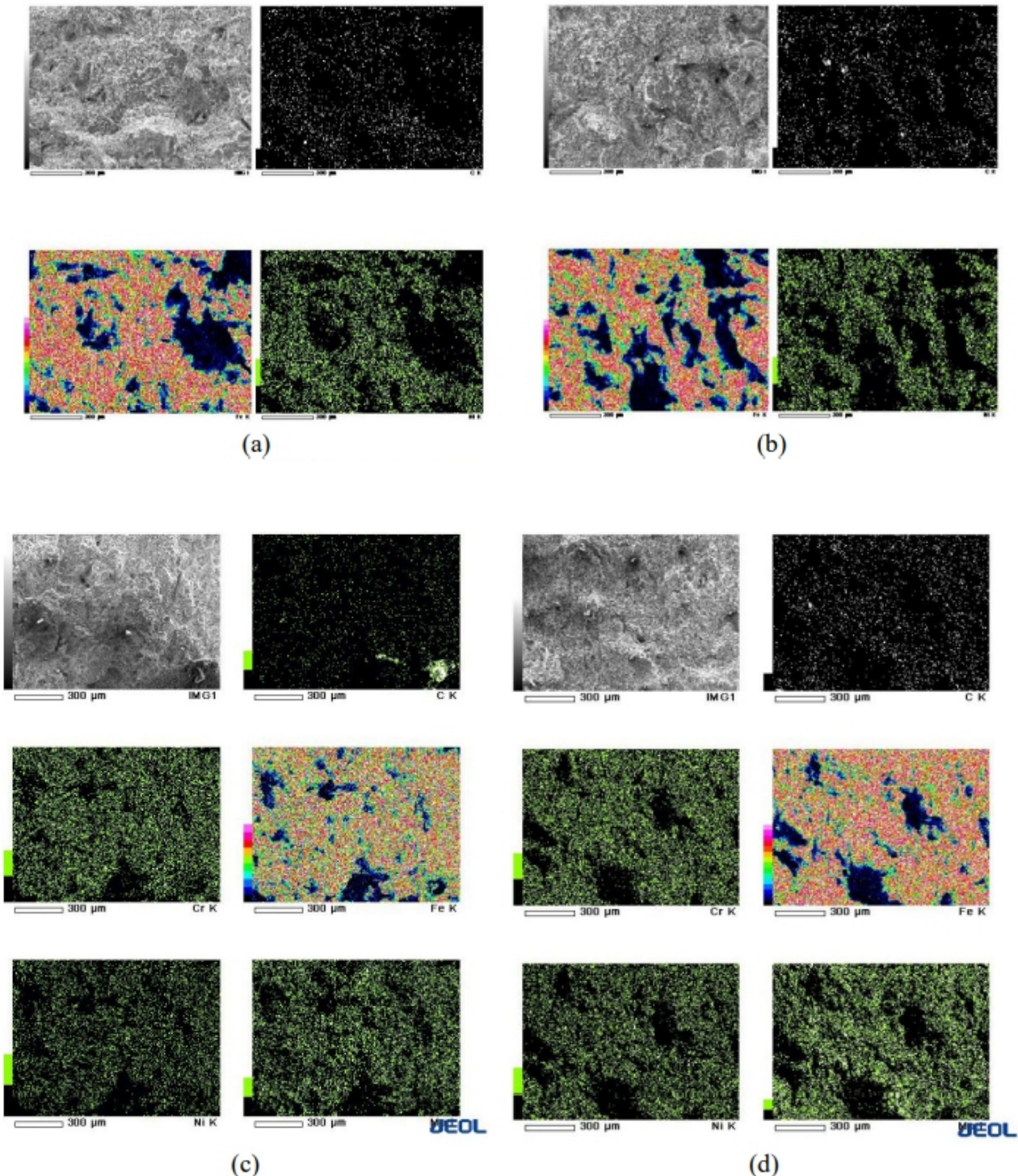


Figure 3. EDS Mapping of crack surfaces of (a) FeNiCrMo C10-3, (b) FeNiCrMo C60-3, (c) FeNiCrMo C10-4 and (d) FeNiCrMo C60-4.

3.3. Effect of Sub-zero treatment on microstructure experimental results

Figure 4a–f reveals the morphological structure of FeNiCrMo alloy with different times of cryogenic treatment using liquid nitrogen as the cooling medium, showing the existence of martensite (red arrows), ferrite (yellow arrows) and retained austenite (blue arrows). The cryogenic heat treatments contributed to the phase transformation, where the retained austenite was transformed into lath martensite. There was an increase in martensite amount with the rise in cryogenic time (10–360 min), which is caused by how long the austenitization process had taken [31]. The lath martensite was also transformed into the lath martensite tempered due to the tempering process after cryogenic treatment [32].

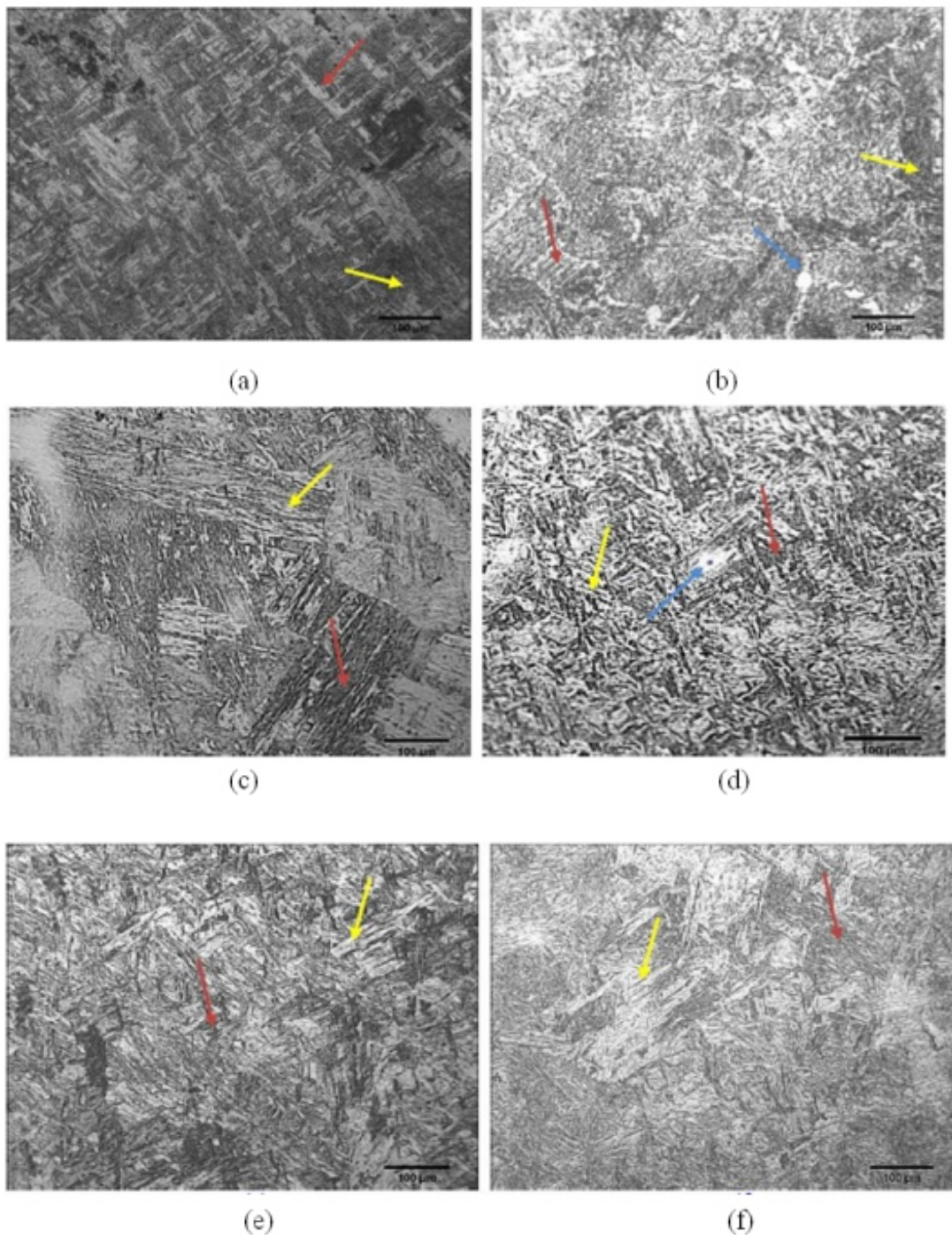


Figure 4. Microstructure of (a) FeNiCrMo C10-3, (b) FeNiCrMo C60-3, (c) FeNiCrMo C10-4, (d) FeNiCrMo C60-4, (e) FeNiCrMo C-360-3, (f) FeNiCrMo C-360-4.

Furthermore, it also can be seen that there was a gradual decrease in retained austenite in the FeNiCrMo specimens with the enhancement in soaking time [33]. The deep cryogenic treatment using nitrogen showed that the martensite formed soon after the cooling process and having the body-centered tetragonal crystal structure. After the tempering process was done, the body-centered tetragonal martensite was transformed into body-centered cubic martensite, which also affects its hardness [34].

3.4. Effect of Sub-zero treatment on corrosion test results

Open circuit potential (OCP) was an important factor in comprehending the material's tendency to corrode [35]. The more positive the value of open circuit potential is, the more difficult the material is to corrode [36]. Based on the Pourbaix diagram of the Fe-Cl system, the range potential for OCP in this study is in the formation of Fe²⁺ [37].

Figure 5a indicates the curve of open circuit potential of Fe-Ni-Cr-Mo specimens in 3.5% NaCl solution. The E_{ocp} values of FeNiCrMo-3 specimens are -585 mV for C10-3, -554 mV for C60-3 and -547 mV for C360-3. Furthermore, the E_{ocp} values of FeNiCrMo-4 specimens are -599 mV for C10-4, -567 mV for C60-4 and -505 mV for C360-4. The E_{ocp} value increases with the increasing of sub-zero treatment time. This phenomenon proves that the higher time of sub-zero treatment causes the specimens nobler than the lower time of sub-zero treatment [38]. The FeNiCrMo-4 specimens have a higher value of E_{ocp}, for the same time of sub-zero treatment, than FeNiCrMo-3. This phenomenon is caused by higher Cr and Mo content in FeNiCrMo-4 specimens, which affects the specimens' corrosion resistance. These results reveal that FeNiCrMo-4 specimens were less reactive than FeNiCrMo-3.

In this work, the electrochemical corrosion parameters such as corrosion potential (E_{corr}) and corrosion current densities (I_{corr}) were automatically obtained from Butler-Volmer and Tafel equations [39]. The next step of Tafel slope analysis and fitting of the polarization curves were analyzed using Echem analyst software to acquire the corrosion rate of Low alloy nickel steel. Figure 5b shows that the FeNiCrMo-4 specimens with 360 min of sub-zero treatment time manifest higher corrosion potential than FeNiCrMo-4 specimens with 10- and 60-minute sub-zero treatment time, as well as FeNiCrMo-3 specimens. It is also shown in Table 4 that the corrosion current decreases with the increase of sub-zero treatment time, suggesting that the sub-zero treatment time variation improves the corrosion behavior of the specimens [40]. The corrosion rate decreases as the sub-zero treatment time increases, indicating better corrosion resistance. The highest corrosion resistance is FeNiCrMo C360-4, worth 1.759 mpy, caused by the highest protective passive film due to its high content of Cr [16].

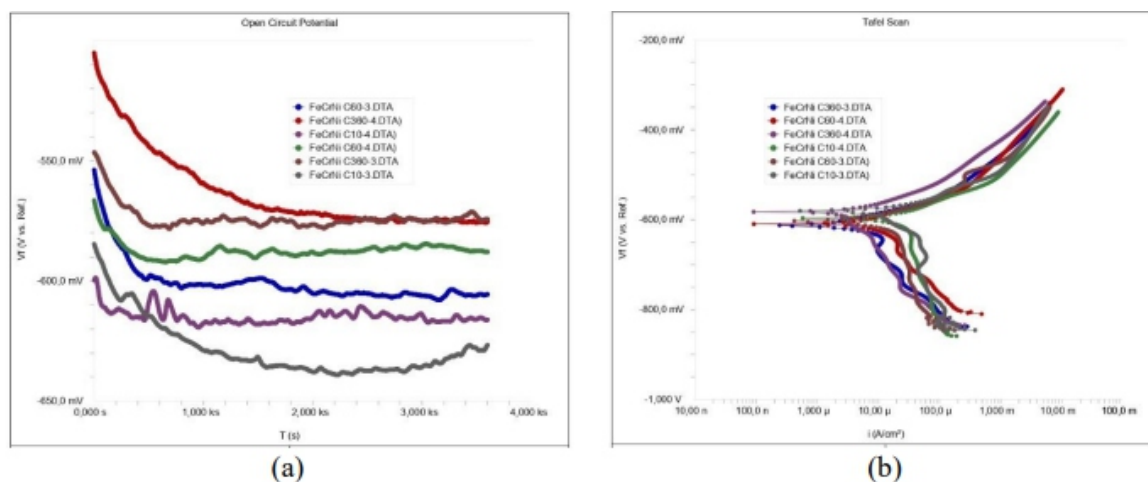


Figure 5. (a) Open circuit potential measurement, (b) Tafel polarization curve of low alloy nickel steel specimens in 3.5% NaCl solution.

Table 4. Electrochemical parameters obtained from Tafel polarization test of Fe-Ni-CrMo specimens in 3.5% NaCl solution.

Specimens	E _{corr} (mV)	I _{corr} ($\mu\text{A}/\text{cm}^2$)	Corr rate (mpy)
FeNiCrMo C10-3	-580.2	40.02	18.67
FeNiCrMo C10-4	-596.2	24.43	11.40
FeNiCrMo C60-3	-602.4	18.65	8.70
FeNiCrMo C60-4	-609.6	9.443	4.405
FeNiCrMo C360-3	-612.0	5.498	2.565
FeNiCrMo C360-4	-582.3	3.770	1.759

Figures 6a and 5b provide the cyclic polarization curves of low alloy nickel steel specimens in a 3.5% NaCl solution. All the FeNiCrMo-4 specimens in Figure 6b presented a substantial hysteresis loop between the forward and the reversed scans, which characterizes the material as generally susceptible to pitting corrosion [41]. Meanwhile, all the FeNiCrMo-3 specimens did not show a substantial hysteresis loop between the forward and reverse scans, which indicates no pitting corrosion is suspected. The E_{corr} values of FeNiCrMo-3 specimens are -820.9 mV for C10-3, -820.1 mV for C60-3 and -734.5 mV for C360-3. Furthermore, the E_{corr} values of FeNiCrMo-4 specimens are -834.5 mV for C10-4, -822.1 mV for C60-4 and -818.4 mV for C360-4.

As can be seen, the low alloy nickel steel with higher sub-zero treatment time has higher corrosion potential than low alloy nickel steel with lower sub-zero treatment time. This means that the corrosion resistance was improved with increasing sub-zero treatment time due to the microstructure of martensite and being free from retained austenite [42]. According to our previous work, the higher sub-zero treatment time eliminated retained austenite and achieved 98.617% of the martensite phase at 360 min of sub-zero treatment time [43]. Moreover, the value of repassivation potential in FeNiCrMo-4 specimens was shifted towards more noble potentials with the increasing sub-zero treatment time, which indicates the better resistance of the material to pit growth [12].

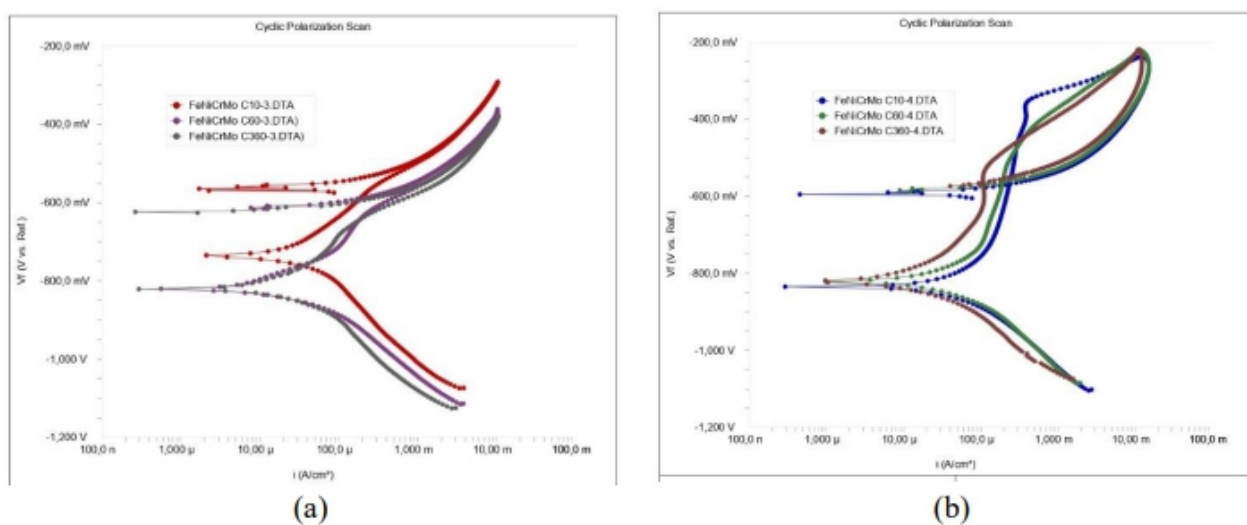


Figure 6. Cyclic polarization curves of (a) FeNiCrMo-3 specimens and (b) FeNiCrMo-4 specimens in 3.5% NaCl solution.

3.5. Effect of Sub-zero treatment on SEM-EDS of corrosion products in Fe-Ni-Cr-Mo specimens

Figure 7a–f shows all the surfaces were covered by ion complexes, indicating that all surface regions have similar corrosion behavior and experienced uniform corrosion. The corroded area decreases with the increase of sub-zero treatment time. The surface of FeNiCrMo-4 specimens exhibited some small individual pits where it seemed that the size increased and the number of pits decreased after the longer sub-zero treatment time [22]. This phenomenon is caused by the distribution element and the effect of cold temperature quenching immersion affecting the phase transformation and carbon in the specimens, increasing the pitting corrosion size.

The EDS spectra reveal the presence of oxygen, which proves the corrosion product in all low alloy nickel steel specimens. The FeNiCrMo C10-3 sample showed the highest percentage (15.9%) of oxygen. The oxidized displays the most exceptional tribological performance because to the synergistic chemical change and mechanical strengthening by O atoms [44]. While the lowest 8.77% of oxygen was revealed by the FeNiCrMo C360-3. It is also displayed that the surface of the uniform corrosion contains sodium and chloride, which relate to the surface exposure in the 3.5% NaCl corrosive medium. The matrix is fully covered by corrosion products, while the corrosion products layer is not uniform [12].

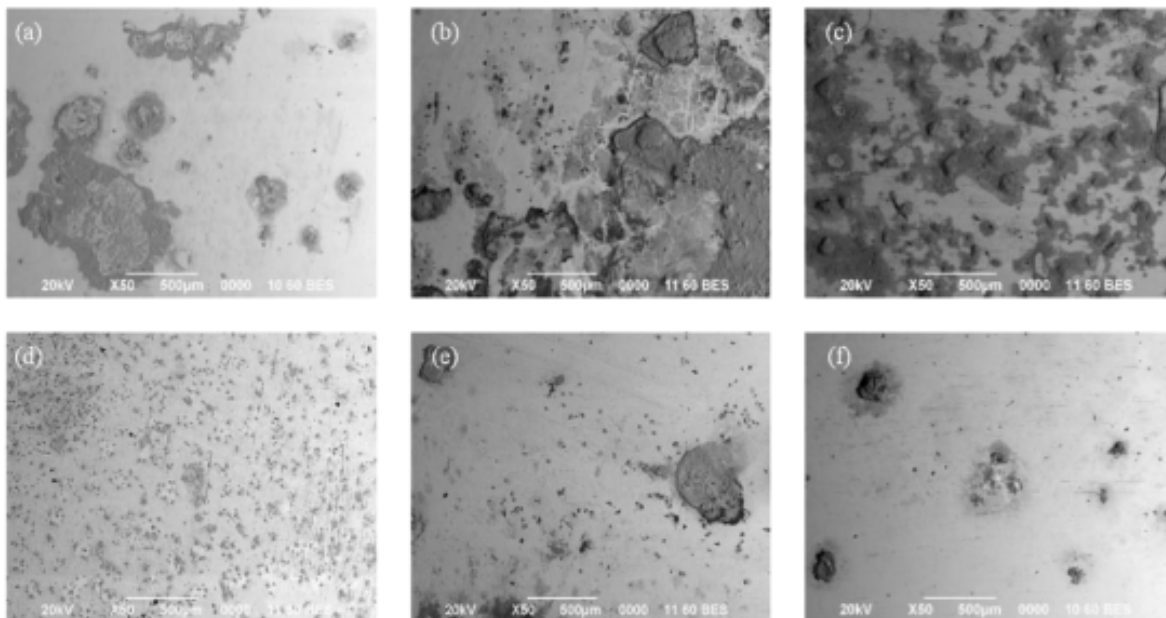
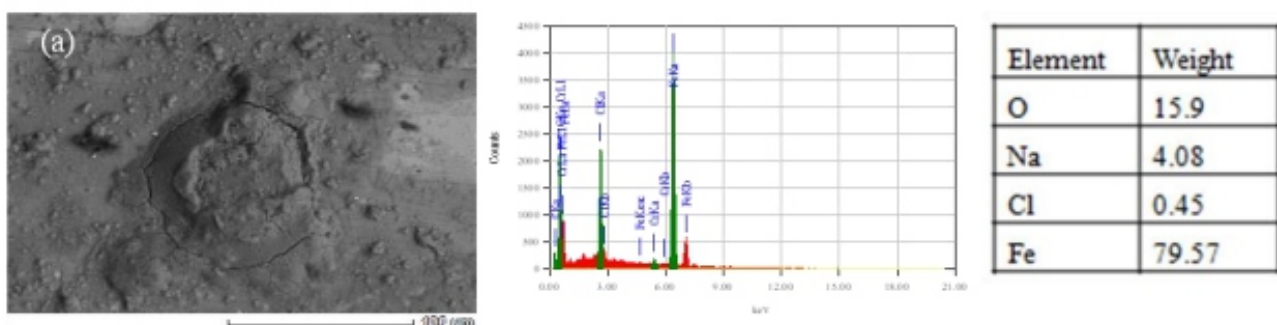


Figure 7. SEM images of (a) FeNiCrMo C10-3, (b) FeNiCrMo C60-3, (c) FeNiCrMo C360-3, (d) FeNiCrMo C10-4, (e) FeNiCrMo C60-4 and (f) FeNiCrMo C360-4 after immersing in 3.5% NaCl solution.



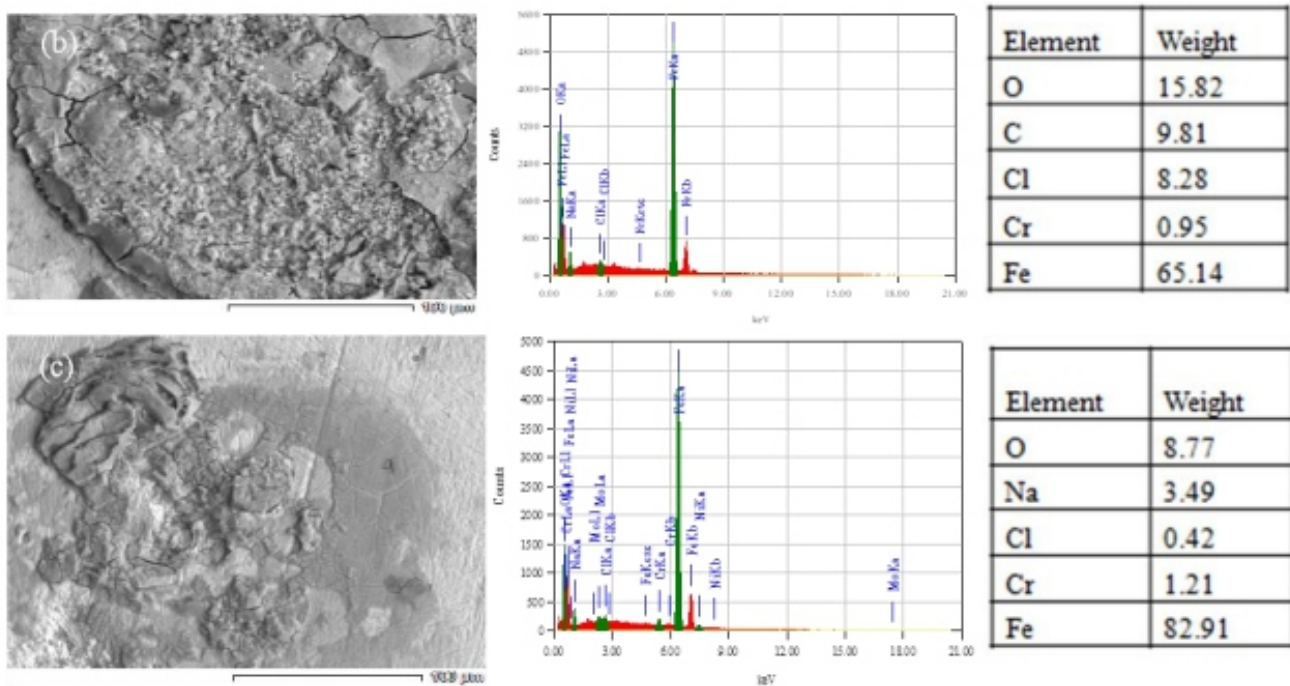


Figure 8. EDS results of FeNiCrMo (a) C10-3, (b) C60-3 and (c) C360-3 after immerse in 3.5% NaCl solution.

4. Conclusions

This study investigated the effects of sub-zero treatment on the hardness, fractography morphology and corrosion properties of low alloy nickel steel. The results confirm that the hardness characterization data using the Kolmogorov-Smirnov and Shapiro-Wilk normality tests were normally distributed, with a Sig value of (0.05), indicating that the FeNiCrMo-4 with 60 min of immersion time is the highest of all the specimens worth of 417.9 HV. The corrosion rate of low alloy nickel steel with a longer sub-zero treatment time is lower than low alloy nickel steel with a shorter sub-zero treatment period. This phenomenon suggests that increasing the sub-zero treatment period improves corrosion resistance. As the sub-zero treatment period increased, the corroded area decreased.

Acknowledgments

The authors would like to express their gratitude to the National Research and Innovation Agency of Indonesia for their financial support. The main contributors in this paper are Vinda Puspasari and Satrio Herbirowo.

Conflicts of interests

All authors declare no conflicts of interest in this paper.

References

1. Kartikasari R, Subardi A, Wijaya AE (2021) Development of Fe-5Al-1C alloys for grinding ball. *Eastern-European J Enterp Technol* 1: 29–35. <https://doi.org/10.15587/1729-4061.2021.225421>
2. Foszcz D, Krawczykowski D, Gawenda T, et al. (2018) Analysis of process of grinding efficiency in ball and rod mills with various feed parameters. *IOP Conf Ser-Mater Sci Eng* 427: 012031. <https://doi.org/10.1088/1757-899X/427/1/012031>
3. Jankovic A, Wills T, Dikmen S (2016) A comparison of wear rates of ball mill grinding media. *J Min Metall A Min* 52: 1–10. <https://doi.org/10.5937/JMMA1601001J>
4. Zurnadzhly VI, Efremenko VG, Wu KM, et al. (2020) Quenching and partitioning-based heat treatment for rolled grinding steel balls. *Metall Mater Trans A* 51: 3042–3053.

<https://doi.org/10.1007/s11661-020-05737-w>

5. Massola CP, Chaves AP, Albertin E (2016) A discussion on the measurement of grinding media wear. *J Mater Res Technol* 5: 282–288. <https://doi.org/10.1016/j.jmrt.2015.12.003>
6. Stalinskii DV, Rudyuk AS, Solenyi VK, et al. (2017) Improving the quality of steel grinding balls. *Steel Transl* 47: 130–136. <https://doi.org/10.3103/S0967091217020115>
7. Aissat S, Sadeddine A, Bradai MA, et al. (2017) Effect of heat treatment on the hardness and wear of grinding balls. *Met Sci Heat Treat* 59: 297–301. <https://doi.org/10.1007/s11041-017-0146-58>
- Chyla P, Pater Z, Tomczak J, et al. (2016) Numerical analysis of a rolling process for producing steel balls using helical rolls. *Arch Metall Mater* 61: 485–492. <https://doi.org/10.1515/amm20160085>
9. Hao Y, Li J, Li X, et al. (2020) Influences of cooling rates on solidification and segregation characteristics of Fe-Cr-Ni-Mo-N super austenitic stainless steel. *J Mater Process Technol* 275: 116236. <https://doi.org/10.1016/j.jmatprotec.2019.116326>
10. Zai L, You G, Tong X, et al. (2020) Microstructure and mechanical properties of inertia-friction welded Fe-Cr-Ni-Mo high-strength steel. *Steel Res Int* 91: 1–12. <https://doi.org/10.1002/srin.202000145>
11. Sabih A, Radziszewski P, Mullany I (2017) Investigating grinding media differences in microstructure, hardness, abrasion and fracture toughness. *Miner Eng* 103: 43–53. <https://doi.org/10.1016/j.mineng.2016.08.014>
12. Efremenko VG, Popov ES, Kuz'Min SO, et al. (2014) Introduction of three-stage thermal hardening technology for large diameter grinding balls. *Metallurgist* 57: 849–854. <https://doi.org/10.1007/s11015-014-9812-7>
13. Çolak SS, Altun O, Benzer H, et al. (2018) Development of a preliminary media wear measurement test procedure for cement ball milling applications. *Powder Technol* 325: 678–686. <https://doi.org/10.1016/j.powtec.2017.11.033>
14. Daraio D, Villoria J, Ingram A, et al. (2020) Investigating grinding media dynamics inside a vertical stirred mill using the discrete element method: Effect of impeller arm length. *Powder Technol* 364: 1049–1061. <https://doi.org/10.1016/j.powtec.2019.09.038>
15. Jang JW, Iwasaki I, Moore JJ (1989) Effect of galvanic interaction between martensite and ferrite grinding media wear. *Corrosion* 45: 402–407. <https://doi.org/10.5006/1.3582036>
16. Jurči P, Dománková M, Čaplovič L, et al. (2015) Microstructure and hardness of sub-zero treated and no tempered P/M Vanadis 6 ledeburitic tool steel. *Vacuum* 111: 92–101. <https://doi.org/10.1016/j.vacuum.2014.10.004>
17. Murthy BRN, Rangappa R (2021) Morphology and wear of high chromium and austempered ductile iron balls as grinding media in ball mills. *J Phys-Conf Ser* 2070: 012201. <https://doi.org/10.1088/1742-6596/2070/1/012201>
18. Das D, Ray KK (2012) Structure-property correlation of sub-zero treated AISI D2 steel. *Mater Sci Eng A-Struct* 541: 45–60. <https://doi.org/10.1016/j.msea.2012.01.130>
19. Sobotova J, Ku-Gik M, Krum S, et al. (2016) Effect of sub-zero treatment on the wear resistance of P/M tool steels. *J Appl Mech Eng* 5: 1000243.
20. Jurči P, Bartkowska A, Hudáková M, et al. (2021) Effect of sub-zero treatments and tempering on corrosion behaviour of vanadis 6 tool steel. *Materials* 14: 3759. <https://doi.org/10.3390/ma14133759>
21. Kosaraju S, Singh SK, Buddi T, et al. (2020) Evaluation and characterisation of ASS316L at sub-zero temperature. *Adv Mater Process Technol* 6: 445–455. <https://doi.org/10.1080/2374068X.2020.1728650>
22. Shah N, Arora K, Dhokey NB, et al. (2019) Studies on wear behaviour and DBTT in sub-zero regimes of cryo-treated high nitrogen martensitic stainless steel (HNMS). *Trans Indian Inst Met* 72: 2121–2126. <https://doi.org/10.1007/s12666-018-01555-2>
23. Zhou Q, Luo D, Hua D, et al. (2022) Design and characterization of metallic glass/graphene multilayer with excellent nanowear properties. *Friction* 10: 1913–1926. <https://doi.org/10.1007/s40544-021-0581-6>
24. Yan XG, Li DY (2013) Effects of the sub-zero treatment condition on microstructure, mechanical behavior and wear resistance of W9Mo3Cr4V high speed steel. *Wear* 302: 854–862.

<https://doi.org/10.1016/j.wear.2012.12.037>

25. Li DH, He WC, Zhang X, et al. (2021) Effects of traditional heat treatment and a novel deep cryogenic treatment on microstructure and mechanical properties of low-carbon high-alloy martensitic bearing steel. *J Iron Steel Res Int* 28: 370–382. <https://doi.org/10.1007/s42243-020-00527-5>
26. Szala M, Winiarski G, Wójcik Ł, et al. (2020) Effect of annealing time and temperature parameters on the microstructure, hardness, and strain-hardening coefficients of 42CrMo4 Steel. *Materials* 13: 1–16. <https://doi.org/10.3390/ma13092022>
27. Zhirafar S, Rezaeian A, Pugh M (2007) Effect of cryogenic treatment on the mechanical properties of 4340 steel. *J Mater Process Technol* 186: 298–303. <https://doi.org/10.1016/j.jmatprotec.2006.12.046>
28. Shamsolhodaei A, Oliveira JP, Schell N, et al. (2020) Controlling intermetallic compounds formation during laser welding of NiTi to 316L stainless steel. *Intermetallics* 116: 106656. <https://doi.org/10.1016/j.intermet.2019.106656>
29. Wang K, Gu K, Miao J, et al. (2019) Toughening optimization on a low carbon steel by a novel Quenching-Partitioning-Cryogenic-Tempering treatment. *Mater Sci Eng A-Struct* 743: 259–264. <https://doi.org/10.1016/j.msea.2018.04.104>
30. Akincioğlu S, Gökkaya H, Uygur I (2015) A review of cryogenic treatment on cutting tools. *Int J Adv Manuf Technol* 78: 1609–1627. <https://doi.org/10.1007/s00170-014-6755-x>
31. Gill SS, Singh J, Singh R, et al. (2012) Effect of cryogenic treatment on AISI M2 high speed steel: Metallurgical and mechanical characterization. *J Mater Eng Perform* 21: 1320–1326. <https://doi.org/10.1007/s11665-011-0032-z>
32. Wang LY, Wu YX, Sun WW, et al. (2020) Strain hardening behaviour of as-quenched and tempered martensite. *Acta Mater* 199: 613–632. <https://doi.org/10.1016/j.actamat.2020.08.067>
33. Patil PI, Tated RG (2012) Comparison of effects of cryogenic Treatment on different types of steels: A review. *International Conference in Computational Intelligence (ICCIA)* 9: 10–29.
34. Jovičević-Klug P, Jovičević-Klug M, Sever T, et al. (2021) Impact of steel type, composition and heat treatment parameters on effectiveness of deep cryogenic treatment. *J Mater Res Technol* 14: 1007–1020. <https://doi.org/10.1016/j.jmrt.2021.07.022>
35. Alqarni ND, Wysocka J, El-Bagoury N, et al. (2018) Effect of cobalt addition on the corrosion behavior of near equiatomic NiTi shape memory alloy in normal saline solution: Electrochemical and XPS studies. *RSC Adv* 8: 19289–19300. <https://doi.org/10.1039/C8RA02031K>
36. Wang XH, Zhong SY, Song YH, et al. (2020) Effect of tantalum film on corrosion behaviour of AA6061 aluminium alloy in hydrochloric acid- and chloride-containing solutions. *Trans Inst Met Finish* 98: 243–249. <https://doi.org/10.1080/00202967.2020.1802930>
37. Zhou X, Liao C, Wang Y, et al. (2021) Constructing the Pourbaix diagram of Fe-Cl–H₂O ternary system under supercritical water conditions. *Electrochim Acta* 377: 138075. <https://doi.org/10.1016/j.electacta.2021.138075>
38. Utomo EP, Herbirowo S, Puspasari V, et al. (2021) Characteristics and corrosion behavior of Ti 30Nb-5Sn alloys in histidine solution with various NaCl concentrations. *Int J Corros Scale Inhib* 10: 592–601. <https://doi.org/10.17675/2305-6894-2021-10-2-7>
39. Hu J, Zhu Y, Hang J, et al. (2021) The effect of organic core-shell corrosion inhibitors on corrosion performance of the reinforcement in simulated concrete pore solution. *Constr Build Mater* 267: 121011. <https://doi.org/10.1016/j.conbuildmat.2020.121011>
40. Li S, Xiao M, Ye G, et al. (2018) Effects of deep cryogenic treatment on microstructural evolution and alloy phases precipitation of a new low carbon martensitic stainless bearing steel during aging. *Mater Sci Eng A-Struct* 732: 167–177. <https://doi.org/10.1016/j.msea.2018.07.012>
41. Samuel AP, Arul S (2018) Effect of cryogenic treatment on the mechanical properties of low carbon steel IS 2062. *Mater Today Proc* 5: 25065–25074. <https://doi.org/10.1016/j.matpr.2018.10.307>
42. Liao J, Li L, Peng J, et al. (2020) Effects of deep cryogenic treatment on the microstructure and friction performance of M35 high-speed steel. *J Phys-Conf Ser* 1676: 012098. <https://doi.org/10.1088/1742-6596/1676/1/012098>

43. Sendya A, Marzuki H, Herbirowo S, et al. (2020) Study of Cr/Mo alloys lateritic steel with the soaking time cryogenic treatment on hardness, toughness, abrasive resistant, and microstructure. *Met Indones* 42: 21–27. <https://doi.org/10.32423/jmi.2020.v42.20-27>
44. Jia Q, He W, Hua D, et al. (2022) Effects of structure relaxation and surface oxidation on nanoscopic wear behaviors of metallic glass. *Acta Mater* 232: 117934. <https://doi.org/10.1016/j.actamat.2022.117934>

Increasing the charge/discharge rate for phase-change materials by forming hybrid composite paraffin/ash for an effective thermal energy storage system

Budhi Muliawan Suyitno*, Dwi Rahmalina and Reza Abdu Rahman
Department of Mechanical Engineering, Faculty of Engineering, Universitas
Pancasila, Srengseng Sawah, Jagakarsa 12640, DKI Jakarta, Indonesia

ABSTRACT

Low-temperature latent heat storage (LHS) systems are suitable for incorporating paraffin as the storage material. However, they face difficulty in actual implementation due to low thermal conductivity (TC). The present study used volcanic ash as an environmentally friendly and cost-effective material to increase the TC of paraffin. Three composites of paraffin/ash were prepared with ash proportions of 10 wt%, 30 wt% and 50 wt%. Characterizations were done to evaluate the average TC and properties. Thermal performance evaluation was conducted by analyzing the static charge/discharge cycle. The average TC for paraffin was 0.214 W/m·K. Adding volcanic ash improved the TC to 19.598 W/m·K. It made the charge/discharge performance of the composite better than that of pure paraffin. The charge rate for the composite ranged from 3.83 °C/min to 5.12 °C/min. The highest discharge rate was obtained at 4.21 °C/min for the composite paraffin50/ash50. The freezing temperature for the composite is influenced by the ash proportion, which can be taken as a suitable approach to adjust the freezing point of paraffin-based thermal energy storage (TES). The detailed results for the characterization and thermal performance evaluation are described thoroughly within the article. The overall result indicates that volcanic ash is applicable for improving the TC and charge/discharge rate of paraffin-based TES.

Keywords: ash; paraffin; phase change materials; thermal conductivity; thermal energy storage

1. Introduction

The risks of the energy crisis and global warming are motivating researchers across the globe to utilize alternative energy sources while simultaneously improving the reliability of renewable energy sources. Moreover, increasing the efficiency of the existing energy system is considered a suitable method to reduce the consumption of primary energy sources that still rely on fossil fuels [1]. Recent trends indicate that the deployment of solar and wind energy as renewable energy sources is increasing exponentially [2]. As a result, the annual global renewable energy production has increased rapidly in the last 10 years. Rapid growth in renewable energy deployment is related to the advanced development of energy storage systems, particularly for thermal energy storage (TES) [3]. TES is gaining momentum as an attractive method to store thermal energy. It can be implemented as a thermal substitution that reduces fossil fuel consumption indirectly for the heating/cooling sector. Continuous effort for optimization is still in progress, focusing on system improvement to provide more reliable and efficient thermal storage [4].

Sensible and latent heat storage are the two common methods for TES systems. Sensible heat storage utilizes the specific heat capacity of the storage material as the mechanism to store thermal energy. It is the most mature technology but suffers from low gravimetric and volumetric energy density [5]. Latent heat storage (LHS) uses a phase-change material (PCM) which stores the thermal energy based on its enthalpy of fusion. Thus, it can store sufficient thermal energy during the phase transition at a relatively small temperature gradient [6]. Furthermore, PCMs can be combined by using its specific heat capacity during the solid and liquid sensible stage, so they act as a sensible

material. Therefore, the storage capacity can be improved significantly based on the specific heat capacity at a given temperature operation and its enthalpy of fusion [7]. PCMs can be applied in active and passive thermal storage systems, making them suitable for various applications, such as residential heating/cooling and solar thermal systems [8].

Paraffin wax is the ideal candidate for a PCM for a low-temperature LHS system owing to its high enthalpy of fusion (approximately 180 kJ/kg) [9]. A PCM with a high enthalpy of fusion is desirable for LHS since it provides a higher storage capacity. The enthalpy of fusion is the key indicator for determining the storage capacity of the LHS system. The theoretical phase transition occurs at a constant temperature (isothermal phase transition), which makes the system absorb and release thermal energy isothermally [10]. Furthermore, paraffin is cheap, stable at room temperature and a non-corrosive substance. Low-temperature applications such as residential water heaters and thermal management systems are suitable for paraffin-based PCMs.

Two problems are related to the actual implementation of paraffin in LHS systems. The problems are related to the unstable phase transition [11] and low thermal conductivity [12]. Polymer can be used as a supporting matrix to promote the stable phase transition of paraffin. It can also maintain the long-term performance of the LHS system for up to 5000 charge/discharge cycles [13]. The next issue is related to low thermal conductivity. During the operation, the heat exchange process requires interaction between the paraffin and thermal source/load, which is highly dependent on thermal conductivity [14]. Low thermal conductivity decreases the heat transfer coefficient during the operation. As a result, the system operates at a slow charge/discharge cycle, which reduces the overall performance of the system substantially [15].

Two approaches can be taken to overcome the low thermal conductivity issue for paraffin-based PCMs. It can be done by promoting a better heat transfer rate based on the configuration of the storage container for paraffin-based PCMs. Yang et al. used modified fins inside the storage container. The charge rate of the finned container was 65% higher than that of the container without fins [16]. Waser et al. studied the combination of tube-in-shell and fin-based heat exchangers for the storage container [17]. It reduced the supercooling effect, which promotes a higher discharge rate. Bayomy et al. developed a storage container with a coil heat exchanger to accelerate the heat transfer process of paraffin-based TES. The proposed model increased the overall efficiency to 82% [18]. In general, using a suitable heat exchanger in the storage container minimizes the effect of low thermal conductivity. Kalapala and Devanuri confirmed that the heat transfer coefficient from the heat exchanger within the storage tank greatly influences the overall performance of an active LHS system [19].

A high thermal conductivity material can be used as an additive to develop a composite paraffin. The method is applicable for active and passive LHS systems. Deng et al. used a metal matrix to create a composite paraffin, proving that the melting/freezing processes increased by 93.9% and 95.9%, respectively [20]. Chen et al. utilized copper foams to improve the conductivity of a composite paraffin/polymer [21]. Qu et al. added 5-wt% carbon nanotubes to composite paraffin/high-density polyethylene (HDPE) and obtained an increment in the thermal conductivity of the composite of 60% [22]. Sheikholeslami et al. proposed a combined method to enhance the low thermal conductivity of paraffin-based PCMs. They used a fin-based container and composite paraffin with high thermal conductivity nanoparticles. It increased the heat transfer rate of the system substantially [23]. However, it is hard to implement the method for an integrated LHS system, particularly for a passive storage system for residential heating/cooling systems [11]. Furthermore, it leads to a significant challenge related to the mass production of paraffin-based PCMs as low-cost thermal storage material [24].

The thermal conductivity of paraffin can be improved by using a more sustainable and low-cost material such as volcanic ash. Volcanic ash is widely available, more economical, environmentally friendly and sustainable [25]. It consists of metallic and non-metallic minerals [26], which generally have better thermal conductivity than pure paraffin. It can be taken as a cost-effective material to improve the thermal conductivity in paraffin-based TES systems [27]. Considering the potential of volcanic ash to increase the thermal conductivity in paraffin-based TES systems, further characterization is required to understand the effect of volcanic ash in composite paraffin/volcanic

ash. Thus, the study aimed to examine the effects of volcanic ash of different weight proportions on the thermal performance of a paraffin-based TES system. Extensive characterization was conducted to evaluate the thermal conductivity, thermal properties and stability of the composite. The micrograph observation and infrared spectrum are presented as well in the study. Moreover, static charging/discharging test was also conducted to observe the charge/discharge cycles for the composite. The findings from the study are expected to be used as an essential reference for the further development of high thermal conductivity composite paraffin/volcanic ash as a sustainable and low-cost thermal conductivity enrichment material.

2. Materials and methods

2.1. Sample preparations

Commercial-grade paraffin wax (with an average melting temperature of 60 °C) was purchased from a local marketplace. We used volcanic ash with an average particle size of 74 µm. The main constituents of the volcanic ash were Fe (51.23%), Fe₂O₃ (23.24%) and SiO₂ (11%). The other composition and physical properties of the volcanic ash can be found in a previous report [27]. Four samples were prepared for characterization and static charging/discharging testing (Table 1). The mixing process for the composite was conducted by melting the paraffin using a thermal bath at a temperature of 90 °C. The ash was heated for 30 min in an electric oven at a temperature of 100 °C to remove the moisture. After that, the ash was added to the molten paraffin. The mixture was stirred slowly for half an hour. Then, rapid cooling was applied to the mixture to ensure that the ash dispersed properly within the solid composite. The total sample weight was 20 g for thermal evaluation through static charging/discharging testing.

2.2. Characterizations

Thermal conductivity measurement was conducted by using the hot disk method (TPS-3500). The test was repeated five times to estimate the average thermal conductivity for each sample. The enthalpy of fusion and melting and freezing temperatures were evaluated by using differential scanning calorimetry (DSC, MT + 1). The heating rate was set at 5 °C/min to minimize the effect of thermal inertia during the heating process. The decomposition curve for each sample was assessed by using thermogravimetric analysis (TGA). Fourier-transform infrared (FTIR) spectroscopy was applied to each sample to compare the functional group between the paraffin and composites of paraffin/ash. Then, the microstructures of the paraffin and the composites were evaluated by using scanning electron microscopy (SEM).

2.3. Charge/discharge cycle

Thermal performance evaluation was conducted to examine the charge/discharge rate of the prepared samples. Figure 1 presents the schematic design for static thermal performance evaluation. Each sample was tested individually. The sample was stored within the storage container (copper tube). The charge cycle was done by heating the storage container in an oil bath with an electric heater (Figure 1a). The charge cycle for TES is an endothermic process, meaning that the storage material is heated from an external source. Oppositely, the discharge cycle is an exothermic process, meaning that the stored heat in the storage material is released to the surroundings [28].

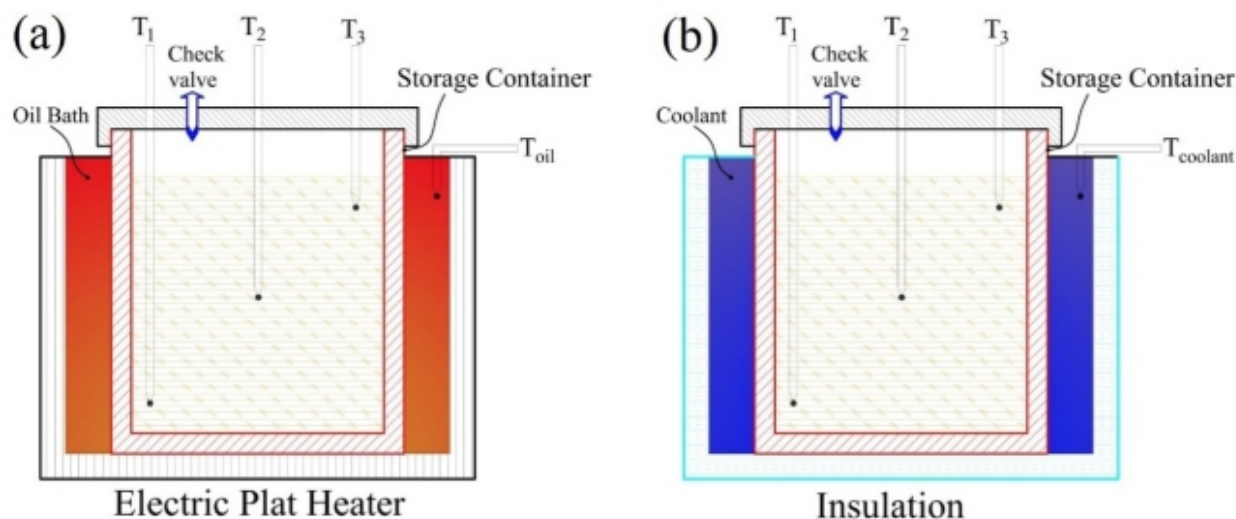


Figure 1. Schematic for charge cycle (a) and discharge cycle (b).

The composite paraffin/ash is intended for a passive LHS system. Thus, the charge cycle was limited to a temperature of 65 °C, which is slightly higher than the melting temperature of paraffin. The charge cycle was conducted by heating the sample using an electric hot plate. Once the sample reached the target temperature (65 °C), the storage container was moved to the cooling chamber for the discharge cycle (Figure 1b). The discharge cycle was conducted by using water as cooling media (with an initial temperature of 10 °C). Three thermocouples (Type K) were located within the storage container to record temperature changes during the charge/discharge cycle. The result of the charge/discharge cycle has been plotted by using a temperature-time graph to analyze the charge/discharge rate for each sample [29].

3. Results

3.1. DSC results

DSC provides sufficient information about the thermal properties of the prepared samples. It shows different heating/cooling curves, indicating the effect of the ash content within the composite (Figure 2). Paraffin yielded two endothermic peaks, indicating two crystallinity behaviors during the heating process. The first peak marks the solid-solid transition, which occurred around 40 °C. The second endothermic peak occurred at a temperature of 61.4 °C, representing the melting temperature of paraffin with an enthalpy of fusion of 188.7 J/g.

There was no substantial change in the heating curve for the composite paraffin90/ash10. The first and second peaks of the composite were relatively similar to those of pure paraffin. It had a melting temperature of 60.9 °C with an enthalpy of fusion of 179.2 J/g. Contrary to that, the heating curve was changed significantly for the composites with a higher ash content. As shown in Figure 2, the endothermic peak decreased for paraffin70/ash30 and paraffin50/ash50. The melting temperatures of both samples were 60.3 °C and 56.4 °C, respectively. The enthalpies of fusion of both samples were 175.6 J/g (paraffin70/ash30) and 158.5 J/g (paraffin50/ash50). The decrement in melting temperature made the sample easier to melt, which is advisable for specific applications.

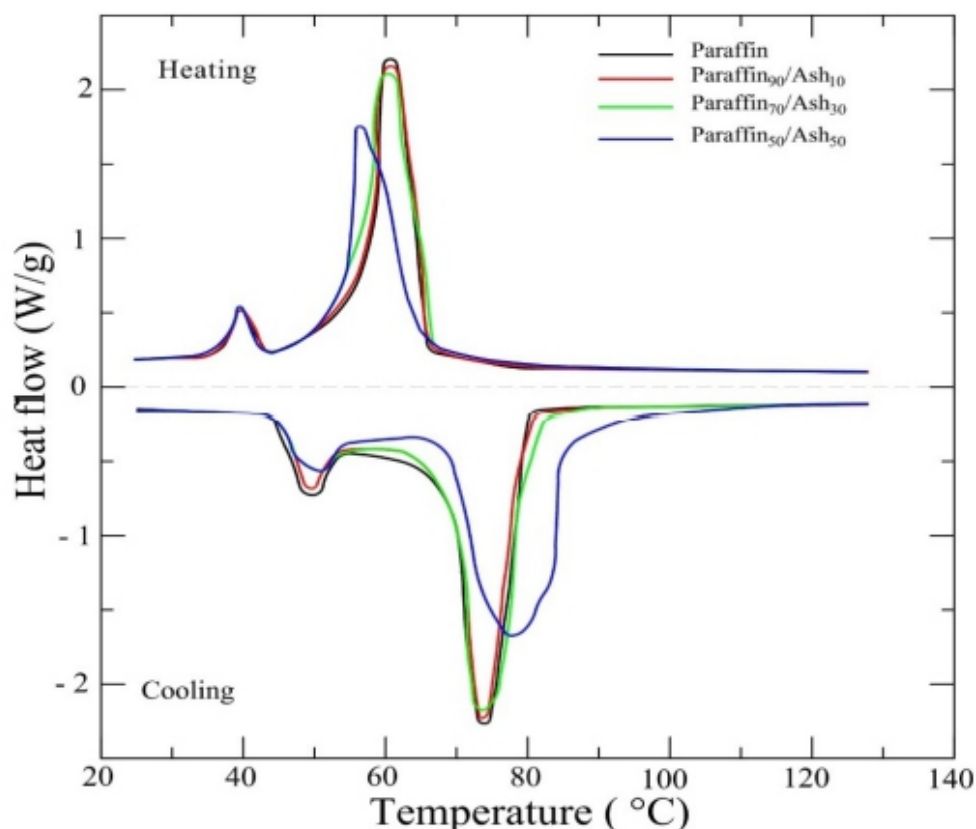


Figure 2. Heating and cooling curves for paraffin and composites of paraffin/ash.

The exothermic curve indicates the solidification process. The exothermic peak for the tested samples appeared at a higher temperature than the endothermic peak. The freezing temperature for paraffin was observed at 73.9 °C. In contrast, the freezing temperature shifted for the composites, dependent on the ash proportion. The freezing temperature for the composite with 10 wt% ash was 73.1 °C, which is lower than that of pure paraffin. Contrary to that, paraffin90/ash10 and paraffin70/ash30 had higher freezing temperatures of 74.2 °C and 78.5 °C, respectively. A higher freezing temperature is desirable for specific applications requiring rapid solidification during the discharge cycle, while a lower freezing temperature reduces the supercooling degree, which is desirable for temperature-sensitive LHS systems. Thus, adding a suitable ash proportion can be considered to adjust the freezing temperature of paraffin to meet the requirements of the LHS system.

3.2. TGA

Figure 3 presents the TGA curve for the tested samples. The decomposition curve determines the thermal stability of the sample during the heating process. As shown in Figure 3, the decomposition behavior of pure paraffin occurred as a single step decomposition. Rapid decomposition ran continuously from temperature 180 to 400 °C, with more than 90% of total mass loss. The thermal stability of paraffin is considerably low since it has a single-go decomposition at a relatively low temperature, which is undesirable for long-term cycles [30]. As compared to pure paraffin, the composites had different decomposition curves, implying the influence of the ash content within the sample.

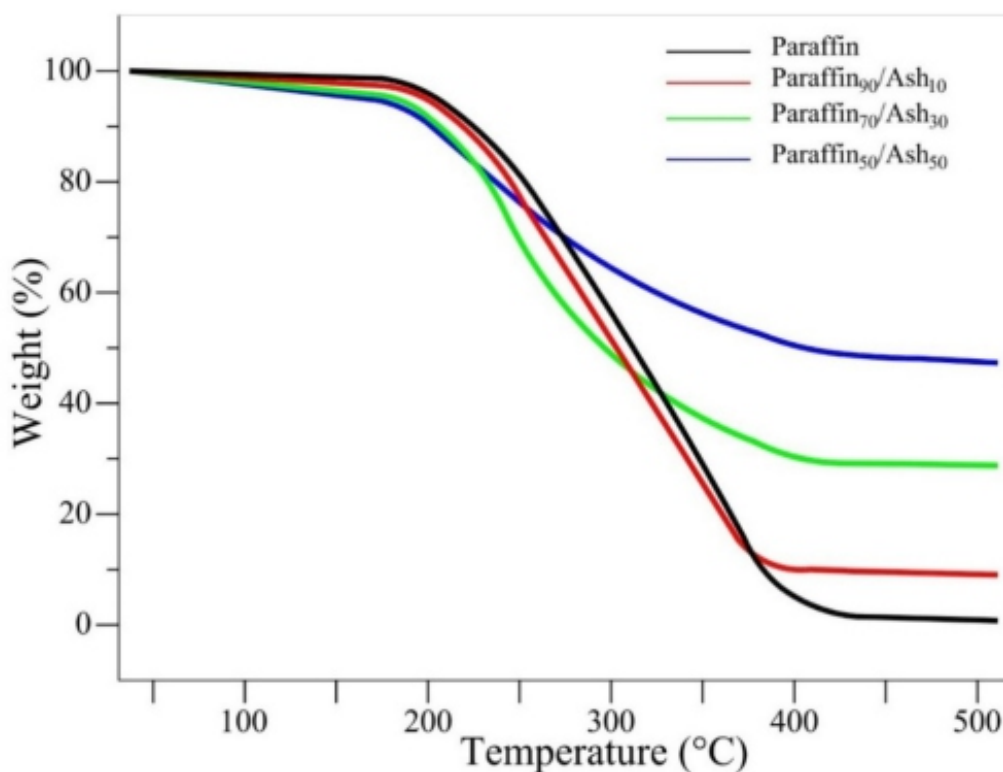


Figure 3. TGA plot for pure paraffin and composites of paraffin/ash.

The initial decomposition stage (<180 °C) of the paraffin/ash composites revealed significant mass loss, particularly with higher ash content. It implies the decomposition of the impurities and moisture content from the ash. It suggests that the preheating treatment should be done at a higher temperature to remove the impurities and moisture within the ash. Despite that, the composites had two-stage decomposition. It implies an immiscible blend between paraffin and ash. The paraffin was decomposed in the first place until the final decomposition temperature (approximately 400 °C) was reached. After that, no significant mass loss was observed since ash decomposes at a much higher temperature than pure paraffin.

3.3. Thermal conductivity

Figure 4 presents the average thermal conductivity of the tested samples. It shows that the thermal conductivity of paraffin is extremely low, with an average thermal conductivity of 0.214 W/m·K. It corresponds to a slow charge/discharge cycle. The average thermal conductivity of the composite paraffin/ash improved considerably. Adding 10 wt% ash increased the thermal conductivity to almost nine times that of pure paraffin. Volcanic ash is composed of various elements that generally have better thermal conductivity than paraffin. Thus, it increased the average thermal conductivity of paraffin effectively. Increasing the ash content of the composite led to a higher average thermal conductivity. However, the average thermal conductivity of the paraffin/ash composites was still much lower than the typical thermal conductivity enhancement. For instance, using copper nanoparticles increases the thermal conductivity of paraffin by up to 400 W/m·K [31].

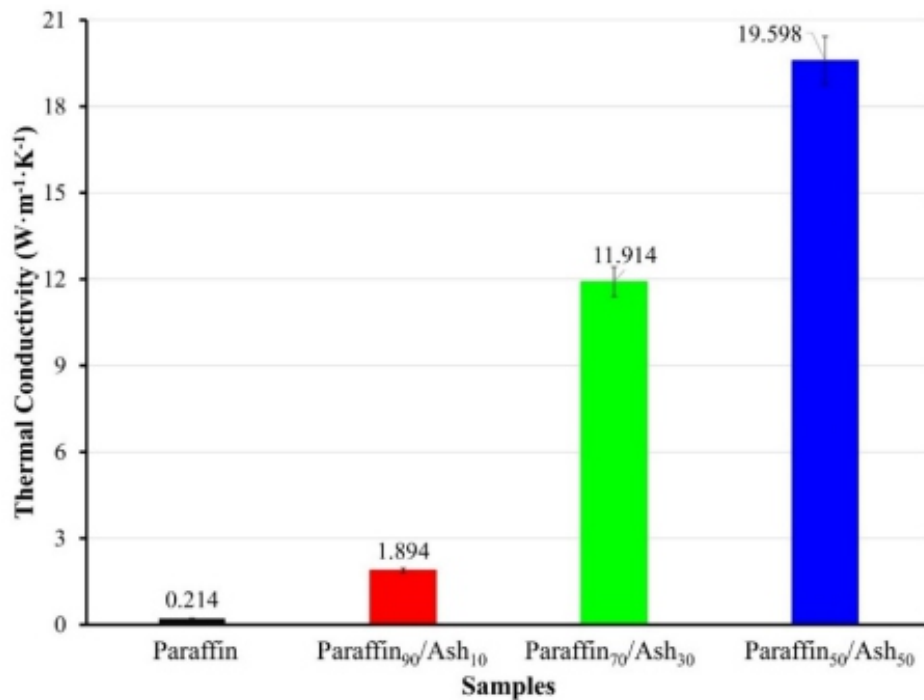


Figure 4. Average thermal conductivity of paraffin and composites of paraffin/ash.

3.4. Charge/discharge rate

The temperature-time profile for the charging stage is plotted in Figure 5. We used the average temperature from three thermocouples within the container (Figure 1). The phase transition region (indicated by the red dashed line) was accompanied by a slow temperature increment, which made the samples undergo a non-isothermal phase transition. The mushy region formation from the paraffin promoted a nonequilibrium heat transfer process. It increased the temperature slowly instead of indicating a plateau line during phase transition.

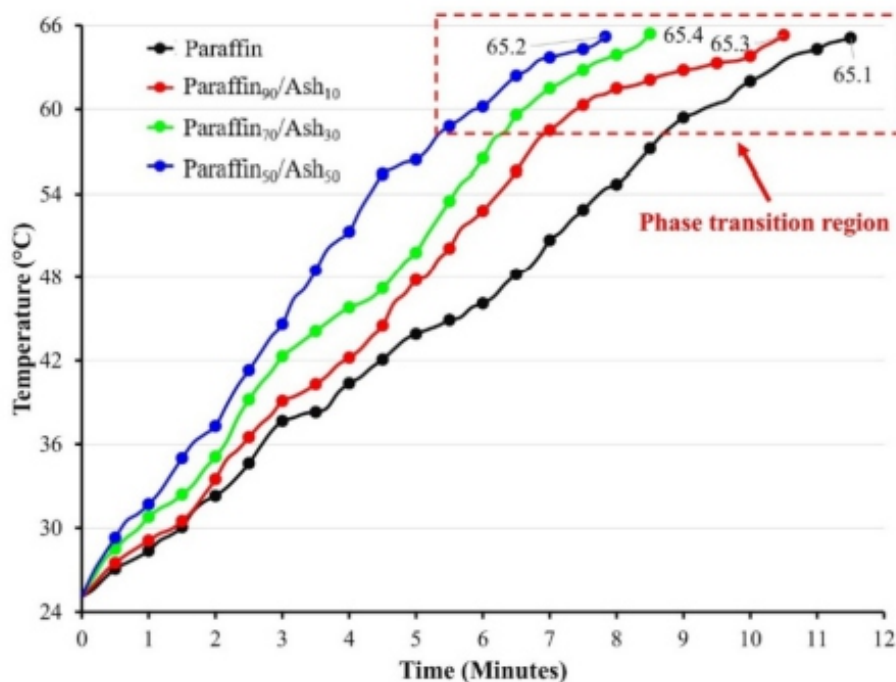


Figure 5. Temperature-time graph for charging stage for paraffin and composites of paraffin/ash.

Paraffin had the longest duration to reach the targeted temperature. Thus, it had the lowest charge rate compared to the composites of paraffin/ash. It emphasizes the effect of low thermal conductivity, which increased the duration of charge/discharge cycles during the operation. Adding ash to the paraffin directly contributed to the acceleration of the charge stage. As the thermal conductivity was enhanced, the heat transfer occurred rapidly, facilitating a better thermal distribution within the composite. Interestingly, there was a remarkable change in the temperature increment for each composite after passing the melting temperature. The temperature increment of paraffin90/ash10 was slower in the phase transition region. It implies that the effect of mushy region formation for the composite is still more noticeable than the composites with higher ash contents (paraffin70/ash30 and paraffin50/ash50). The composites paraffin70/ash30 and paraffin50/ash50 showed a steady temperature increment in the phase transition. Thus, the effect of mushy region formation can be minimized with more ash content within the composite.

The temperature increment before entering the phase transition (solid-sensible region) also accelerated distinctively. For instance, pure paraffin took 8.8 min to reach a temperature of 60 °C, while paraffin90/ash10 took a shorter duration, with only 7.3 min. A faster temperature increment in the solid-sensible region accelerated the composite to reach the phase transition region, where the most thermal energy is stored. The composite paraffin50/ash50 showed the highest charge rate, particularly during the solid-sensible stage. A higher ash content reduced the melting temperature of paraffin (Figure 2) and improved the average thermal conductivity (Figure 4). Thus, it made the charge performance of paraffin50/ash50 desirable for the operation of the LHS system.

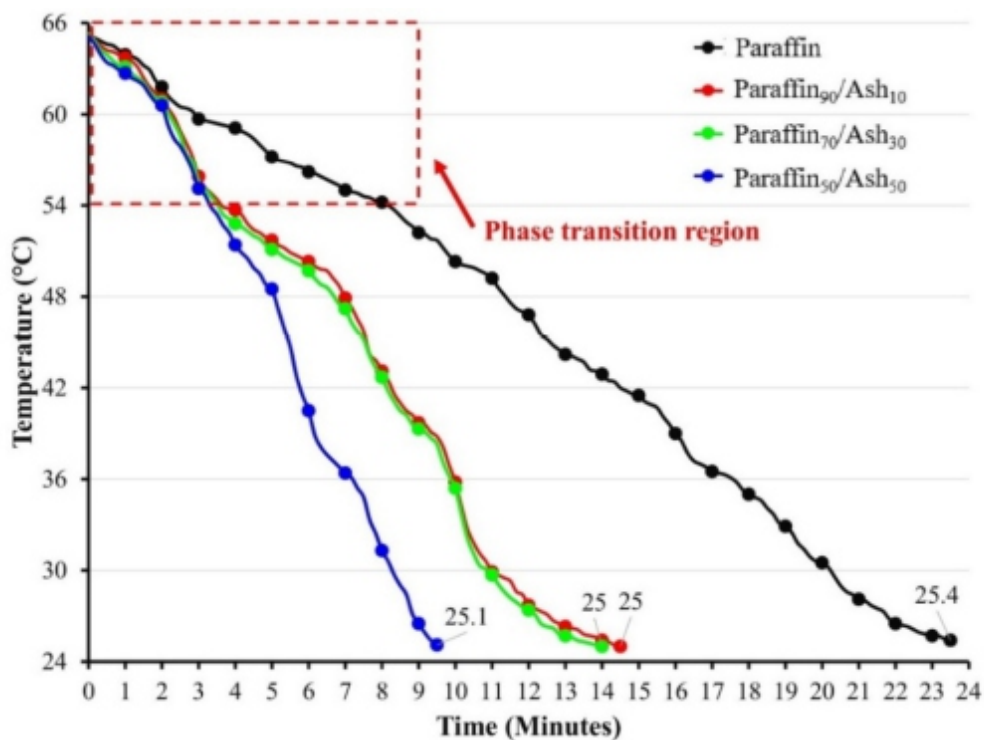


Figure 6. Temperature-time graph for discharging stage for paraffin and composites of paraffin/ash.

The discharge profile is shown in Figure 6. The heat release process for an LHS system is much slower than the charging process due to the supercooling effect [32]. Thus, the temperature decrement during the discharging process is relatively slow. For example, paraffin took almost twice as long as the charge duration to release the stored thermal energy. It is troublesome for the actual system because it indicates a low power rate. Furthermore, mushy region formation severely affects solidification, disrupting the heat transfer process [33]. It can be observed noticeably in the phase transition region with an average temperature decrement of 1.36 °C/min. The average temperature decrement during the solid-sensible stage was slightly higher, with a discharge rate of 1.88 °C/min.

The negative impact of mushy region formation during the discharging process can be reduced by adding volcanic ash to the paraffin. It can be seen that all paraffin/ash composites had a better discharge rate in the phase transition region. The composites took approximately 4 min to reach the end stage of the solidification process. It shows the positive impact of adding volcanic ash to the paraffin, where partial phase change can be minimized. The average discharge rate for the composites with ash contents of 10 wt% and 30 wt% were 2.67 °C and 2.77 °C/min, respectively. The cooling curves for both samples (Figure 2) also show similar freezing temperatures between 73.1–74.2 °C. Therefore, the discharge characteristics for both samples were relatively similar, with sufficient heat release during the phase transition and solid-sensible stage.

Paraffin50/ash50 obtained the most outstanding performance since it had the highest discharge rate. The total discharge duration for paraffin50/ash50 was 9.5 min, which is slightly longer than the charge duration. Using a higher ash proportion promoted a better temperature distribution. Thus, the decrement during the discharge stage could be minimized. The DSC results (Figure 2) imply the same phenomenon, since paraffin50/ash50 had the highest deviation between melting and freezing temperatures. It corresponds to the high thermal conductivity of the composite paraffin50/ash50, promoting an exceptional charge/discharge rate.

3.5. FTIR spectra

The FTIR spectra for pure paraffin and composite paraffin/ash are plotted in Figure 7. There was no substantial change in the paraffin/ash composites relative to pure paraffin. Peak absorption mainly occurred between 2900–2800 cm^{-1} , demonstrating the stretching vibration for main functional CH_2 . The next peak can be observed between 1500–1400 cm^{-1} , indicating the rocking vibration for the main functional groups $-\text{CH}_2$ and $-\text{CH}_3$. The last peak occurred around 800–700 cm^{-1} , and it is defined as rocking vibration for the main functional group of $-\text{CH}_2$. The paraffin/ash composites had spectra that were similar to that of pure paraffin. Thus, the composite was bound physically without forming any new chemical formation. Hence, the charge/discharge rate was improved by adding volcanic ash to the paraffin without altering the chemical properties of the paraffin.

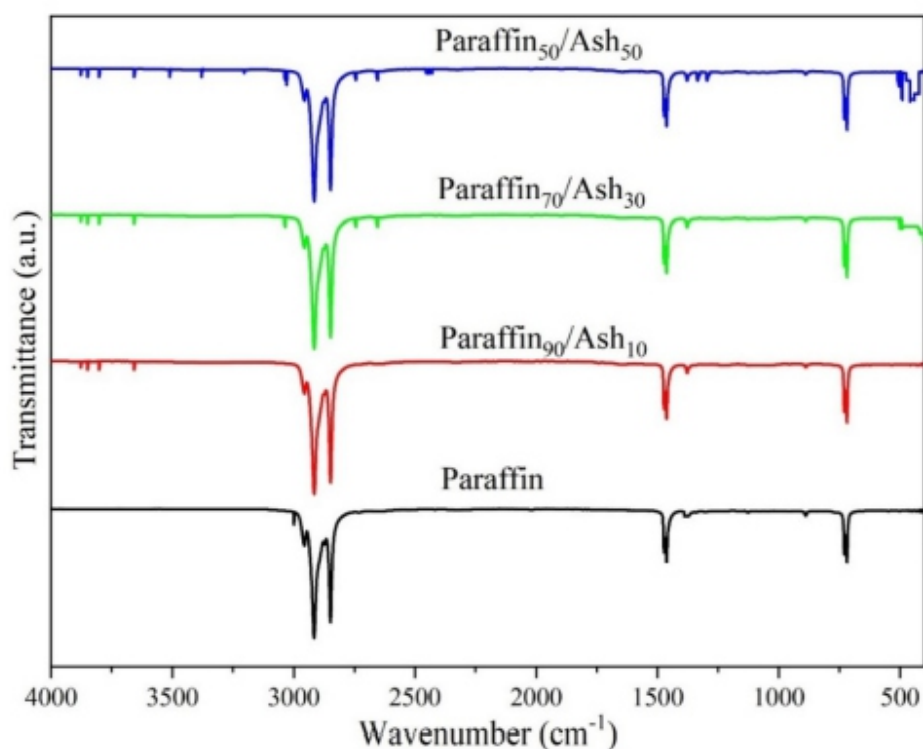


Figure 7. FTIR spectra for paraffin and composites of paraffin/ash.

3.6. SEM

Morphological observation was conducted by applying SEM to the tested samples. The SEM image was taken after thermal evaluation of the charge/discharge cycle. We intended to understand the dispersion of ash within the composite after the melting/freezing process for the actual application. Therefore, the captured images were specifically purposed to observe different morphologies which occurred within the composites of paraffin/ash. Figure 8a shows the corrugated paraffin surface affected by the melting/freezing cycle. It corresponds to the low molecular weight of paraffin and the slow freezing process, which transforms its shape after solidification. It affects the interaction between paraffin and volcanic ash, which can be seen as an immiscible blend. It confirms the TGA curve (Figure 3), which implies that the paraffin and ash melted at different rates and temperatures. Figure 8b shows local agglomeration of the ash content within the composite. It was affected by the melting process of paraffin, which altered the ash content distribution. Since the composite paraffin90/ash10 had the lowest ash content, the solidification process caused the ash particles to agglomerate locally with the contiguous ash particles. As a result, ash agglomerated as a single cluster and formed several individual clusters (indicated by the red circle). A different ash distribution can be observed in Figure 8c. It shows that the ash dispersed moderately in the paraffin since it had a higher ash content. However, the ash particles accumulated (the green circle). The volcanic ash had a higher density than paraffin, making the particles move downward in the molten paraffin. During the freezing process, the agglomerated ash settled closely, causing local accumulation. The effect of the immiscible blend between paraffin and ash is shown in Figure 8d. It shows that a void formed around the outer layer of the ash particle (the blue circle). The void between the ash and paraffin was worsened by rapid solidification in the case of the composite paraffin50/ash50 (Figure 6). It confirms the significant change in the thermal properties of the composite paraffin50/ash50 (Figure 2), particularly for the melting/freezing temperature; this highly corresponds to the void formation between the paraffin and ash particles.

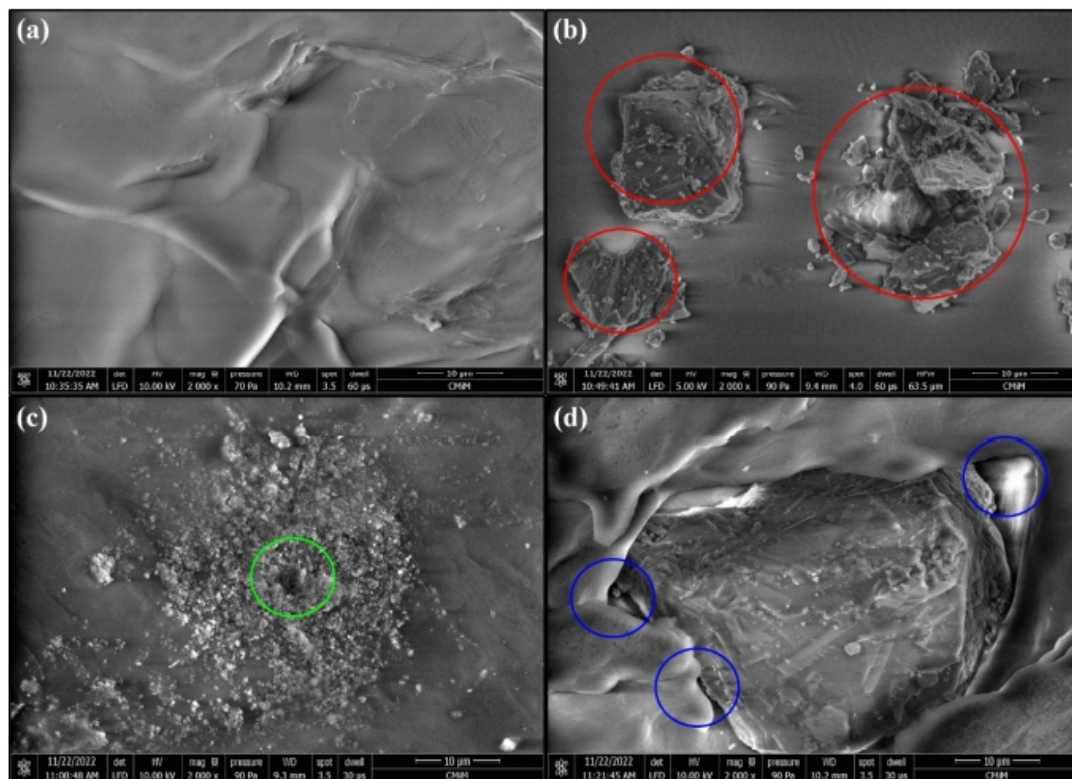


Figure 8. SEM micrographs of paraffin (a), paraffin90/ash10 (b), paraffin70/ash30 (c) and paraffin50/ash50 (d).

The charge/discharge rate for the paraffin/ash composite was higher than that for pure paraffin. However, sedimentation occurred for the paraffin/ash composites after 20 thermal cycles. It is an inevitable effect since volcanic ash is heavier than paraffin. The sedimentation could be minimized by using a supporting matrix such as HDPE, which works as a shape stabilizer during the phase transition of paraffin. Also, fast-charging operation causes thermal stress and hysteresis losses, potentially reducing the long-term performance of the PCM [34]. Besides its use as a shape stabilizer, HDPE also reduces the thermal stress and hysteresis losses for fast-charging paraffin-based PCM [35]. Thus, the proposed method can be further evaluated to avoid the sedimentation and extended cycling test to evaluate the long-term operation of composites of paraffin/volcanic ash as a fast-charging LHS material.

4. Conclusion

This work examined the potential of using volcanic ash as a thermal conductivity enhancement material for paraffin-based TES. The general results indicate that adding volcanic ash to form a paraffin/ash composite significantly improves the overall thermal conductivity. It leads to a better charge/discharge cycle. The highest discharge rate was 4.21 °C/min, which is much higher than that for pure paraffin, with only 1.69 °C/min. The composites of paraffin/ash had an immiscible blend that led to the FTIR spectra indicating no chemical change between the mixture. Improvement in the thermal conductivity and charge/discharge rate is correlated with the proportion of ash content within the composite. The highest thermal conductivity was 19.598 W/m·K for the composite paraffin50/ash50, which had the highest charge/discharge rate.

The addition of volcanic ash to form a composite of paraffin/ash decreased the total enthalpy of fusion. It can be considered the main drawback of adding a sensible material for thermal conductivity enhancement. The decrement in the enthalpy of fusion ranged from 5% to 16%, where the lowest decrement was obtained by paraffin50/50. Furthermore, the immiscible blend led to phase segregation and local agglomeration, which may alter the long-term performance of the composite. Despite that, improving the charge/discharge rate and thermal conductivity by adding volcanic ash can be considered as an alternative approach for increasing the performance of paraffin-based PCM. Therefore, further research is suggested to minimize the drawbacks of the volcanic ash within the composite. It can be done by using alternative binder materials such as polymers and PCMs with a higher enthalpy of fusion to maintain a suitable thermal capacity of the composite PCM and volcanic ash.

Acknowledgments

The authors would like to thank Andika Dedi Novi Prasetyo and Adimas Aziz Tasmin for supporting the study.

Conflict of Interest

The authors declare that they have no known competing financial interests or personal relationships that could have appeared to influence the work reported in this paper.

References

1. Ismail I, Mulyanto AT, Rahman RA (2022) Development of free water knock-out tank by using internal heat exchanger for heavy crude oil. *EUREKA: Phys Eng* 77–85. <https://doi.org/10.21303/2461-4262.2022.002502>
2. Ismail I, Rahman RA, Haryanto G, et al. (2021) The optimal pitch distance for maximizing the power ratio for savonius turbine on inline configuration. *IJRER* 11: 595–599.
3. International Renewable Energy Agency (IRENA), *Innovation outlook: Thermal energy storage, 2020*. Available from: <https://www.irena.org/Publications/2020/Nov/Innovation-outlook-Thermal-energy-storage>.
4. Ataei A (2016) Performance optimization of a combined solar collector, geothermal heat pump and thermal seasonal storage system for heating and cooling greenhouses. *J Appl Eng Sci* 14: 296–305. <https://doi.org/10.5937/jaes14-8749>

5. Sadeghi G (2022) *Energy storage on demand: Thermal energy storage development, materials, design, and integration challenges*. *Energy Storage Mater* 46: 192-222.
<https://doi.org/10.1016/j.ensm.2022.01.017>
6. Elbahjaoui R, El Qarnia H (2019) *Performance evaluation of a solar thermal energy storage system using nanoparticle-enhanced phase change material*. *Int J Hydrogen Energ* 44: 2013-2028.
<https://doi.org/10.1016/j.ijhydene.2018.11.116>
7. Palacios A, Navarro ME, Barreneche C, et al. (2020) *Hybrid 3 in 1 thermal energy storage system-Outlook for a novel storage strategy*. *Appl Energ* 274: 115024.
<https://doi.org/10.1016/j.apenergy.2020.115024>
8. Dsilva Winfred Rufuss D, Rajkumar V, Suganthi L, et al. (2019) *Studies on latent heat energy storage (LHES) materials for solar desalination application-focus on material properties, prioritization, selection and future research potential*. *Sol Energ Mat Sol C* 189: 149–165.
<https://doi.org/10.1016/j.solmat.2018.09.031>
9. Yadav C, Sahoo RR (2019) *Exergy and energy comparison of organic phase change materials based thermal energy storage system integrated with engine exhaust*. *J Energy Storage* 24: 100773.
<https://doi.org/10.1016/j.est.2019.100773>
10. Rahmalina D, Rahman RA, Ismail I (2022) *Improving the phase transition characteristic and latent heat storage efficiency by forming polymer-based shape-stabilized PCM for active latent storage system*. *Case Stud Therm Eng* 101840. <https://doi.org/10.1016/j.csite.2022.101840>
11. Gandhi M, Kumar A, Elangovan R, et al. (2020) *A review on shape-stabilized phase change materials for latent energy storage in buildings*. *Sustainability (Switzerland)* 12: 1–17.
<https://doi.org/10.3390/su12229481>
12. Wu S, Yan T, Kuai Z, et al. (2020) *Thermal conductivity enhancement on phase change materials for thermal energy storage: A review*. *Energy Storage Mater* 25: 251–295.
<https://doi.org/10.1016/j.ensm.2019.10.010>
13. Rahmalina D, Rahman RA, Ismail (2022) *Increasing the rating performance of paraffin up to 5000 cycles for active latent heat storage by adding high-density polyethylene to form shape-stabilized phase change material*. *J Energy Storage* 46: 103762.
<https://doi.org/10.1016/j.est.2021.103762>
14. Ma X, Sheikholeslami M, Jafaryar M, et al. (2020) *Solidification inside a clean energy storage unit utilizing phase change material with copper oxide nanoparticles*. *J Cleaner Production* 245: 118888. <https://doi.org/10.1016/j.jclepro.2019.118888>
15. Zhang YP, Lin KP, Yang R, et al. (2006) *Preparation, thermal performance and application of shape-stabilized PCM in energy efficient buildings*. *Energ Buildings* 38: 1262–1269.
<https://doi.org/10.1016/j.enbuild.2006.02.009>
16. Yang X, Lu Z, Bai Q, et al. (2017) *Thermal performance of a shell-and-tube latent heat thermal energy storage unit: Role of annular fins*. *Appl Energ* 202: 558–570.
<https://doi.org/10.1016/j.apenergy.2017.05.007>
17. Waser R, Maranda S, Stamatiou A, et al. (2020) *Modeling of solidification including supercooling effects in a fin-tube heat exchanger based latent heat storage*. *Sol Energy* 200: 10–21.
<https://doi.org/10.1016/j.solener.2018.12.020>
18. Bayomy A, Davies S, Saghier Z (2019) *Domestic hot water storage tank utilizing phase change materials (PCMs): Numerical approach*. *Energies* 12: 2170. <https://doi.org/10.3390/en12112170>
19. Kalapala L, Devanuri JK (2018) *Influence of operational and design parameters on the performance of a PCM based heat exchanger for thermal energy storage—A review*. *J Energy Storage* 20: 497–519. <https://doi.org/10.1016/j.est.2018.10.024>
20. Deng Z, Li J, Zhang X, et al. (2020) *Melting intensification in a horizontal latent heat storage (LHS) system using a paraffin/fractal metal matrices composite*. *J Energy Storage* 32: 101857.
<https://doi.org/10.1016/j.est.2020.101857>
21. Chen P, Gao X, Wang Y, et al. (2016) *Metal foam embedded in SEBS/paraffin/HDPE form-stable PCMs for thermal energy storage*. *Sol Energ Mater Sol C* 149: 60–65.
<https://doi.org/10.1016/j.solmat.2015.12.041>
22. Qu Y, Wang S, Zhou D, et al. (2020) *Experimental study on thermal conductivity of paraffin-*

- based shape-stabilized phase change material with hybrid carbon nano-additives. *Renew Energ* 146: 2637–2645. <https://doi.org/10.1016/j.renene.2019.08.098>
23. Sheikholeslami M, Haq R ul, Shafee A, et al. (2019) Heat transfer simulation of heat storage unit with nanoparticles and fins through a heat exchanger. *Int J Heat Mass Tran* 135: 470–478. <https://doi.org/10.1016/j.ijheatmasstransfer.2019.02.003>
24. Sciacovelli A, Navarro ME, Jin Y, et al. (2018) High density polyethylene (HDPE)-Graphite composite manufactured by extrusion: A novel way to fabricate phase change materials for thermal energy storage. *Particuology* 40: 131–140. <https://doi.org/10.1016/j.partic.2017.11.011>
25. Játiva A, Ruales E, Etxeberria M (2021) Volcanic ash as a sustainable binder material: An extensive review. *Materials* 14: 1–32. <https://doi.org/10.3390/ma14051302>
26. Kuznetsova E (2017) Thermal conductivity and the unfrozen water contents of volcanic ash deposits in cold climate conditions: A review. *Clays Clay Miner* 65: 168–183. <https://doi.org/10.1346/CCMN.2017.064057>
27. Rahmalina D, Adhitya DC, Rahman RA, et al. (2022) Improvement the performance of composite Pcm paraffin-based incorporate with volcanic ash as heat storage for low-temperature. *EUREKA-Phys Eng* 3–11. <https://doi.org/10.21303/2461-4262.2022.002055>
28. International Energy Agency Technology Collaboration Programme, *Applications of thermal energy storage in the energy transition*, 2018. Available from: <https://iea-es.org/wp-content/uploads/public/86.3.3-IEA-ECES-Annex-30-Final-Report.pdf>.
29. Yinping Z, Yi J (1999) A simple method, the T-history method, of determining the heat of fusion, specific heat and thermal conductivity of phase-change materials. *Meas Sci Technol* 201–205. <https://doi.org/10.1088/0957-0233/10/3/015>
30. Trisnadewi T, Kusriani E, Nurjaya DM, et al. (2021) Experimental analysis of natural wax as phase change material by thermal cycling test using thermoelectric system. *J Energy Storage* 40: 102703. <https://doi.org/10.1016/j.est.2021.102703>
31. Eanest Jebasingh B, Valan Arasu A (2020) A comprehensive review on latent heat and thermal conductivity of nanoparticle dispersed phase change material for low-temperature applications. *Energy Storage Mater* 24: 52–74. <https://doi.org/10.1016/j.ensm.2019.07.031>
32. Shamseddine I, Pennec F, Biwolle P, et al. (2022) Supercooling of phase change materials: A review. *Renew Sust Energ Rev* 158: 112172. <https://doi.org/10.1016/j.rser.2022.112172>
33. Tabassum T, Hasan M, Begum L (2018) Transient melting of an impure paraffin wax in a double-pipe heat exchanger: Effect of forced convective flow of the heat transfer fluid. *Sol Energy* 159: 197–211. <https://doi.org/10.1016/j.solener.2017.10.082>
34. Liu L, Zhang X, Xu X, et al. (2020) The research progress on phase change hysteresis affecting the thermal characteristics of PCMs: A review. *J Mol Liq* 317: 113760. <https://doi.org/10.1016/j.molliq.2020.113760>
35. Rahman RA, Lahuri AH, Ismail I (2023) Thermal stress influence on the long-term performance of fast-charging paraffin-based thermal storage. *TSEP* 37: 101546. <https://doi.org/10.1016/j.tsep.2022.101546>

Instructions for Authors

Essentials for Publishing in this Journal

- 1 Submitted articles should not have been previously published or be currently under consideration for publication elsewhere.
- 2 Conference papers may only be submitted if the paper has been completely re-written (taken to mean more than 50%) and the author has cleared any necessary permission with the copyright owner if it has been previously copyrighted.
- 3 All our articles are refereed through a double-blind process.
- 4 All authors must declare they have read and agreed to the content of the submitted article and must sign a declaration correspond to the originality of the article.

Submission Process

All articles for this journal must be submitted using our online submissions system. <http://enrichedpub.com/> . Please use the Submit Your Article link in the Author Service area.

Manuscript Guidelines

The instructions to authors about the article preparation for publication in the Manuscripts are submitted online, through the e-Ur (Electronic editing) system, developed by **Enriched Publications Pvt. Ltd.** The article should contain the abstract with keywords, introduction, body, conclusion, references and the summary in English language (without heading and subheading enumeration). The article length should not exceed 16 pages of A4 paper format.

Title

The title should be informative. It is in both Journal's and author's best interest to use terms suitable. For indexing and word search. If there are no such terms in the title, the author is strongly advised to add a subtitle. The title should be given in English as well. The titles precede the abstract and the summary in an appropriate language.

Letterhead Title

The letterhead title is given at a top of each page for easier identification of article copies in an Electronic form in particular. It contains the author's surname and first name initial, article title, journal title and collation (year, volume, and issue, first and last page). The journal and article titles can be given in a shortened form.

Author's Name

Full name(s) of author(s) should be used. It is advisable to give the middle initial. Names are given in their original form.

Contact Details

The postal address or the e-mail address of the author (usually of the first one if there are more Authors) is given in the footnote at the bottom of the first page.

Type of Articles

Classification of articles is a duty of the editorial staff and is of special importance. Referees and the members of the editorial staff, or section editors, can propose a category, but the editor-in-chief has the sole responsibility for their classification. Journal articles are classified as follows:

Scientific articles:

1. Original scientific paper (giving the previously unpublished results of the author's own research based on management methods).
2. Survey paper (giving an original, detailed and critical view of a research problem or an area to which the author has made a contribution visible through his self-citation);
3. Short or preliminary communication (original management paper of full format but of a smaller extent or of a preliminary character);
4. Scientific critique or forum (discussion on a particular scientific topic, based exclusively on management argumentation) and commentaries. Exceptionally, in particular areas, a scientific paper in the Journal can be in a form of a monograph or a critical edition of scientific data (historical, archival, lexicographic, bibliographic, data survey, etc.) which were unknown or hardly accessible for scientific research.

Professional articles:

1. Professional paper (contribution offering experience useful for improvement of professional practice but not necessarily based on scientific methods);
2. Informative contribution (editorial, commentary, etc.);
3. Review (of a book, software, case study, scientific event, etc.)

Language

The article should be in English. The grammar and style of the article should be of good quality. The systematized text should be without abbreviations (except standard ones). All measurements must be in SI units. The sequence of formulae is denoted in Arabic numerals in parentheses on the right-hand side.

Abstract and Summary

An abstract is a concise informative presentation of the article content for fast and accurate Evaluation of its relevance. It is both in the Editorial Office's and the author's best interest for an abstract to contain terms often used for indexing and article search. The abstract describes the purpose of the study and the methods, outlines the findings and state the conclusions. A 100- to 250-Word abstract should be placed between the title and the keywords with the body text to follow. Besides an abstract are advised to have a summary in English, at the end of the article, after the Reference list. The summary should be structured and long up to 1/10 of the article length (it is more extensive than the abstract).

Keywords

Keywords are terms or phrases showing adequately the article content for indexing and search purposes. They should be allocated heaving in mind widely accepted international sources (index, dictionary or thesaurus), such as the Web of Science keyword list for science in general. The higher their usage frequency is the better. Up to 10 keywords immediately follow the abstract and the summary, in respective languages.

Acknowledgements

The name and the number of the project or programmed within which the article was realized is given in a separate note at the bottom of the first page together with the name of the institution which financially supported the project or programmed.

Tables and Illustrations

All the captions should be in the original language as well as in English, together with the texts in illustrations if possible. Tables are typed in the same style as the text and are denoted by numerals at the top. Photographs and drawings, placed appropriately in the text, should be clear, precise and suitable for reproduction. Drawings should be created in Word or Corel.

Citation in the Text

Citation in the text must be uniform. When citing references in the text, use the reference number set in square brackets from the Reference list at the end of the article.

Footnotes

Footnotes are given at the bottom of the page with the text they refer to. They can contain less relevant details, additional explanations or used sources (e.g. scientific material, manuals). They cannot replace the cited literature.

The article should be accompanied with a cover letter with the information about the author(s): surname, middle initial, first name, and citizen personal number, rank, title, e-mail address, and affiliation address, home address including municipality, phone number in the office and at home (or a mobile phone number). The cover letter should state the type of the article and tell which illustrations are original and which are not.

Address of the Editorial Office:

Enriched Publications Pvt. Ltd.
S-9, IInd FLOOR, MLU POCKET,
MANISH ABHINAV PLAZA-II, ABOVE FEDERAL BANK,
PLOT NO-5, SECTOR -5, DWARKA, NEW DELHI, INDIA-110075,
PHONE: - + (91)-(11)-45525005

